The Remote Sensing and Measurement of Melting Processes on Greenland and Antarctica

by

Nicholas Steiner

A dissertation submitted to the Graduate Faculty in Earth and Environmental Science in partial fulfillment of the requirements for the degree of Doctor of Philosophy, The City University of New York

2012

This manuscript has been read and accepted for the
Graduate Faculty in Earth and Environmental Science in satisfaction of the
dissertation requirement for the degree of Doctor of Philosophy.

Marco Tedesco

Date _____ _____

Chair of the Examining Committee

Cindi Katz

Date _____ _____

Executive Officer

Chris Derksen _____

Alan Frei _____

Johnny Luo _____

Supervisory Committee

THE CITY UNIVERSITY OF NEW YORK

Abstract

THE REMOTE SENSING AND MEASUREMENT OF MELTING PROCESSES ON GREENLAND AND ANTARCTICA

By

Nicholas Steiner

Adviser: Professor Marco Tedesco

We report measurements of melt-related processes for Antarctic and Greenland made using novel remote sensing algorithms and in-situ measurement techniques. First, persistent melting is mapped over Antarctica at high resolution using a novel melt-detection algorithm, based on wavelet-theory and multiscale analysis for the duration of the QuikSCAT satellite record (1999 through 2009). This novel approach is compared with threshold based methods, where melting is detected at 3dB below the winter mean backscatter, indicating an agreement to within 7 percent accuracy in yearly melt index [days-km2] and within 10 percent accuracy based automated weather station (AWS) comparisons due to the omission of short-duration melting events. In further comparison with Special Sensor Microwave/Image (SSMI) melting records, a higher degree of agreement (9 percent relative difference) is obtained by employing the wavelet-based approach than threshold-based (11 percent relative difference) methods. Secondly, we assess the validity of remote sensing based multispectral bathymetry from the analysis of concurrent in-situ multi-spectral and depth measurements collected over a supraglacial lake during early July 2010 in West Greenland (Lake Olivia, 69º36'35"N, 49º29'40"W). In particular, we evaluate lake

bottom albedo and the water attenuation coefficient. Analysis of in-situ data (using a remotely controlled boat equipped with a GPS, sonar and a spectrometer) illustrates the exponential trend of the water-leaving reflectance with lake depth. The attenuation factors obtained are compared with those proposed in the literature. Finally, measured ablation rates at the bottom of the two lakes, collected during the summers of 2010 and 2011, are on the order of ~ 6 cm/day, versus a rate of ~ 2.5 – 3 cm/day in the case of bare ice of surrounding areas. These measurements are compared with a thermodynamic model forced with the outputs of a regional climate model. In general, the model is able to satisfactorily reproduce the measured quantities with RMSE of the order of 3 – 4 cm for the ablation and ~ 1.5 ºC in the case of water temperature. Results confirm that the ablation at the bottom of supraglacial lakes can account for close to ten percent of the total lake depth.

Preface

The following document contains the collection of work done during my PhD. Each work has a topic that is related to the overall theme of this study, the remote sensing and measurement of melting processes. Each work stands on its own as either a publishable article or dataset. Several topics are covered including:

1. The Detection of Melt over Antarctica using Active Microwave Sensors
2. Measurement of Melt water Lake Depth using Multi-Spectral Optical Measurements
3. Measurement of Ablation Rates Under Melt Ponds on Greenland

For topics 1-3, the corresponding chapter is presented in the form of a journal article, each having a separate Introduction, Methods, and Conclusion sections (or similar). To summarize the introductory material for the reader's convenience, an additional Thesis Introduction section is added to the start of this document containing a brief introduction to each topic on a general level and the connections between topics.

Acknowledgements

This work is dedicated to my Mother and Father

This author is extremely gratified to have profited from the motivation and guidance provided by Prof. Marco Tedesco. The opportunity to be involved in two Greenland expeditions was especially rewarding. The author also gratefully acknowledges the support of his dissertation committee, and especially edits made available by Dr. Chris Derksen (Environment Canada).

The author is also very grateful for the support and guidance provided by all of the members of the Department of Earth and Environmental Science at the City College of New York. In particular the author is grateful for the encouragement and editing of Prof. Karin Block and Prof. Jeffrey Steiner (senior) and colleagues Dr. Lev Sviridov, Dr. Angelo Lampousis, Patrick Alexander and Jim (Soup) Rios. In addition, James Balog is acknowledged as the owner and sole rights holder of all chapter title page photos.

The author would also like to acknowledge the support of Katie Cole without whom this work would not be possible.

Table of Contents

Table of Figures

Table of Tables

1. Thesis Introduction

Warming from increased atmospheric CO_2 concentration is predicted to cause substantial effects at high latitudes where the world's largest ice sheets are located (Anisimov et al., 2007; Hansen et al., 2010b). The effect of increased surface temperatures on the Greenland Ice Sheet (GrIS) and the Antarctic Ice Sheet (AIS) will shape future climate. Intensification of seasonal surface melting can have global-scale effects, including increases in the global sea level due to loss of mass from ice-sheets as well as a decrease in the ice sheet albedo leading to positive mechanisms. A sea level rise of several meters would affect millions of people concentrated in coastal communities (Nicholls, 2004; Nicholls & Cazenave, 2010). Remote sensing techniques have proved useful for observing melt-conditions at high temporal resolutions and at a global scale. This study introduces new methods and in-situ measurements to improve upon the monitoring of melt processes, and elucidates how melt processes are related to the rate of ice loss occurring on the GrIS and AIS.

1.1 Rationale

Global climate change has already resulted in measurable temperature increases at high latitudes. Recent reanalysis of weather station measurements (Hansen et al., 2010b) reveals that the GrIS has experienced a 0.6 ^{o} to 1^{o} C observed increase in surface temperature during summer months (JJA) in the last ~60 years. There is evidence that these changes have intensified the previous decade (2000s), during which the GrIS has experienced a positive 1^{o} C to 2.2^{o} C average temperature anomaly (Hansen et al., 2010b). Positive temperature trends recorded from weather station measurements are corroborated by remotely sensed infrared-band land surface

temperature measurements that estimate a more pronounced 0.73 +- 0.12^{o} C increase in temperature per decade over the same time-period (Comiso, 2010).

However, similar warming trends are not observed for a majority of the AIS. Overall, the Antarctic continent has experienced a slight but consistent cooling based on air-temperate measurement and reanalysis (Comiso, 2010; Hansen et al., 2010b). One notable exception is the Antarctic Peninsula (AP), the northernmost region of the AIS. where temperatures have increased up to ~2.7^{o} Csince the International Polar Year of 1957 (Comiso, 2010; Hansen et al., 2010a). By some estimates, this same warming trend extends over the entire Western Antarctic Ice Shelf (WAIS), increasing at 0.1^{o} C per decade over the past 50 years (Steig et al., 2009).

As temperature increases at high latitudes, the rate of surface melting is expected to increase, as these processes are intimately linked (Ohmura, 2001; Vaughan, 2006). The area of surface melt over the GrIS, is currently increasing at a rate of ~17x10^{4} km^{2}/yr based on satellite observations starting in the late 1970s (Fettweis, 2007; Mernild et al., 2011; Tedesco, 2007). However, for the AIS there appears to be no registered change in melting for either the AP or the AIS as a whole (Munneke et al., 2012; Tedesco & Monaghan, 2009).

These melting processes are important, as melting of ice-sheets due to rising temperatures, along with the thermal expansion of the oceans, is a major factor in predicting the magnitude of global sea level rise (SLR) (Overpeck et al., 2006). Currently, a majority of increases to SLR are driven by ice lost from glaciers and ice caps (Meier et al., 2007; Nicholls & Cazenave, 2010). In the near future, ice lost by the AIS and GrIS will account for over half of this predicted increase (Alley et al., 2005; Rignot et al., 2011). The potential magnitude of SLR from the ice-sheets is great, as melting of the AIS and GrIS ice sheets completely would produce an estimated 70

meters of SLR (Alley et al., 2005; Rignot et al., 2011). Predictions of the maximum level of sea level rise expected for the 21st century vary from approximately 32 to 210 cm (Jevrejeva et al., 2010; Rahmstorf, 2007, 2010; Solomon et al., 2007). These estimates come with a high degree of uncertainty, mostly due to the unknown response of the GrIS and AIS (Hughes, 1981; Joughin & Alley, 2011; Overpeck et al., 2006; Shepherd & Wingham, 2007) . Based on the historic correlation between CO_2 and global sea level (Alley et al., 2005), current levels of CO_2 correspond to a substantially higher mean sea level than what is currently observed. In addition, the historic sea level record is not fully consistent with ocean level model projections (Alley et al., 2005; Meehl et al., 2007; Rohling et al., 2009). This indicates that some processes, such as the dynamic response of warming ice-sheets, are not captured by model predictions. As evidence, the currently observed rates of ice-loss exceed those predicted by a many global climate model prediction (Luthcke et al., 2006). In recent estimation of mass balance, the GrIS and AIS are experiencing ice loss that is accelerating at a combined rate of ~36.6+-2 Gt/yr^2 (Rignot et al., 2011). It is therefore crucial to understand and monitor ice loss by the AIS and GrIS, as well as the processes contributing to this loss, in order to improve SLR projections.

1.2 Ice Loss Processes

A majority of the ice-loss for the GriS and AIS occurs through two processes: calving events at the ice-sheet boundaries and surface runoff; both of which are affected by surface melting (van den Broeke 2009). The rate of ice-loss through calving events is primarily driven by gravity, but can be altered by surface melting in several ways (Bell, 2008). Surface melting may cause, or aid in the cause, of collapse of large-scale ice sheets, the semi-permanent floating platforms of ice found attached at the ice-sheet terminus. For the AIS, the surrounding ice-shelves structurally buttress the adjacent ice sheet (Alley et al., 2005; Dupont & Alley, 2006; Hughes, 1981; Joughin

& Alley, 2011). This suggests that stability at ice-sheet boundaries is highly correlated to the rate of ice-stream flow and, therefore, thinning within large ice-sheet systems (Dupont & Alley, 2006). Current events on the Antarctic Peninsula may indicate that changes in ice-shelf stability are already occurring, For example, in 2002 the Larsen B ice-shelf experienced a catastrophic collapse. The conditions and exact circumstances responsible for ice-sheet of collapses are not fully understood, however, observations of conditions on the ice-shelf surface provide clues. In the summer preceding the collapse, the Antarctic Peninsula experienced a melting season of relatively high intensity (Scambos et al., 2003; M. van den Broeke, 2005). Surface melting and runoff fed extensive melt-water ponding, as well as the flooding of glacial crevasses in the ice-shelf surface (Scambos et al., 2003). It is thought that pressure exerted by standing water in these cracks inhibited the closure of the crevasse system upon movement, and deepened existing openings through hydrofracture (MacAyeal et al., 2003). These factors led to a structural weakening of the ice-shelf and may have acted as the main catalyst for the Larsen B collapse in 2002. During this event, an area of ice that had formerly covered of 3,250 km^2 and was stable for at least (M. Van Den Broeke et al., 2009) the previous 12,000 years, disintegrated in several months (Domack et al., 2005). Immediately following the collapse rates of connected glacial ice-stream flow were observed to increase by 8 times their previous velocity (Rignot et al., 2004; Scambos et al., 2003). This series of events reinforces the implied role of melt-water in the process of ice-shelf collapse and therefore discharge.

Surface melting and melt-water ponding are also important components of the GrIS ice-sheet dynamics. Here, melt-water ponds are seasonal structures common to the ablation zone. Similar to the AIS, melt-ponds can influence the rate of ice-flow and discharge through different processes. With the buildup of water pressure caused by the continual filling of topographic

depressions, melt ponds can hydraulically fracture the underlying ice sheet causing rapid draining events (Das et al., 2008; Tedesco et al., 2012; Zwally et al., 2002). It is estimated that pond draining delivers a substantial outflow from surface areas directly to the bedrock (Zwally et al., 2002). The basal influx of warmer water is observed to accelerate adjacent down-gradient ice-flow, likely through lubrication and increased basal melting (Das et al., 2008; Joughin et al., 2008). In this way the melt pond cycle may substantially affect the rate of downstream ice-loss. Though relative importance of this process is not well understood, it has been recently proposed that temporary increases in ice flow may not have a large impact on seasonal mass balance (Schoof, 2010; A. V. Sundal et al., 2011; Van Der Veen et al., 2011). Regardless of its importance to the integrated seasonal discharge, the direct effect of surface melting on the rate of ice flow make it an integral part of ice-sheet dynamics.

In addition to the role that surface melting plays in ice discharge, surface melting is directly accounted for in surface mass balance estimates through seasonal runoff. For the GrIS and AIS, the volume of ice lost from meltwater runoff is comparable to the volume of ice lost from glacial discharge (M. Van Den Broeke et al., 2009). And like accelerating rates of ice-loss, direct runoff from melting has been increasing (Hanna et al., 2005; Luthcke et al., 2006). Presented in Chapter 3, are in-situ measurements of melt lake bottom-ablation rates that can be applied to future studies for validation and improved prediction of total ice loss due to ablation and runoff; this topic is discussed in greater detail therein.

Surface melting processes, for example the presence of melt ponds on the ice-sheet surface, will alter surface radiative fluxes, and lead to a higher absorption of short-wave solar insolation. This, in turn, promotes additional melting and is in itself a component of a positive feedback mechanism (Tedesco et al., 2011a). This phenomenon is observable on a seasonal basis as

changes in snow properties due to melting during one season are directly correlated with the surface melting in the following (J. Box et al., 2012; Tedesco et al., 2011b; M. R. van den Broeke et al., 2011). Additionally, the presence of a supraglacial lake, mainly due to the increased rate of absorption by the water column, has been shown to significantly (up to 2 times) increase the rate of ablation of the underlying ice (Tedesco et al., 2012).

It is clear that the rate of surface melting over the GrIS and AIS is important, and should be monitored. Unfortunately, melting processes are, in a practical sense, difficult to measure directly. In situ measurements of liquid water content are rare, and not currently made by automated weather stations. As a result, a majority of the spatially continuous estimates of melting and melt-water production are based on remotely sensed observations. As introduced in the following chapters, space-borne microwave frequency instruments are most commonly used for this purpose.(e.g Abdalati & Steffen, 1997; Ashcraft & Long, 2006; Liu et al., 2005; Mote et al., 1993; S. Nghiem et al., 2007; S. V. Nghiem et al., 2001; Steffen et al., 2004; Tedesco et al., 2007; Torinesi et al., 2003; Wang et al., 2008) . These instruments are able to detect the presence of water due to the high contrast in microwave frequency observations between dry and wet snow. This contrast exists because of the large difference in the complex dielectric constant of liquid water compared to ice at microwave frequencies, and particularly the imaginary part that accounts signal attenuation (Stiles & Ulaby, 1980; Tsang et al., 1985; F.T. Ulaby et al., 1981). Consequently, the active and passive microwave response to a liquid/solid phase change for any snow-covered area is much greater than other snow property changes (e.g. density or grain size) and will dominate the seasonal record (Stiles & Ulaby, 1980; F. T. Ulaby & Stiles, 1980).

The timings of both the seasonal melt onset and refreeze as measured by microwave frequency sensors are correlated to the duration of above-zero seasonal temperatures for each measurement

location (Tedesco et al., 2007; Wang et al., 2008; Zwally & Fiegles, 1994). Dry and wet states are generally separated by a thresholded brightness temperature (PMW) or backscatter (AMW) based on an estimate of the expected absolute change in the measured signal upon an increase of liquid water content (LWC) (Stiles & Ulaby, 1980). A fixed (spatially and temporally) time-series threshold has proven effective in many cases (Ashcraft & Long, 2006; S. V. Nghiem et al., 2001; Tedesco, 2009); however, the actual signal change at melt/refreeze events is dependent on many factors that are not static, such as the properties of the melting snow or ice. From changing snow conditions (snow metamorphosis) during the evolution of a snow-pack, the microwave response to liquid water content (LWC) vary with time as well as location. The optimal melt detection methodology is then temporally and spatially dynamic.

Another limitation of the fixed threshold methodology is that weather patterns or wind-driven melting are difficult to distinguish from melting events caused by synoptic-scale temperature increases. These events will produce similar values in microwave frequency observations, especially at higher frequencies (e.g. Ku-band), and will often be indistinguishable from wet snow (Fettweis et al., 2010). These weather related processes, however, will be short-lived in comparison to the length of seasonal melting. To remove sporadic weather related events from seasonal melting estimates it is necessary to consider the temporal duration of changes observed in microwave measurements. This can be accomplished using an arbitrarily small value (e.g. 3 days) as a minimum temporal threshold to remove weather-like melting (S. V. Nghiem et al., 2001; Tedesco et al., 2007).

As an alternative to fixed threshold approaches, dynamic methods, or ones that use relative signal change rather than absolute magnitude, have been developed for melt detection (Joshi et al., 2001; Liu et al., 2005). These approaches detect melting events from the timings of large

magnitude (relative to observed dry snow) signal changes within a seasonal time-series. We build upon these previous change-based methods by introducing a novel melt-detection algorithm based on wavelet theory. This approach evaluates all signal changes within a seasonal time-series of observations based on both temporal persistence and relative magnitude change. This acts to reduce the effects of weather and wind-driven events on seasonal melting estimates. This topic is introduced at greater length in Chapter 2.

As indicated, microwave sensors are well suited for the detection of melt-water extent at the surface (and volume) of snow and ice, but most are unable to distinguish melt surface-features such as ponds, from the surrounding melted surface. This is in some part due to the inherent resolution constraints of satellite based microwave instruments, but also due to saturation in the microwave response at a low LWC (Stiles & Ulaby, 1980). With increasing LWC, there is an exponentially increasing absorptivity (emissivity) which creates saturation in observations by both passive and active sensors. This inhibits the ability to resolve certain melt features, for example water saturated snow from standing water.

Optical sensors are able to both detect the presence of melt-water ponding as well as to estimate depth (or volume) from multi-spectral observations. Since the optical properties of pure water are very well known (Pope & Fry, 1997), and since melt-water has negligible sediment load and organic content (Tedesco & Steiner, 2011), with some knowledge of the diffuse pond-bottom albedo total depth can be estimated from satellite reflectivity measurements. In the blue and green visible channels the penetration depth into pure water is on the order of tens of meters (Pope & Fry, 1997) and loss along the water column for melt-ponds are within the dynamic range of some visible sensors (Tedesco & Steiner, 2011). Using multispectral sensors, the detected loss through the water column can be used to estimate the depth of melt-water ponds (J.

E. Box & Ski, 2007; Sneed & Hamilton, 2007; A. Sundal et al., 2009). To do this the bottom albedo must be well known (Philpot, 1989). In previous physically-based approaches, the bottom albedo value has been estimated from either observations of the surrounding snow and ice (Sneed & Hamilton, 2007). Melt-pond depth has also been measured using an empirical relationship from in-situ measurements (J. E. Box & Ski, 2007). We present in Chapter 3 in-situ observations of depth along concurrent measurements of water-leaving hyper-spectral reflectance. These are used to estimate a bottom albedo based on a physical-based parameterization and evaluate remote sensing techniques for multispectral bathymetry (Chapter 3).

In summary, this work presents a method for approximating melting using active microwave-frequency measurements (Chapter 2) that builds on earlier retrieval work on dynamic melt-detection algorithms. This approach is able to isolate temporally sustained melting events from those that are sporadic in time. This work also introduces in-situ measurements from fieldwork in Greenland on the theme of melt-ponding. As previously indicated, ponding is considered a key factor for ice-sheet dynamics for the AIS and GrIS. Two separate field expeditions during 2009 and 2010 provide the in-situ observations necessary for improvements the remote sensing of supraglacial melt pond depth as well as their effect on ice sheet ablation. Specifically, we provide the basis for improved estimates of standing water volume from remotely sensed optical measurements (Chapter 3). Lastly, we presents in-situ measurements of melt-pond ablation through novel techniques which can be applied to future studies for validation and improved prediction of total ice loss due to climate change induced melting of the GrIS and AIS (Chapter 4).

1.3 References

Abdalati, W., & Steffen, K. (1997). Snowmelt on the Greenland ice sheet as derived from passive microwave satellite data. *Journal of Climate, 10*(2), 165-175.

Alley, R. B., Clark, P. U., Huybrechts, P., & Joughin, I. (2005). Ice-sheet and sea-level changes. *Science, 310*(5747), 456-460. doi: 10.1126/science.1114613

Anisimov, O. A., Vaughan, T. V., Callaghan, C., Furgal, H., Marchant, T. D., Prowse, H., . . . Walsh, J. E. (2007). Polar regions (Arctic and Antarctic). Climate Change 2007: Impacts, Adaptation and Vulnerability. Contribution of Working Group II to the Fourth Assessment Report of the Intergovernmental Panel on Climate Change. In M. L. Parry, O. F. Canziani, J. P. Palutikof, P. J. van der Linden & C. E. Hanson (Eds.), (pp. 653-685). Cambridge, UK: Cambridge University Press.

Ashcraft, I. S., & Long, D. G. (2006). Comparison of methods for melt detection over Greenland using active and passive microwave measurements. *International Journal of Remote Sensing, 27*(12), 2469-2488.

Bell, R. E. (2008). The role of subglacial water in ice-sheet mass balance. *Nature Geoscience, 1*(5), 297-304. doi: 10.1038/ngeo186

Box, J., Fettweis, X., Stroeve, J., Tedesco, M., Hall, D., & Steffen, K. (2012). Greenland ice sheet albedo feedback: thermodynamics and atmospheric drivers. *The Cryosphere Discuss, 6*, 593-634.

Box, J. E., & Ski, K. (2007). Remote sounding of Greenland supraglacial melt lakes: implications for subglacial hydraulics. *Journal of Glaciology, 53*(181), 257-265.

Comiso, J. C. (2010). *Polar oceans from space*. New York: Springer.

Das, S. B., Joughin, I., Behn, M. D., Howat, I. M., King, M. A., Lizarralde, D., & Bhatia, M. P. (2008). Fracture propagation to the base of the Greenland Ice Sheet during supraglacial lake drainage. *Science, 320*(5877), 778-781. doi: 10.1126/science.1153360

Domack, E., Duran, D., Leventer, A., Ishman, S., Doane, S., McCallum, S., . . . Prentice, M. (2005). Stability of the Larsen B ice shelf on the Antarctic Peninsula during the Holocene epoch. *Nature, 436*(7051), 681-685.

Dupont, T. K., & Alley, R. B. (2006). Role of small ice shelves in sea-level rise. *Geophysical Research Letters, 33*(9). doi: L09503 10.1029/2005gl025665

Fettweis, X. (2007). Reconstruction of the 1979-2006 Greenland ice sheet surface mass balance using the regional climate model MAR. *Cryosphere, 1*(1), 21-40.

Fettweis, X., Tedesco, M., van den Broeke, M., & Ettema, J. (2010). Melting trends over the Greenland ice sheet (1958–2009) from spaceborne microwave data and regional climate models. *Cryosphere Discuss, 4*, 2433-2473.

Hanna, E., Huybrechts, P., Janssens, I., Cappelen, J., Steffen, K., & Stephens, A. (2005). Runoff and mass balance of the Greenland ice sheet: 1958-2003. *Journal of Geophysical Research, 110, D13108*.

Hansen, J., Ruedy, R., Sato, M., & Lo, K. (2010a). GLOBAL SURFACE TEMPERATURE CHANGE. [Review]. *Reviews of Geophysics, 48*, 29. doi: Rg4004 10.1029/2010rg000345

Hansen, J., Ruedy, R., Sato, M., & Lo, K. (2010b). GLOBAL SURFACE TEMPERATURE CHANGE. *Reviews of Geophysics, 48*. doi: Rg4004 10.1029/2010rg000345

Hughes, T. J. (1981). THE WEAK UNDERBELLY OF THE WEST ANTARCTIC ICE-SHEET. *Journal of Glaciology, 27*(97), 518-525.

Jevrejeva, S., Moore, J. C., & Grinsted, A. (2010). How will sea level respond to changes in natural and anthropogenic forcings by 2100? *Geophysical Research Letters, 37*. doi: L07703 10.1029/2010gl042947

Joshi, M., Merry, C. J., Jezek, K. C., & Bolzan, J. F. (2001). An edge detection technique to estimate melt duration, season and melt extent on the Greenland ice sheet using passive microwave data. *Geophysical Research Letters, 28*(18), 3497-3500.

Joughin, I., & Alley, R. B. (2011). Stability of the West Antarctic ice sheet in a warming world. *Nature Geoscience, 4*(8), 506-513. doi: 10.1038/ngeo1194

Joughin, I., Das, S. B., King, M. A., Smith, B. E., Howat, I. M., & Moon, T. (2008). Seasonal speedup along the western flank of the Greenland Ice Sheet. *Science, 320*(5877), 781-783. doi: 10.1126/science.1153288

Liu, H., Wang, L., & Jezek, K. C. (2005). Wavelet-transform based edge detection approach to derivation of snowmelt onset, end and duration from satellite passive microwave measurements. *International Journal of Remote Sensing, 26*(21), 4639-4660.

Luthcke, S. B., Zwally, H., Abdalati, W., Rowlands, D., Ray, R., Nerem, R., . . . Chinn, D. (2006). Recent Greenland ice mass loss by drainage system from satellite gravity observations. *Science, 314*(5803), 1286.

MacAyeal, D. R., Scambos, T. A., Hulbe, C. L., & Fahnestock, M. A. (2003). Catastrophic ice-shelf break-up by an ice-shelf-fragment-capsize mechanism. *Journal of Glaciology, 49*(164), 22-36. doi: 10.3189/172756503781830863

Meehl, G. A., Covey, C., Delworth, T., Latif, M., McAvaney, B., Mitchell, J. F. B., . . . Taylor, K. E. (2007). The WCRP CMIP3 multimodel dataset. *Bull. Am. Meteorol. Soc, 88*, 1383-1394.

Meier, M. F., Dyurgerov, M. B., Rick, U. K., O'Neel, S., Pfeffer, W. T., Anderson, R. S., . . . Glazovsky, A. F. (2007). Glaciers dominate Eustatic sea-level rise in the 21st century. *Science, 317*(5841), 1064-1067. doi: 10.1126/science.1143906

Mernild, S. H., Mote, T. L., & Liston, G. E. (2011). Greenland ice sheet surface melt extent and trends: 1960-2010. *Journal of Glaciology, 57*(204), 621-628.

Mote, T. L., Anderson, M. R., Kuivinen, K. C., & Rowe, C. M. (1993). Passive microwave-derived spatial and temporal variations of summer melt on the Greenland ice sheet. *Annals of Glaciology, 17*, 233-233.

Munneke, P. K., Picard, G., van den Broeke, M. R., Lenaerts, J. T. M., & van Meijgaard, E. (2012). Insignificant change in Antarctic snowmelt volume since 1979. *Geophysical Research Letters, 39*. doi: L01501 10.1029/2011gl050207

Nghiem, S., Steffen, K., Neumann, G., & Huff, R. (2007). *Snow accumulation and snowmelt monitoring in Greenland and Antarctica*.

Nghiem, S. V., Steffen, K., Kwok, R., & Tsai, W. (2001). Detection of snowmelt regions on the Greenland ice sheet using diurnal backscatter change. *Journal of Glaciology, 47*(159), 539-547.

Nicholls, R. J. (2004). Coastal flooding and wetland loss in the 21st century: changes under the SRES climate and socio-economic scenarios. *Global Environmental Change-Human and Policy Dimensions, 14*(1), 69-86. doi: 10.1016/j.gloenvcha.2003.10.007

Nicholls, R. J., & Cazenave, A. (2010). Sea-level rise and its impact on coastal zones (June, pg 1517, 2007). *Science, 329*(5992), 628-628.

Ohmura, A. (2001). Physical basis for the temperature-based melt-index method. *Journal of Applied Meteorology, 40*(4), 753-761.

Overpeck, J. T., Otto-Bliesner, B. L., Miller, G. H., Muhs, D. R., Alley, R. B., & Kiehl, J. T. (2006). Paleoclimatic evidence for future ice-sheet instability and rapid sea-level rise. *Science, 311*(5768), 1747-1750. doi: 10.1126/science.1115159

Philpot, W. D. (1989). Bathymetric mapping with passive multispectral imagery. *Applied optics, 28*(8), 1569-1578.

Pope, R. M., & Fry, E. S. (1997). Absorption spectrum (380–700 nm) of pure water. II. Integrating cavity measurements. *Applied optics, 36*(33), 8710-8723.

Rahmstorf, S. (2007). A semi-empirical approach to projecting future sea-level rise. *Science, 315*(5810), 368-370. doi: 10.1126/science.1135456

Rahmstorf, S. (2010). A new view on sea level rise. *Nature Reports Climate Change*, 44-45.

Rignot, E., Casassa, G., Gogineni, P., Krabill, W., Rivera, A., & Thomas, R. (2004). Accelerated ice discharge from the Antarctic Peninsula following the collapse of Larsen B ice shelf. *Geophysical Research Letters, 31*(18). doi: L1840110.1029/2004gl020697

Rignot, E., Velicogna, I., van den Broeke, M. R., Monaghan, A., & Lenaerts, J. (2011). Acceleration of the contribution of the Greenland and Antarctic ice sheets to sea level rise. *Geophysical Research Letters, 38*. doi: L05503 10.1029/2011gl046583

Rohling, E. J., Grant, K., Bolshaw, M., Roberts, A. P., Siddall, M., Hemleben, C., & Kucera, M. (2009). Antarctic temperature and global sea level closely coupled over the past five glacial cycles. *Nature Geoscience, 2*(7), 500-504. doi: 10.1038/ngeo557

Scambos, T., Hulbe, C., & Fahnestock, M. (2003). Climate-induced ice shelf disintegration in the Antarctic Peninsula. *Antarctic Research Series, 79*, 79-92.

Schoof, C. (2010). Ice-sheet acceleration driven by melt supply variability. *Nature, 468*(7325), 803-806. doi: 10.1038/nature09618

Shepherd, A., & Wingham, D. (2007). Recent sea-level contributions of the Antarctic and Greenland ice sheets. *Science, 315*(5818), 1529-1532. doi: 10.1126/science.1136776

Sneed, W., & Hamilton, G. S. (2007). Evolution of melt pond volume on the surface of the Greenland Ice Sheet. *Geophysical Research Letters, 34*(3).

Solomon, S., D., Qin, M., Manning, Z., Chen, M., Marquis, K. B., Averyt, M., & Miller, H. L. (2007). *Contribution of Working Group I to the Fourth Assessment Report of the Intergovernmental Panel on Climate Change*. Cambridge, United Kingdom and New York, NY, USA: Cambridge University Press.

Steffen, K., Nghiem, S., Huff, R., & Neumann, G. (2004). The melt anomaly of 2002 on the Greenland Ice Sheet from active and passive microwave satellite observations. *Geophys. Res. Lett, 31*(20), L20402.

Steig, E. J., Schneider, D. P., Rutherford, S. D., Mann, M. E., Comiso, J. C., & Shindell, D. T. (2009). Warming of the Antarctic ice-sheet surface since the 1957 International Geophysical Year. *Nature, 457*(7228), 459-U454. doi: 10.1038/nature07669

Stiles, W. H., & Ulaby, F. T. (1980). The active and passive microwave response to snow parameters 1. Wetness. *Journal of Geophysical Research, 85*(C2), 1037-1044.

Sundal, A., Shepherd, A., Nienow, P., Hanna, E., Palmer, S., & Huybrechts, P. (2009). Evolution of supra-glacial lakes across the Greenland Ice Sheet. *Remote Sensing of Environment, 113*(10), 2164-2171.

Sundal, A. V., Shepherd, A., Nienow, P., Hanna, E., Palmer, S., & Huybrechts, P. (2011). Melt-induced speed-up of Greenland ice sheet offset by efficient subglacial drainage. *Nature, 469*(7331), 521-524.

Tedesco, M. (2007). Snowmelt detection over the Greenland ice sheet from SSM/I brightness temperature daily variations. *Geophysical Research Letters, 34*(2). doi: L02504 10.1029/2006gl028466

Tedesco, M. (2009). Assessment and development of snowmelt retrieval algorithms over Antarctica from K-band spaceborne brightness temperature (1979-2008). *Remote Sensing of Environment, 113*(5), 979-997.

Tedesco, M., Abdalati, W., & Zwally, H. J. (2007). Persistent surface snowmelt over Antarctica (1987-2006) from 19.35 GHz brightness temperatures. *Geophysical Research Letters, 34*(18). doi: L1850410.1029/2007gl031199

Tedesco, M., Fettweis, X., Van den Broeke, M., Van de Wal, R., Smeets, C., van de Berg, W. J., Box, J. (2011a). The role of albedo and accumulation in the 2010 melting record in Greenland. *Environmental Research Letters, 6*, 014005.

Tedesco, M., Fettweis, X., van den Broeke, M. R., van de Wal, R. S. W., Smeets, C. J. P. P., van de Berg, W. J., . . . Box, J. E. (2011b). The role of albedo and accumulation in the 2010

melting record in Greenland. *Environmental Research Letters, 6*(1). doi: 014005 10.1088/1748-9326/6/1/014005

Tedesco, M., Luthje, M., Steffen, K., Steiner, N., Fettweis, X., Willis, I., . . . Banwell, A. (2012). Measurement and modeling of ablation of the bottom of supraglacial lakes in western Greenland. *Geophysical Research Letters, 39*. doi: L02502 10.1029/2011gl049882

Tedesco, M., & Monaghan, A. J. (2009). An updated Antarctic melt record through 2009 and its linkages to high-latitude and tropical climate variability. *Geophysical Research Letters, 36*. doi: L18502

10.1029/2009gl039186

Tedesco, M., & Steiner, N. (2011). In-situ multispectral and bathymetric measurements over a supraglacial lake in western Greenland using a remotely controlled watercraft. *The Cryosphere, 5*, 445-452.

Torinesi, O., Fily, M., & Genthon, C. (2003). Variability and trends of the summer melt period of Antarctic ice margins since 1980 from microwave sensors. *Journal of climate, 16*(7), 1047-1060.

Tsang, L., Kong, J. A., & Shin, R. T. (1985). Theory of microwave remote sensing. *A WileyInterscience publication*, 214-235.

Ulaby, F. T., Moore, R. K., & Fung, A. K. (1981). Microwave remote sensing: Active and passive. Volume 1-Microwave remote sensing fundamentals and radiometry.

Ulaby, F. T., & Stiles, W. H. (1980). THE ACTIVE AND PASSIVE MICROWAVE RESPONSE TO SNOW PARAMETERS .2. WATER EQUIVALENT OF DRY SNOW.

Journal of Geophysical Research-Oceans and Atmospheres, 85(NC2), 1045-1049. doi: 10.1029/JC085iC02p01045

van den Broeke, M. (2005). Strong surface melting preceded collapse of Antarctic Peninsula ice shelf. *Geophysical Research Letters, 32*(12). doi: L12815 10.1029/2005gl023247

Van Den Broeke, M., Bamber, J., Ettema, J., Rignot, E., Schrama, E., Van de Berg, W. J., . . . Wouters, B. (2009). Partitioning recent Greenland mass loss. *Science, 326*(5955), 984-986.

van den Broeke, M. R., Smeets, C. J. P. P., & van de Wal, R. S. W. (2011). The seasonal cycle and interannual variability of surface energy balance and melt in the ablation zone of the west Greenland ice sheet. *Cryosphere, 5*(2), 377-390. doi: 10.5194/tc-5-377-2011

Van Der Veen, C., Plummer, J., & Stearns, L. (2011). Controls on the recent speed-up of Jakobshavn Isbrae, West Greenland. *Journal of Glaciology, 57*(204), 770-782.

Vaughan, D. G. (2006). Recent trends in melting conditions on the Antarctic Peninsula and their implications for ice-sheet mass balance and sea level. *Arctic Antarctic and Alpine Research, 38*(1), 147-152. doi: 10.1657/1523-0430(2006)038[0147:rtimco]2.0.co;2

Wang, L., Derksen, C., & Brown, R. (2008). Detection of pan-Arctic terrestrial snowmelt from QuikSCAT, 2000–2005. *Remote Sensing of Environment, 112*(10), 3794-3805.

Zwally, H. J., Abdalati, W., Herring, T., Larson, K., Saba, J., & Steffen, K. (2002). Surface melt-induced acceleration of Greenland ice-sheet flow. *Science, 297*(5579), 218-222. doi: 10.1126/science.1072708

Zwally, H. J., & Fiegles, S. (1994). EXTENT AND DURATION OF ANTARCTIC SURFACE MELTING. *Journal of Glaciology, 40*(136), 463-476.

A Wavelet Based Melt Detection Algorithm for Enhanced Resolution Scatterometer Data over Antarctica (2000-2008)

To be submitted to: The Cryosphere Discussions

2 A Wavelet Based Melt Detection Algorithm for Enhanced Resolution Scatterometer Data over Antarctica (2000-2008)

2.1 Abstract

Persistent melting is mapped over Antarctica at high resolutions using a novel melt-detection algorithm, based on wavelet-theory and multiscale analysis, for the duration of the QuikSCAT satellite record (1999 through 2009). This method is applied to Ku band (13.4 GHz) SeaWind Instrument normalized backscatter that is spatially enhanced to 2.225 km (Long & Hicks, 2000). This novel approach is compared with threshold based methods, where melting is detected at 3dB below the winter mean backscatter, indicating an agreement to within 7 percent accuracy in yearly melt index [days-km^2] and within 10 percent accuracy based automated weather station (AWS) comparisons. The differences between methods are found to be due to the expected omission of short-duration melting events. In further comparison with Special Sensor Microwave/Image (SSMI) melting records over the same duration, we find a higher degree of agreement (9 percent relative difference) using the wavelet-based approach the than threshold-based (11 percent relative difference) methods. When melting estimates for the Antarctic Peninsula are compared to the Southern Annular Mode (SAM), it is found that increases in melting over some regions AP are well correlated with a positive SAM mode.

2.2 Introduction

The current and future behavior of mass balance of the Antarctica Ice Sheet (AIS) is one of the largest uncertainties in the prediction of global sea-level rise over the coming decades

(Bromwich & Nicolas, 2010; Dowdeswell, 2006; Lemke et al., 2007) with many studies having focused on quantifying surface mass balance and surface temperature trends over Antarctica (Chen et al., 2009; Rignot & Thomas, 2002; Shepherd & Wingham, 2007). Recently, Rignot et al (2011) have used the Regional Atmospheric Climate Model (RACMO2) in conjunction with Antarctica ice sheet discharge data to reveal an accelerating mass loss of 15.1 ± 12 Gt/yr^2, in agreement with estimates obtained from the Gravity Recovery and Climate Experiment (GRACE) of 13.2 ± 10 Gt/yr^2. Results reported in the literature also indicate that Antarctica temperatures have been increasing over the last decades (Steig et al., 2009), with the Antarctic Peninsula being subject to warming above 0.5°C/decade in the second part of the past century (Turner et al., 2005). The Antarctic Peninsula has witnessed dramatic events over the past decade: in 2002, the Larsen B ice shelf collapsed and so did a large portion of the Wilkins ice shelf in 2008. Both collapses were the consequence of a suite of physical surface processes and ocean-ice shelves interaction mechanisms. Surface melting likely played a key role, with the formation of meltwater ponds on the surface of the ice shelves contributing to their disintegration through hydrofracturing *,(e.g., MacAyeal et al., 2003)*, with cracks propagating to the base of the ice and ultimately leading to the catastrophic collapse. This episode highlights the importance of improving our capabilities of mapping surface and subsurface melting over Antarctica which is crucial for surface mass balance estimates and for understanding ice sheet and ice shelf dynamics and processes.

Though surface melting can be estimated from surface meteorological measurements collected by automatic weather stations (AWS), such measurements are sparse over Antarctica and primarily located along the coast or at low elevations. The presence of melting snow in Antarctica can be estimated through the analysis of spaceborne microwave data, at large spatial

scales and high temporal resolution, as a consequence of the abrupt and considerable change in the recorded signal rapidly following the appearance of liquid water in snow (e.g., Ashcraft & Long, 2006; Tedesco et al., 2006; Tedesco & Monaghan, 2009; Ulaby & Stiles, 1980). Results from these observations have indicated that the sign of the melting trends over Antarctica has been regionally variable and dependent on the period analyzed and on the indices used, with the continent-averaged trend being small and generally statistically not significant for the period 1979 - 2009 (Liu et al., 2005; Picard et al., 2007; Tedesco & Monaghan, 2009; Torinesi et al., 2003).

Both active and passive (e.g., Kunz & Long, 2004; Liu et al., 2005; S. Nghiem et al., 2007; Tedesco et al., 2007; Torinesi et al., 2003) microwave instruments, such as scatterometers or microwave radiometers data have been used to estimate Antarctic melt records. Many of these studies use the so-called *threshold-based approaches*, meaning that melting is detected when the recorded active (passive) microwave signal is below (above) a threshold value (Ashcraft & Long, 2006; L. B. Wang et al., 2008; Zwally & Fiegles, 1994). In many approaches widely used in the literature, the threshold value for wet snow detection a selected value is added to a baseline value obtained from, for example, the wintertime (December through February) mean value. Approaches making use of a fixed value added to a 'dry' condition baseline-measurement will be denoted here as *fixed threshold approaches* (denoted FT thereafter). Approaches making use of dynamic temporal or spatial threshold values will be referred to as *dynamic threshold approaches* (Tedesco, 2009). Beside those based on thresholding, approaches using the intrinsic properties of the spaceborne signal have been proposed (Joshi et al., 2001; Liu et al., 2005; L. Wang & Yu, 2011). These approaches are inherently dynamic, in the sense that they are based on the magnitude of relative change within a backscattering or brightness temperature time-series

and will refer to them as *dynamic approaches*. The driving idea behind these approaches is that large amplitude signal changes (which are associated with the changes associated with the insurgence or disappearance of wet snow) are detected using differential operators, such as the derivative-of-Gaussian (DoG, e.g. *Yoshi et al, 2001*) or the dyadic wavelet edge detection method (*e.g., Liu 2005*).

In this study, we build on previous work based on wavelet theory for detecting and mapping wet snow from the time series of an enhanced spatial resolution microwave backscattering product. We apply a multi-scale analysis to the seasonal time series of each pixel over Antarctica, without the need of a-priori information, as in the case of previous approaches. Additionally, because of the properties of the wavelet methodology, the approach proposed in this study can distinguish between persistent melting (melting lasting continuously for a certain number of days, with the specific values discussed in the paper) and transient or sporadic melting events. Through our method, we can identify those melt onset "edges" (as well as smooth transitions) that are relevant on a seasonal scale, allowing us to identify snowmelt onset and refreeze events that are at least one order of magnitude larger than winter mean at scales comparable to the length of the melting season and persistent based on comparison with idealized signal "edges."

We apply our method to an enhanced spatial resolution QuikSCAT (Ku band) scatterometer dataset distributed by the Microwave Earth Remote Sensing (MERS) Laboratory (http://www.mers.byu.edu/) with an effective resolution of 5 km, re-gridded at 2.225 km (Early & Long, 2001; Spencer et al., 2003). The enhanced spatial resolution of such product allows to discriminate melting patterns at sub-ice-shelf resolution as well as to resolve melting patterns and trends that might not be apparent in coarse spatial resolution products. This type of high resolution dataset is ideal, for example, for the Antarctic Peninsula, a region of relatively high

elevation contrast where the coarse resolution of passive microwave observations (e.g., 25 km) might underestimate melt due to a large sub-pixel elevation gradient.

This study is focused on estimates of the seasonal melt onset date (MO), melt off date (MF), melt extent (ME) and melt duration (MD) over the whole Antarctica. Results obtained with the method proposed in this study are compared with those obtained from a fixed threshold method applied to the same active microwave data set and from two different fixed threshold approaches applied to spaceborne microwave brightness temperatures. The fixed threshold approach used for comparison is introduced by Ashcraft and Long (2006). In this methodology, a -3 dB fixed offset is added to the winter-mean normalized backscatter to obtain a threshold value below which snow is assumed to have a layer (3.8 cm) with liquid water content (LWC) of greater than 1 percent. Following Ngheim (2007) limit the minimum length of consecutive melting days are limited to 3 in order to remove non-winter melt and spurious backscattering transitions. Results from the approach proposed in this study are also compared with estimates of melt obtained from the analysis of surface (air) temperature values recorded by automated weather stations (AWS). Finally, building on previous studies, the relationship between the melting estimates obtained with the novel method here reported are discussed and quantities describing climate drivers in Antarctica, such the Southern Annular Mode (SAM) indices.

2.3 Methodology

In this section we introduce the wavelet method and its application to melt detection. A more detailed description of wavelet theory can be found in Mallet (1999) or Holschneider (1995). Wavelets have found great utility in image compression (Taubman et al., 2002), real-time medical applications like the analysis of electro-cardiograms (Addison, 2005; Li et al., 1995), as well as the analysis of remote sensing data time-series (Liu et al., 2005). A wavelet transform,

like a Fourier transform, is able to represent a time-series as an equivalent sum of its frequency components. Wavelet analysis is ideal for non-periodic data-series like those commonly found in remote sensing applications because the frequency components are localized. To clarify some terminology, the term frequency is often reserved for discussions of Fourier analysis, while when discussing wavelet analysis, frequencies are referred to as scales (denoted as '*s'*). Scales are simply the inverse of frequency and are equivalent to the data time-step at their smallest values.

Wavelet or wavelet-like methodologies have been previously applied to microwave data for the purpose of snow-melt detection (see Joshi, et al, 2001 and Liu, et al. 2005 for details). In Joshi et al (2001) melting is detected by identifying maximum values, above a set threshold, in a series of relative signal-change coefficients determined using a derivative of Gaussian function (DoG) function using a series of brightness temperatures. The threshold is set through trial-and-error, and is used to separate melting-like transitions from non-melting. The melting season is defined as the period of time between melting-like signal transitions in brightness temperatures. In another similar study, (Liu et al, 2005) use a wavelet-based methodology similar to Joshi et al. (2001). Time-series of brightness temperatures are separated into their dyadic scale components using a first derivative spline function, as described in Mallet and Zhong (1992). It was determined that the majority of high frequency signal noise and non-melting transitions are relegated to the shortest dyadic scales (high frequency). Melting is then identified by thresholding one dyadic scale ($s=2^3$) to identify both melting and refreeze transitions. The location of this transition is then traced across dyadic scales to its position at the finest scale. Optimal threshold values are determined through statistical analysis of a large population of wavelet coefficient magnitudes, corresponding to the relative magnitude of transition, or 'edge-

strength.' The melting season, like in Joshi et al (2001) is defined as the periods between melt-like transitions.

Our current methodology builds upon these previous results in that it uses differential operators to analyze a data time-series to determine the relative magnitude of each signal transition. The most significant difference between the method proposed here and those reported in the literature is that signal changes can be evaluated based on all scale components, as opposed to a single scale component as in Liu (2005) and Joshi (2001). This is done using a continuous wavelet transform (CWT) that allows for the accurate connection of all scale components for a given signal transition. Another novel aspect of this current melt-detection methodology is the use of multi-scale analysis, which has found similar applications in image processing (S. G. Mallat, 1999) and seismic wave response (Herrmann, 2001; Le Gonidec et al., 2003). Multiscale analysis allows for the classification of signal transition types (i.e. step-like or smooth) in order to exclude non-melt or sporadic melt transitions (i.e. cusp-like or spike-like). This methodology is novel, and to our knowledge, it is the first time that such approach is applied to remote sensing of snow and ice.

2.3.1 Continuous Wavelet Transform and Multi-scale Analysis

In the method proposed in this study, melting is identified from +the analysis of the backscattering time series through the multi-scale components derived from a wavelet transform. The magnitude of a given scale component (s_0) at any one location (u_0) along the backscattering time series (f) is determined from the convolution of f with a short, wave-like, analyzing function (ψ) centered at that position. Here, ψ is confined, by its compact support, to a segment along the signal that is proportional to the scale being considered, s_0. Convolution is then repeated for each position, as the wavelet function is translated over the entire signal length. This produces a series

of wavelet coefficients (*Wf*) for each scale (**Figure 2-1**a). The magnitude of $Wf(u_0,s_0)$ is proportional to the relative contribution of s_0 to the signal at u_0. To analyze multiple scales, the wavelet function is dilated (in proportion to *s*) using a scaling factor, here equal to $\frac{1}{\sqrt{s}}$ (S. G. Mallat, 1999). A continuous wavelet transform (*CWT*) is a collection of position-scale representations ordered by scale, where the difference in sequential wavelet dilation is small. The CWT defines as a scale-position space, orthogonal to the time axis (**Figure 2-1**b).

The CWT is calculated using the following integrated convolution product (S. G. Mallat, 1999)

Equation 1

$$Wf(u,s) = \int_{-\infty}^{+\infty} f(t)\frac{1}{\sqrt{s}}\psi^*\left(\frac{t-u}{s}\right)dt$$

Here *f* refers to the yearly backscattering time series at each pixel location over Antarctica. Daily measurements are arranged from June 1st through May 31st of the next year so that the austral summer (DJF) is continuous. Generally, the wavelet function (ψ), used in the signal convolution, is defined as any non-zero function with a zero average, $\int_{-\infty}^{+\infty}\psi(t)dt = 0$ and compact support, indicating that the function will equal zero at negative and positive infinity. It is often constructed from a mother wavelet (θ), a prototype function with compact support and often continuously differentiable. In this study we use a Gaussian function for θ. The analyzing wavelet function (ψ) is then set to a derivative of the Gaussian function, $\psi(t) = (-1)^n\frac{d^n\theta(t)}{dt^n}$, with the function order, *n,* equal to 1 (Mallet, 1999). The choice of *n* will be discussed further.

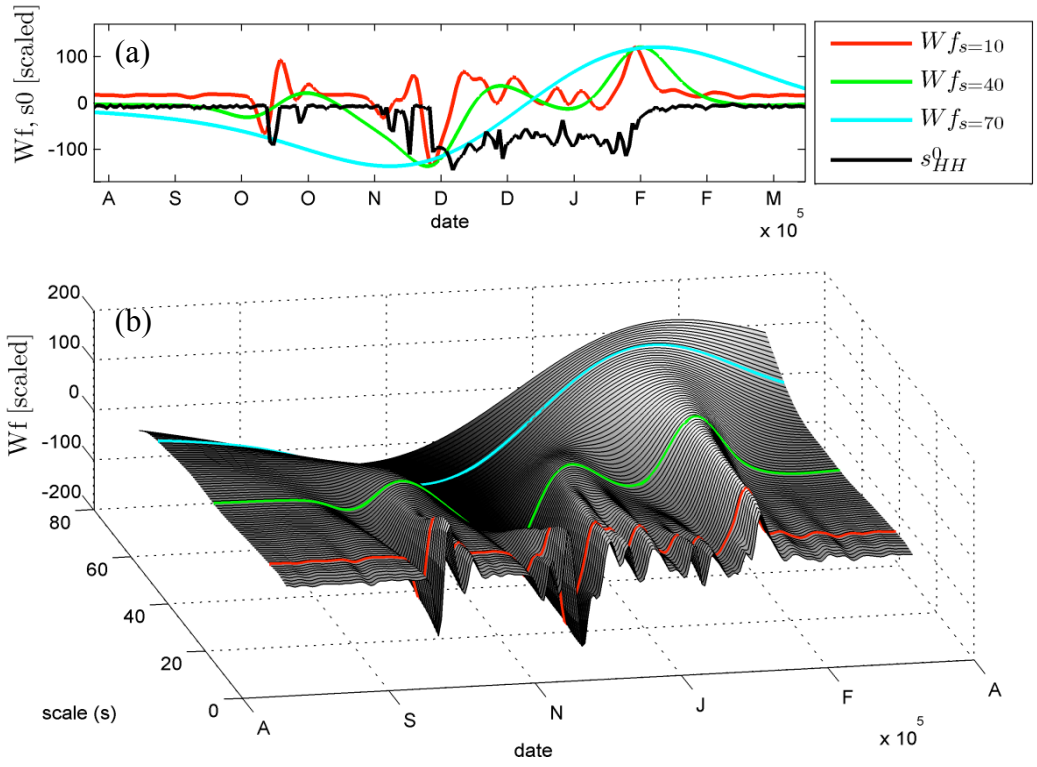

Figure 2-1 (a) The time-scale components of a backscattering time-series (black), are plotted as colored lines. It is important to note that the actual values (i.e. dB or Wf) of these components are normalized (in the Y-direction) so that they can be plotted on the same axis. (b) A continuous wavelet transform of the backscattering time series shown in (a) with individual scales highlighted as in (a).

When expressed as an equivalent convolution product Eq. 1 becomes (Mallet, 1999):

Equation 2

$$Wf(u,s) = s^n \left(f \star \frac{d^n}{dt^n} \overline{\theta}_s \right)(u) = s^n \frac{d^n}{du^n} (f \star \overline{\theta}_s)(u)$$

Equation 2, describes wavelet transform in two functional parts: one that will smooth the function ($f \star \bar{\theta}_s$), and another that will extract details $\left(s^n \frac{d^n}{du^n}\right)$ (Hermann, 2001). By using a derivative-of-Gaussian wavelet, and n = 1, large magnitude $|Wf|$ are expected at positions corresponding to substantial signal edges, similar to the first derivative of that function.

Signal discontinuities, like the abrupt changes in backscatter associated with melting and refreezing events, produce areas of elevated $|Wf|$ in the CWT that converge at fine scales to the exact position of signal discontinuity (S. Mallat & Zhong, 1992). Hence, in the CWT of AMW time-series during seasonal melt both upon melt onset and refreeze we expect large magnitude $|Wf|$ that extend across scales. As an example, a backscattering time series over the Larsen Ice Shelf during the 2006-2007 melting season is presented in **Figure 2-2**a with the corresponding CWT plotted in **Figure 2-2**b. Representative of a typical melting season for the Larsen C Ice Shelf, short-duration backscatter losses are recorded during July, October and November, most likely due precipitation events and wind-driven melting, followed by a more sustained melting period from December to mid-February. The sustained melting event is isolated from shorter duration backscatter changes using multiscale analysis of a CWT as described in the following.

Abrupt and sustained changes in the radar signal will produce observable features in the CWT. At position u=185 (of the CWT, corresponding to a ~20 dB decrease over several days, a conical shape of negative (white) $|Wf|$ is coincident with the signal transition at the finest scale

and extends down over scales. Values within this conical area compose the multi-scale components of that transition (u=185). An opposite condition is observed, corresponding to a refreeze event occurring close to position u=260. A similar conical shape is observed, composed of positive (black) $|Wf|$, indicating a rapid increase in observed backscatter (also ~20 dB) (**Figure 2-2**b).

Maximum |Wf| values follow "ridges" of these cone-shaped regions. Maximum or minimum values are referred to as wavelet transform modulus maxima (WTMM). All WTMM in a CWT are found by determining positions where $\frac{\partial W f(u_0, s_0)}{\partial u} = 0$ and where each maxima point is greater in absolute magnitude compared to its immediate left and right neighbors (Mallet, 1999). We can connect all WTMM by following them across scales to form Wavelet Modulus Maximum Lines (WTMML, Mallet 1999). The terminating position of the WTMML on the time axis is a position where the signal, or its derivative, is not well defined (i.e. discontinuous). By connecting all WTMM into WTMML we can identify all singularities (and therefore all potential melting events) in the data series (S. Mallat & Zhong, 1992). Using a Gaussian derived wavelet function ensures that all WTMM will propagate from a large scale, without interruption, to the finest scale (Mallet, 1999). We plot all WTMM connected as lines superimposed on the CWT in **Figure 2-2**b. (black, red and green lines, **Figure 2-2**b).

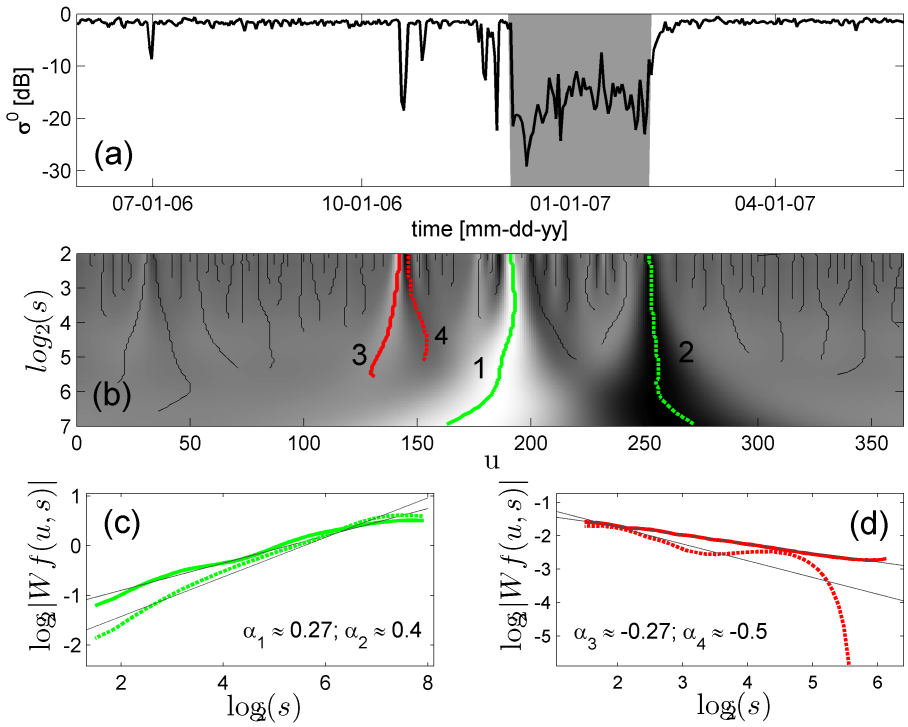

Figure 2-2 (a) QuikSCAT, HH pol., backscattering time-series plotted with the melt duration (MD) estimated using the CWT method (grey shaded in gray). (b) The continuous wavelet transform of this particular time series. Dark gray to black color values indicate positive |Wf| and light-gray to white negative. The locations of WTMML are indicated as black, green or red lines. Lines associated with melt onset (MO, WTMML1) melt refreeze (MF, WTMML 2) and sporadic, early season melt (WTMML 3, WTMML 4) are highlighted similar to Figure 2b. (c), associated $\boldsymbol{\alpha}$ (Holder Exponent) value is indicated. (d) The $\log_2$-$\log_2$ plot of WTMML scale and magnitude for a sporadic melting event and associated $\boldsymbol{\alpha}$ values.

2.3.2 **Multi-Scale Analysis**

Each WTMML found for a backscattering time-series of data is analyzed to determine whether or not it is related to a melting event. In this study we focus on measuring only continuous seasonal melting, e.g. those melting events that are not sporadic in time. This distinction is made using multi-scale analysis to characterize the transition type based on its WTMML.

Multi-scale analysis is able to estimate the signal regularity (i.e. the number of times differentiable) at point of each signal transition (S. G. Mallat, 1999). Function regularity is proportional to the rate of decay in WTMM magnitude along the WTMML, expressed by a Holder exponent,α , (Herrmann, 2001). The value of α, for an isolated and ideal transition, can be determined from the WTMML using the following equation (Mallet, 1999):

Equation 3

$$|Wf(s,u)| \leq As^{\alpha}$$

We estimate the Holder exponent by finding the linear least squares regression between the $\log_2$-$\log_2$ plot of $|Wf|$ versus scales for each value along the WTMML. An example of this is found in **Figure 2-2**c and 2d, where the WTMMLs are derived from corresponding CWT (**Figure 2-2**b). The α values reported for each WTMML approximates the signal regularity, or the number of times differentiable, at the terminating position of that WTMML. Since transitions in backscatter are not likely isolated (there is some overlap between the conical regions in the CWT), we only use the Holder exponent as an estimate of the signal regularity.

Once α values are determined, they are classified based on several idealized transition types whose α values are known. In Gondic et al (2003) a step-like transition is determined to have α

values of zero for all scales. Additionally, a ramp-like transition or smoothed transition is determined to have a α value of 1 or greater (Mallet 1999, Gondic et al 2003). We consider melt onset transition, similar to location 185 (labeled 1) in **Figure 2-2**b to be an approximate step-like transition. The actual α value determined by linear least squares (α_1 =0.27) is larger than in the simplified case, since it is not an ideal transition and it is not isolated. Nearby signal heterogeneity contributes to the WTMML values (i.e. there are other transitions within the compact support of the wavelet function at multiple scales). We consider melt refreeze events, like **Figure 2-2**b, position 250, similar to a ramp, or smoothed transition. The determined regularity ($\alpha_2 = 0.4$, **Figure 2-2**c) is greater than that of a step-function as expected, since this transition also has a steep step-like component and is not isolated.

For spike-like transitions, similar to the rapid backscattering change at position, u = 240, (**Figure 2-2**b), α values will be negative (Gondic et al 2003, Mallet 1999). This transition produces two WTMML (**Figure 2-2**d), labeled 3 and 4, both having negative α values($\alpha_3 = -0.27, \alpha_4 = -0.4$). Negative α values associated with that WTMML indicate that the signal is that is discontinuous and non-differentiable at that point. By removing all negative α WTMML, we can remove all backscattering transitions that appear discontinuous at the scale of reference. In terms of melt detection, this will remove from consideration sporadic backscattering changes that return to "dry" conditions rapidly relative to the reference scale. This will create a melt detection process that will only find continuous melting seasons.

For locations that do not experience melting events, variation in the radar signal will vary with of snow property changes due to snow metamorphism or precipitation events. Sustained changes such as these will produce WTMML of low magnitude relative to those observed with changes in LWC. To reduce the influence of these events, we set a minimum threshold for |WTMML|

magnitude at all temporal scales corresponding to an order of magnitude greater than those observed during winter (JJA) for each location. This is a conservative threshold and is not observed to influence those areas experiencing melt. Future studies should address a physical basis for this threshold.

The choice in wavelet function order (n) is important in estimating signal regularity. Simply put, n determines the number of zero crossings for a wavelet function. A wavelet function with n vanishing moments can estimate the signal regularity up until positive or negative n. Therefore, by using the first derivative of a wavelet function, we can estimate α to within ± 1. It is also the case that the number of WTMMLs in any CWT are proportional the wavelet function order (Mallet, 1999). To reduce the computational demands of our melt-detection algorithm, we set n to the lowest possible number (n=1), hence reducing the number of WTMML that must be considered for each backscattering time series. We acknowledge that under certain conditions a higher order wavelet function may be more appropriate. For example, a second order function will have WTMML associated with points of inflection, where the signal regularity is greater than 1. For gradual changes in backscatter during the start (or end) of melt conditions, the initial change in backscatter from melting will be a point of inflection as the signal diverges from the winter mean value. In comparison to rapid onset melting where the maximum slope of signal change is concurrent with the divergence from winter mean backscatter. This is observed to some extent for at position 250 (**Figure 2-2**b). The wavelet determined melting season (shaded area) MF date corresponding to the point of maximum transition in backscatter. This estimation is several days prior to the location where the backscattering returns to "dry" scattering magnitudes, and a more appropriate location for MF may be at ~260. This issue does not imply that all melting events associated with a smooth transition will be missed by our melt detection

algorithm, but rather the estimation of melt onset and melt refreeze dates in such cases may be determined with more accuracy using a higher order wavelet function.

2.3.3 Melt Detection Process

In the manner described in Sections 3.2 and 3.3, a collection of all wavelet transform modulus maximum lines (WTMML) are determined for each backscattering time series. Each individual WTMML is evaluated in order based on the following criteria:

1. *The WTMML must have a scale component that extends above a set minimum scale.* Signal noise, and noisy transition in backscatter produce WTMML only at small scales (i.e. high frequency). We set the minimum scale at 2^5. It was observed that using a scale of 2^3 similar to Liu et al (2005) could not eliminate all noisy transitions common during the melting season. This increased minimum scale relative to previous studies is expected since the enhanced resolution product contains more noise relative to other datasets (Ashcraft & Long, 2003; Spencer et al., 2003), and active microwave measurements (in comparison to the passive microwave data used in Liu et al., 2005) are more sensitive to liquid water content (LWC) and snow property changes.

2. *All |Wf| along the WTMML must have a value one order of magnitude (10x) greater than those measured during the winter season.* For areas experiencing melt, this condition does not have a large effect since *|Wf|* produced at all scales for a ~3dB transition in backscatter is many orders of magnitude greater than observed wintertime conditions. However, areas that experience snow property changes, but no seasonal melt, will produce WTMML with large scalar components since these changes are not "noisy" transitions and are temporally sustained. Since changes in LWC produce greater

differences in backscattering values compared to snow property changes (Ulaby & Stiles, 1980), we threshold the $|Wf|$ values of a WTMML, at all spatial scales, with a value one order of magnitude (10x) greater than observed wintertime conditions.

3. *The Holder exponent,α, of each WTMML must be equal to or greater than zero.* For reasons discussed in the previous section, we eliminate spike-like transitions in backscatter using a test of point-wise signal regularity.

All signal transitions that meet these 3 criteria that are considered to be melt related. To define the melting season, out of the set of melt related transitions, we select the WTMML (1) that has the greatest mean $|Wf|$ over all scales and (2) that extends to the largest scales. This WTML is matched with a corresponding transition of opposite magnitude, where refreeze must follow melt and melt must precede refreeze. This process is repeated until all melting WTMML are matched. The melt onset (MO) is defined as the first day of melting, and melt off (MF) is defined as the last melting day plus one. The melting duration (MD) at any pixel location is found as the sum of all days where melting occurs.

All computation for wavelet analysis is done using the MATLAB® numerical computing environment using the WaveLab 850 wavelet function library, distributed by Stanford University (www-stat.stanford.edu/~wavelab/). Due to the complexity of the melt-detection procedure, computationally intensive steps are coded through the MATLAB's parallel computing toolbox, and run using 8 processing-cores. In this configuration, 1 continent-scale melting-season requires 1 to 2 days of processing.

2.3.4 Threshold Based Methods

To create a dataset for comparison, a 3dB minus winter (JJA) mean backscatter approach, as used in Ashcraft and Long (2006) is applied to the identical QuikSCAT dataset. Melting events whose durations are shorter than 3 continuous days are removed from the melting record at each pixel following (S. Nghiem et al., 2007; Tedesco & Monaghan, 2009).

2.4 Data sets

2.4.1 SeaWinds on QuikSCAT

Enhanced spatial resolution melting products (gridded at 2.225 km) are derived from the enhanced resolution SeaWinds (commonly referred to by the satellite name, QuikSCAT) scatterometer dataset distributed by the Microwave Earth Remote Sensing (MERS) Laboratory at Bingham (BYU, http://www.mers.byu.edu/). The SeaWinds instrument is a conically scanning pencil-beam width scatterometer that takes normalized radar cross-section measurements (σ^0) in the Ku band (13.4 GHz). This instrument records both horizontal and vertical polarizations at two set observation, 46^o for H-pol. and 54.1 for V-pol (Long & Hicks, 2000). The effective ~7x30 km instantaneous field of view of the QuikSCAT range-Doppler processed 'slice' product (Spencer et al., 2003) is enhanced through a scatterometer image reconstruction algorithm (SIR) developed at BYU. By combining multiple observations that are weighed within with the senor's antenna function, the SIR algorithm can recover information attenuated at the antenna side-lobe, and thereby effectively increasing the spatial resolution of the standard scatterometer product *(Early & Long, 2001)*. This resolution enhancement is done at the expense of increased signal noise. In view of the strong change in measured backscatter following the insurgence of liquid water, this increase in noise does not likely affect melt detection considerably, hence allowing for the generation of a surface melting product (including extent and duration) at a gridded

spatial resolution of 2.25 km. In addition, the CWT method is well suited for noisy datasets since high frequency, noisy, transitions in backscatter are not likely to create WTMML that extends to large scales and those that do will decrease in $|Wf|$ with increasing scale, leading to negative Holder exponents (α). The CWT therefore will not consider signal noise as a possible melting event.

2.4.2 Automated Weather Station

Automated weather station data from the Antarctic Meteorological Research Center (AMRC) and Automatic Weather Station (AWS) program, maintained by the Space Science and Engineering Center at the University of Wisconsin, Madison (AMRC, SSEC, UW-Madison), is used to evaluate the results of the melt detection algorithms. This dataset contains continuous Antarctic climate observations, for some stations since 1980. For our comparison, we use the hand corrected 3-hr air temperature records, when available. AWS air temperature measurements are made using platinum resistance thermometer (PRT) that measure air temperature to within to 0.125 ºC with an accuracy of $\pm$0.05 ºC. The stations used in this study are: Larsen Ice Shelf (Lat: 67.01S Long: 61.55W Elev: 17 M), Uranus Glacier (Lat: 71.43S Long: 68.93W Elev: 780 M), Fossil Bluff (Lat: 71.33S Long: 68.28W Elev: 63 M), Butler Island (Lat: 72.21S Long: 60.17W Elev: 91 M), Pegasus South (Lat: 77.99S Long: 166.57E Elev: 5 M), and Limbert (Lat: 75.91S Long: 59.26W Elev: 40 M). For each AWS, 3-hour air-temperature measurements and backscatter are spatially and temporally co-registered using exact overpass times available from MERS-SCP.

Melting is assumed to occur when the mean daily air temperature is above the melting point, 0^{o}C. This criterion is often used to compare AWS air temperature datasets with satellite derived melt estimates (Steffen, Nghiem, Huff, & Neumann, 2004). For Antarctica, extreme fluctuations

in daily temperature prevent the daily mean temperature from exceeding 0^o though satellites observations indicate that melting is likely taking place. A sub-melting temperature threshold is often used to account for this fact (Tedesco & Monaghan, 2009; MR Van den Broeke et al., 2010). However, the mean daily temperature does not contain information on how long temperatures stay above the melting point, and has been found to be a less accurate measure of melt-water production in polar regions (van den Broeke, 2005). In addition to this, many factors besides ambient air temperature, including precipitation (Fettweis et al., 2010) and surface albedo (Tedesco et al., 2011) influence the occurrence of melt. As albedo decreases, from snow metamorphism, the absorption of solar also increases leading to additional melt. A temperature sensitivity analysis is presented in the supplementary section (**Figure A-7** through **Figure A-12**). Here, we take a simple approach and estimate melt by setting a threshold on the number hours per day when measured temperature exceeds 0^oC. We choose a threshold of 6 hours, equivalent to at least 2 daily above zero measurements for the 3hr corrected AWS air temperature dataset, rather than mean surface temperature. It is found that this choice does not have a large influence on the classification of melting from air temperatures. Using this AWS-specific positive melt hour threshold to create a validation dataset, we assess the outputs of the FT3 and CWT melt detection methods. In particular, we study the number of days when the remote sensing- and air temperature-based estimates agree (true-positive), the omission error, computed as the percentage of days when air-temperature indicates melting but the remote sensing-based approach does not (true-negative), and the commission, computed as the percentage of days when QuikSCAT indicates melting but this is not true from the analysis of air temperature (false-positive).

2.5 Results

In Figure 2-3 we show the maps of mean (2000 through 2009) seasonal melt duration (in number of days) obtained from the a) FT3 and b) CWT algorithms and c) their difference over the whole continent. Although the spatial patterns for MD are similar for both algorithms, systematic differences exist. The CWT based method shows a strong regional bias between areas of the Antarctic Peninsula (negative) and Dronning Maude Land (positive). There is an also a clear edge effect at substantial elevation gradients. These two trends are explained in the following. A quantitative analysis of these differences highlights that CWT produces an average MD value of 28 days, versus the 41 days obtained with the FT3 algorithm. The continent scale melt index (MI, defined as the melting subject to area times the number of melting days) obtained with the CWT approach is 2.971 $x10^7$ [day*km^2], a value greater than that obtained with the FT3 approach of 2.813 $x10^7$ [day*km^2]. When considering only melt extent (ME), the CWT algorithm estimates that 6.23 % of the total surface area of Antarctica is subject to at least one day of melting per season compared to the 8.14 % found using the FT3 method. In general, therefore, the CWT method estimates longer mean melting duration over smaller areas than the FT3 approach. MD values for each year are presented in the Appendix (**Figure A-2** and **Figure A-3**). Additionally, a comparison (ΔMD) of the melt duration for enlarged section of the Peninsula is also presented in more detail in the Appendix (**Figure A-4**).

As previously mentioned, we estimate the length of the melting season as the difference between melt off (MF) and melt onset (MO) dates. At a continental scale, the average MO value from the CWT approach is day 347 [day of the year, DOY] and in the case of the FT3 algorithm it is day 352. The difference between the MD obtained with the two approaches is small compared to the standard deviation (SD) of either method, being SD_{FT3} = 12 days and SD_{CWT} = 16 days. The

mean MF dates for the whole of Antarctica differ by 3 days, with the FT3 suggesting a later refreezing than the CWT approach. This indicates that although the CWT algorithm will identify a constantly earlier MO and later MF than the FT3 method. A more detailed view of MD, MO and MF over the Antarctic Peninsula are presented in the supplementary section (**Figure A-5** and **Figure A-6**).

In terms of melting duration, the maximum MD difference between methods (Figure 2-3c) is observed over areas of Eastern Antarctica near the Donning Maud Land. Here ΔMD, defined as MD_{FT3}-$MD_{CWT,}$ has an average of 25 day. This difference can be partially explained by the disparities in melting season length. Over the 10-year measurement record, the difference in mean season length (defined as MF minus MO), accounts for 14 percent of the observed difference in mean MD between methods. Therefore we reason that the majority of the disagreement between methods occurs within the melting season. By comparing the percentage of melt days per melting season length ((MF-MO)/MD), representing the percentage of days during melting season where melting is detected by either method, we find that the FT3 method detects melt for 65 % of the melting season while the CWT approach finds melt for 95 % of melting season days. The percentage of days that are classified as "wet" between the MO and MF produces a majority of the difference in MD observed between methods.

Over the Antarctic Peninsula (Figure 2-3b and c), in the regional mean-MD between methods are more similar in comparison with the rest of Antarctica. For the Antarctic Peninsula, the CWT method finds a mean MD value of 55 days, while the FT3 finds a mean MD value of 51 days. This similarity is mainly a result of the large variability in elevation for the Antarctic Peninsula that balances the elevation bias discussed in the following. From Figure 2-3a it is evident that the CWT finds greater MD values over the ice shelves of the Peninsula. From the analysis of ME

and MI values over the same areas we find that the CWT method produces higher values of MD but smaller MI than the FT3 approach, due to the greater melting extent found by the FT3 compared to that found by CWT.

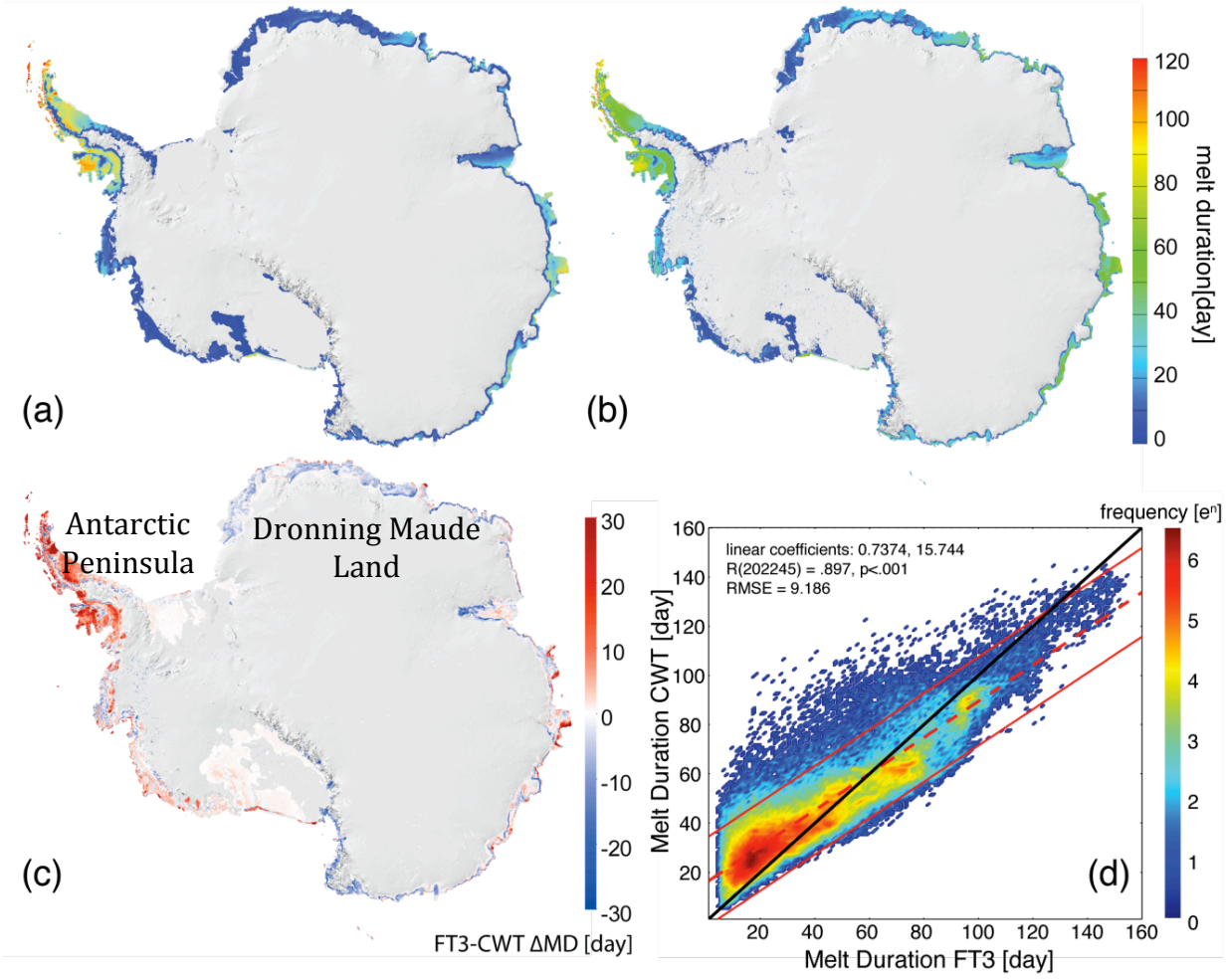

Figure 2-3 *(a) A map of mean (2000 through 2009) seasonal melt duration estimated from the SeaWinds sensor on QuikScat, using a 3dB below winter mean threshold (FT3) (b) and a continuous wavelet based method (CWT). (c)The difference between mean MD from both methods is indicated as* ***Δ****MD (FT3-CWT). The location of the Antarctic Peninsula (AP) and*

Dronning Maude Land (D) are labeled. (d) Autocorrelation analysis using a log transformed 2-axis histogram, where mean MD is compared for all areas where melt is detected by both methods

In terms of the melting season length over the Antarctic Peninsula, the mean melt onset (MO) date from the FT3 is found to be is 366 [DOY], while the mean MO for the CWT is 342 [DOY]. The MF values for the same areas are 411 [DOY] for the FT3 and 398 [DOY] for CWT. This indicates that the FT3 approach estimates a substantially longer (~20 days) melting season per year for the Antarctic Peninsula compared to the CWT. Much of this difference is due to an early melting onset.

The 10 year mean MD value per grid cell obtained with the FT3 method is plotted versus the same quantity obtained with the CWT method in Figure 2-3d. Results of a linear least square regression and autocorrelation analysis indicate that the results from the two algorithms are highly correlated $r = .897$ $(p < 0.001)$ with a root mean squared error (RMSE) of ~ 9 days. The CWT method finds larger MD values for areas that experience a short melting season (~MD 50 from the 1:1 line) and lesser MD in comparison with the FT3 approach for greater MD values. A bias of ~ 15 days exists between the two methods. The abundance of large magnitude CWT outliers (above the 95% confidence interval) indicates that the CWT may greatly overestimate MD, in a small percentage of cases, over all values of MD found by the FT3.

The larger mean MD estimated by the CWT is explained by the increased frequency of small temporal scale melting events detected by the FT3 methods (**Figure 2-4**a). Close to 5 % of MD values found by the FT3 are 10 days or less (**Figure 2-4**b). For the CWT method, this accounts for less than 1 % of all detected melting events. This indicates that the detection of short-duration melting events by the FT3 will lower the mean MD used in the previous comparison. As

evidence, a majority (>50 %) of MD for the FT3 method are under 27 days, compared to a 37 MD for the CWT method. Both methods are in agreement for longer duration MD, where close to 20 % of all MD for both methods are 60 days or over.

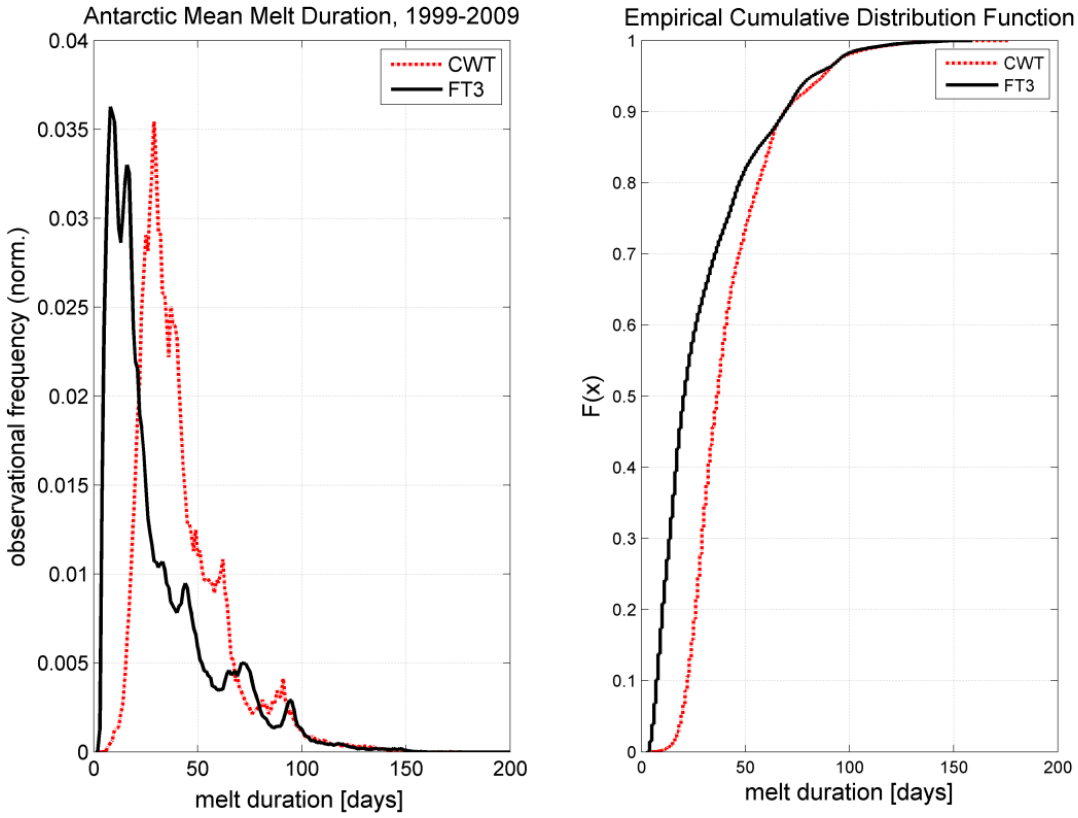

Figure 2-4 A histogram of seasonal (2000 through 2009) mean melt duration in days (a). An empirical cumulative density function of mean melt duration (b).

An analysis of the behavior of backscattering over a single melting season provides a better understanding of the differences between the two remote sensing algorithms. To this aim, we focus on a temporal analysis of melt extent for two regions of Antarctica, namely the Antarctic Peninsula and the coastal area of the Dronning Maude Land. We selected these areas because they exhibit the largest differences between the MD estimates from the two algorithms. For the

Peninsula during the 2004-2005 melting season, FT3 values (**Figure 2-5**a, solid gray line) exhibit an early season (November, 2004) peak value where melt extent reaches an extent of up to ~80 percent of the maximum yearly maximum melt extent for a period of less than 8 days. This transient melting event is not detected by the CWT approach (Figure 5a, dotted black line). A backscattering time series from the Antarctic Peninsula, over this same period, is plotted in Figure 5c. The melting season, as defined by both methods, is indicated by a shaded region for the CWT method, and by the location of the 3dB threshold for the FT3 approach. All normalized backscattering values below the 3dB threshold value are associated with the presence of melting conditions. From Figure 3c, we observe that the CWT approach excludes melting at the beginning of the season (outside of the shaded area). We point out that the histograms in Figure 2-5a and Figure 2-5b refer to regionally-averaged values where **Figure 2-5**c and **Figure 2-5**d refer to a single pixel within the melting season. **Figure 2-5**a and 5b show that, in general, the two methods find similar starting melting dates. The difference between the two methods over the Peninsula can be attributed to non-sustained short-term melting/refreezing events prior to and after the period when the majority of melting occurs. Additionally, it is clear that the melt onset date determined using the FT3 approach (defined as the first melting event greater than 3 days) will correspond to the brief November melting event. From the histogram it is apparent that after a brief melting event, more widespread melting may not occur again for several weeks.

type of discrepancy in melting accounts for the majority of the melting season differences observed between the FT3 and CWT methods. For the pixel under study, this will not create a considerable difference in MO or MF dates.

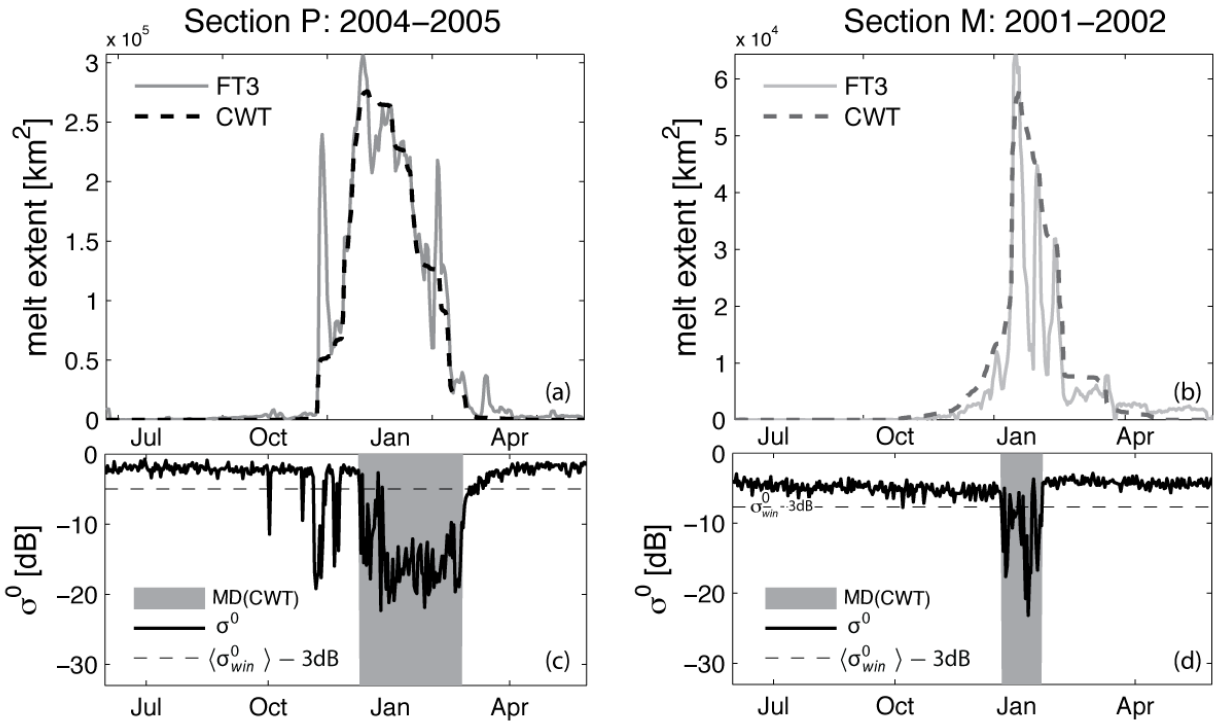

Figure 2-5 (a) A histogram of melt extent for the 2004-2004 melting season estimated using the FT3 and CWT methods over the Antarctic Peninsula and (b) one for during the 2001-2002 melting season for the Dronning Maude Land (Section M,b). Backscattering time series are plotted for (c) similar time series of a representative pixel location for the Peninsula and (d) Dronning Maude Land to illustrate the results of CWT (shaded) and FT3 methods (threshold indicated).

Similar plots for the Donning Maude Land are shown in **Figure 2-5**b and **Figure 2-5**d. In this case, the CWT method finds a higher value for MI with respect to the FT3 method. A sample backscattering time series (**Figure 2-5**d) indicates that while the FT3 method will generally record multiple melt/refreeze events, the CWT will record a single, longer melting event.

An analysis of the duration of melt-periods identified using the FT3 method, but not by the CWT, attempts to quantify the expected length of an isolated melting event eliminated in the

CWT method (i.e. the minimum number of days where the CWT will detect melting). As an example, **Figure 2-6** shows the normalized probability density (lines) and cumulative density (bars) as a function of the length of continuous of melting days obtained from the two approaches over the Antarctic Peninsula for the two selected years of 2003-2004 and 2005-2006; these seasons are selected to as an example of a relatively low and high melting index respectively. In 2003, ~ 60 % of MD values differ by only 1 day, ~ 20 % show differences of two days, with the remaining values differing by more than 6 days (~ 90 percent of observations are 6 days or less). These findings are similar to the temporal filtering methods used in previous melting studies to eliminate transient melting events (e.g., 3 days, S. V. Nghiem et al., 2001; Tedesco, 2009).

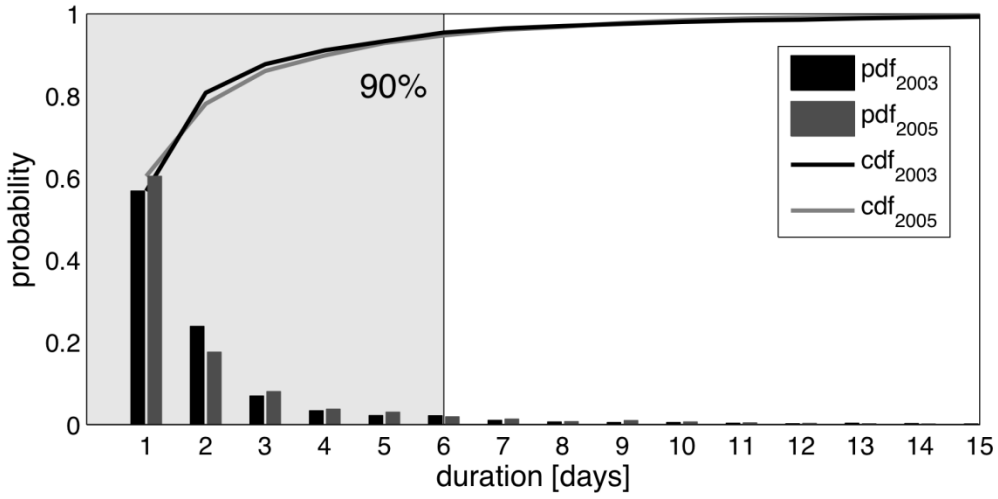

Figure 2-6 Probability density function (bar) and cumulative density function (line) of continuous melting periods per season observed over Antarctica (not the total per-pixel seasonal difference) that are found using a FT3 but rejected in by CWT.

We also performed an analysis aimed at identifying the performances of the two algorithms as a function of elevation. In **Figure 2-7** we show results differences between the outputs of the two approaches as a function of elevation for the Antarctic Peninsula, the Dronning Maude Land and the whole Antarctica. For the Dronning Maud Land area, the melt index difference between the two methods (MI_{FT3}- MI_{CWT}) is negative, independently from the elevation. For the AP however, the mean difference between methods is positive, and will vary with elevation. For areas that are 400 meters a.s.l. or less, the CWT method underestimates MI with respect to the FT3 method. Conversely, above 400 m. a.s.l., the MI difference becomes negative. Building on our previous analysis, we infer that melt processes are likely dominated by short melt-refreeze cycles at high elevations.

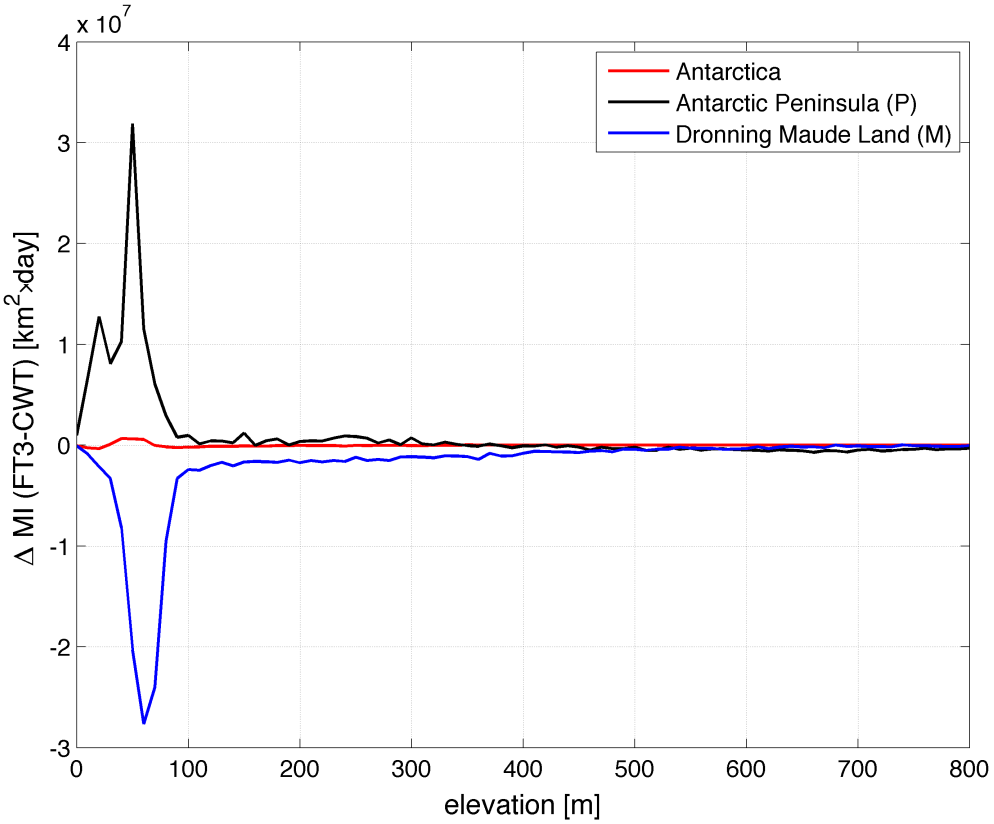

Figure 2-7 Difference between the melting index (MI) estimates from the FT3 and CWT (FT3-CWT) methods at a range of elevations for the entire Antarctic continent as well as the AP and Dronning Maude Land.

2.5.1 Comparison between QSCAT-based approaches and analysis of Automated Weather Stations

Results of the FT3 and CWT approaches are compared with estimates of melting derived from surface air temperatures measured by several automatic weather stations (AWS) (Larsen Ice Shelf, Fossil Bluff, Uranus Glacier, Butler Island, Limbert and Pegasus South). Due to the lack of in-situ liquid water content or snow temperature measurements, melt is estimated from AWS

air temperatures where the temperature is above zeros for at least 6 hours per day. The time series of co-registered backscattering, air temperature and positive temperatures are plotted in **Figure 2-8**. We compute the accuracy, commission, and omission percentages at each station (**Table 2-1**). Accuracy indicates the percentage of cases where surface temperature and spaceborne-based estimates both agree. Commission indicates when QuikSCAT indicates melting but this is not the case for the surface temperature; lastly, omission indicates those cases when the analysis of the surface temperature suggests melting but this is not detected according to the remote sensing algorithm. For those stations that experience at least 10 days of melt per year (Butler Island, Fossil Bluff and Larsen Ice Shelf stations), we find the highest rate of agreement between the remote-sensing and the AWS-based estimates. For these stations the FT3 approach performs slightly better (~ 10 percent) than the CWT approach. Of these, the Larsen Ice Shelf and Fossil Bluff stations show the highest overall agreement for both methods, averaging 87 percent (77 percent) and 75 percent (66 percent) for the FT3 (CWT) approach over the 1999 - 2009 period. The two stations generally display a large magnitude and sustained change in backscatter over the melting season (**Figure 2-8**a and b). For the Limbert, Butler Island and Uranus Glacier stations (**Figure 2-8**c, d and e), there is a higher degree of accuracy for the FT3, compared to the CWT approach, with differences up to 43 percent in accuracy. For these stations, the majority of melting occurs as short duration events. This is not the case during the 2002 and 2003 seasons for the Limbert and Uranus Glacier respectively, where the backscattering time-series experience a more substantial decrease in backscatter, here both methods are in good agreement with AWS estimates. From (**Figure 2-8**a and b) majority of the difference between methods, for these stations occurs at the beginning and end of the melting season. For the Pegasus South station, the CWT method is in better agreement with AWS

compared to FT3 with a 10 percent greater mean accuracy, although only accounting 48 percent of the estimated melt. Here, as opposed to the Limbert and Uranus Glacier station, melting over Pegasus South (**Figure 2-8**f) is expressed by a gradual, low magnitude and sustained decreases in backscatter over the summer season. This type of melting event is better identified using the CWT method. The Pegasus South station has the highest mean temperature, 2.16^{o}C, for all stations during melting estimated by AWS. The Pegasus South station also experiences an average loss of only 1.86 dB (from winter mean) during AWS defined melting. Only the Uranus Glacier station has a smaller backscatter change, of 1.80 dB with an average temperature of 0.79^{o}C during melting. In contrast, the Larsen Ice Shelf averages a loss of 15.07 dB with mean temperature of 1.06^{o}C during AWS defined melting.

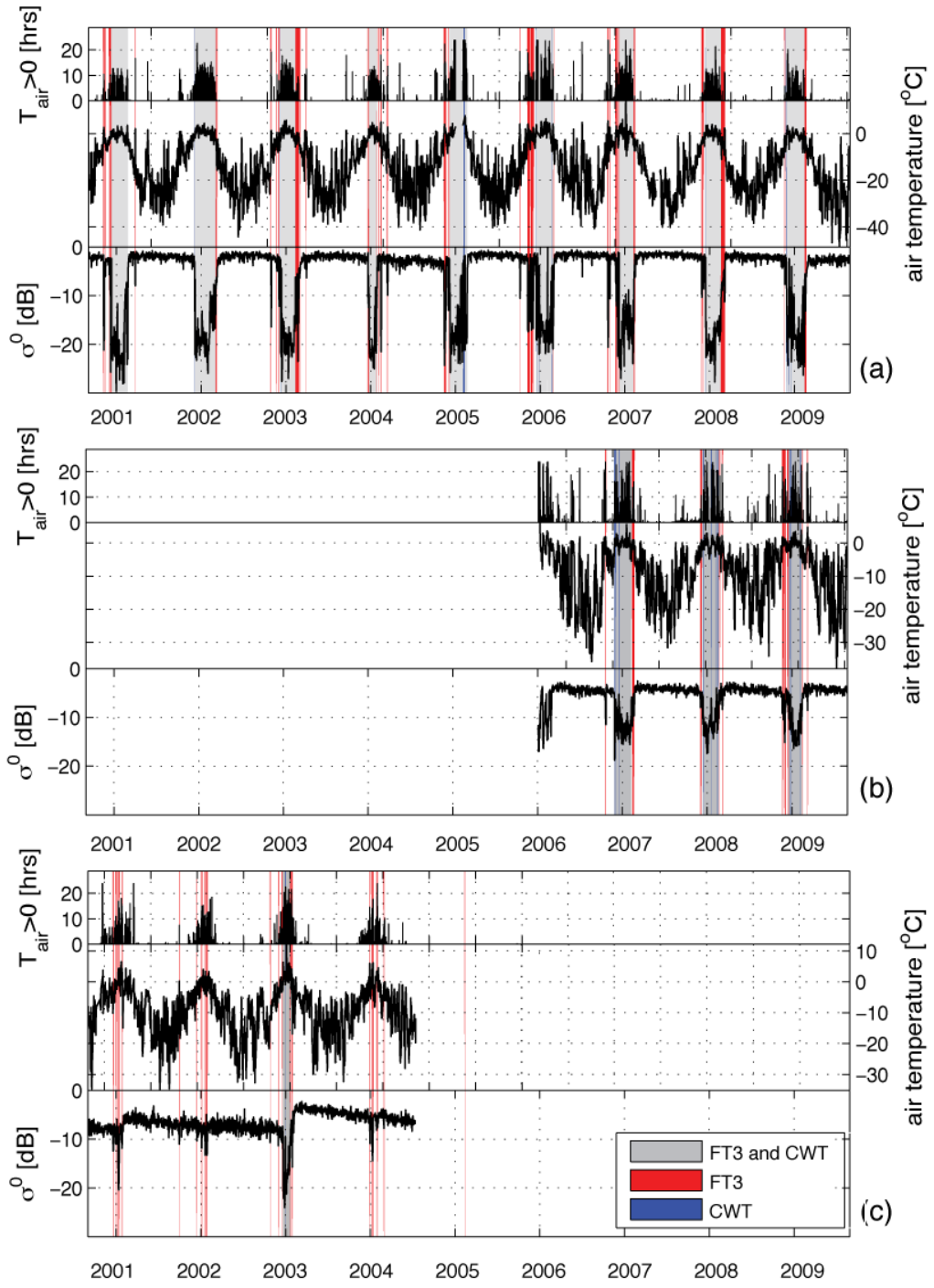
T_air>0 [hrs]
σ^0 [dB]
air temperature [°C]
(a)
(b)
(c)
2001
2002
2003
2004
2005
2006
2007
2008
2009
FT3 and CWT
FT3
CWT

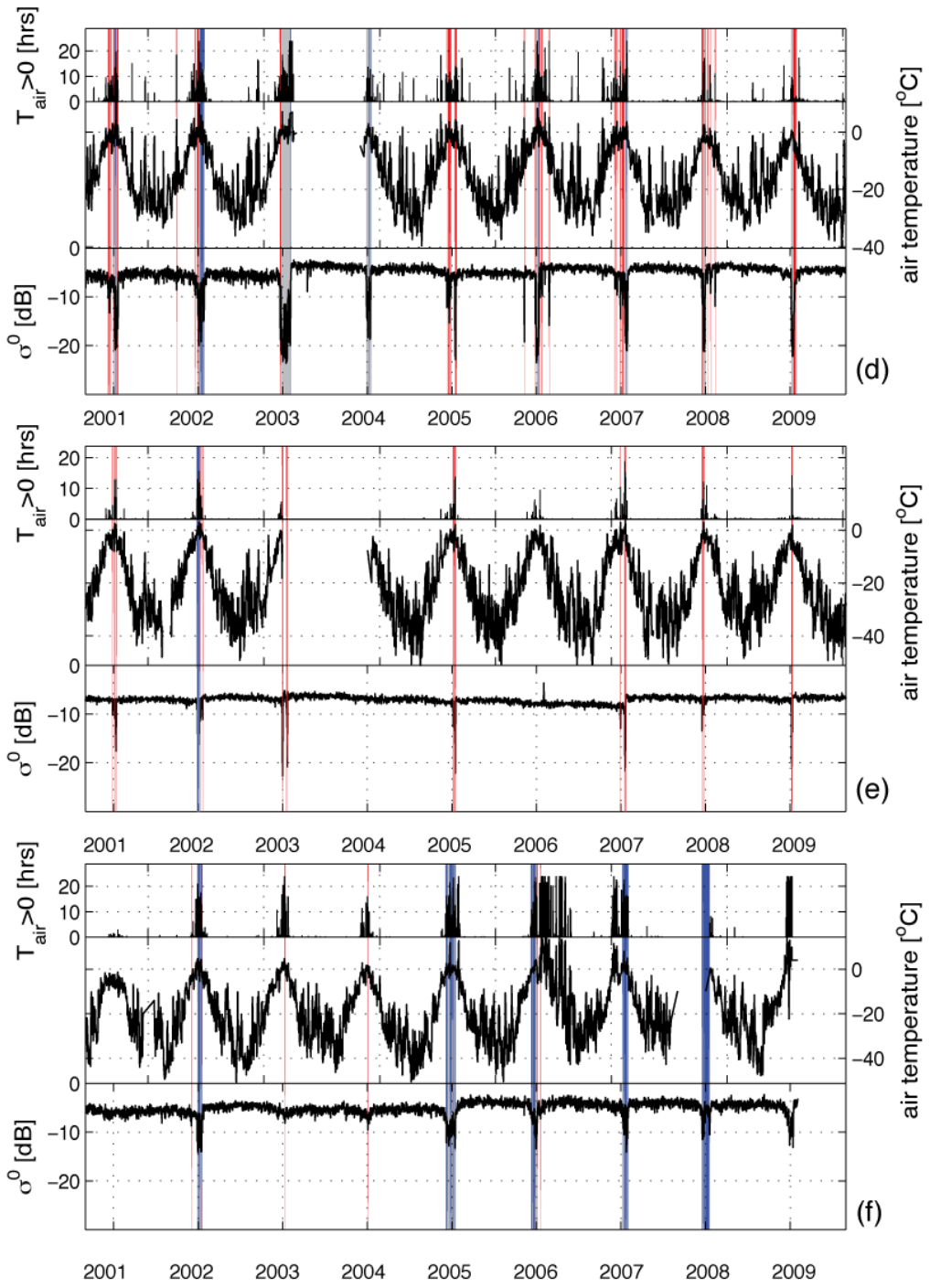

Figure 2-8 *AWS temperature records for the (a) Larsen Ice Shelf, (b), the Fossil Bluff, (c), the Uranus Glacier, (d) Butler Island, (e) Limbert and (f) Pegasus South for 2000 to 2009 plotted with the corresponding QuikSCAT backscattering values. Times where the FT3 or CWT*

approaches estimate melting are shaded red and blue respectively, while times where both methods agree are shaded grey.

In terms of omission errors, there is an average of 12 percent fewer false positives for the FT3 compared to the CWT. For the Limbert AWS, the CWT method has a maximum mean omission error for the CWT of almost 83 percent, compared to the FT3 at 40 percent. The Limbert Station has a short melting season, averaging close to 4 [days/yr] in length from AWS. A majority of these melting events are omitted using the CWT. Conversely, the FT3 approach detects these events with relatively high accuracy (83 percent). These findings are constant with the analysis presented on the ability of the CWT to detect short-duration melting events. A similar rate of omission is found at the Uranus Glacier AWS, again due to the omission of short-duration melting events. For the Larsen Ice Shelf station, we find the lowest rate of omission, averaging 34 (25) percent for the CWT (FT3). Commission errors are found to be small for both methods, averaging 3 percent for all stations for both the FT3 and CWT respectively. The largest commission errors for both methods are found for the Larsen Ice Shelf and Fossil Bluff stations, where the longest duration of melting per season is observed.

It should be noted that sporadic temperature increases related and precipitation will cause a decrease in the accuracy of the CWT method which is designed to detect longer duration temperature changes. From lack of precipitation data from AWS on Antarctica it is difficult to fully evaluate the effect of weather related melting versus temperature driven melting as in previous studies (Fettweis et al., 2011).

***Table** 2-1 Stations used in the AWS evaluation. The agreement (true-positive), omission (false-positive), and commission (true-negative) relative differences from the comparison of PDH threshold AWS air temperature time series and MD time-series estimated using the FT3 and CWT melt algorithms.*

	Accuracy				Omission Error				Commission Error			
AWS Station Name	FT3		CWT		FT3		CWT		FT3		CWT	
Butler Island	50%	(92/184)	30%	(55/184)	50%	(92/184)	70%	(129/184)	2.2%	(59/2708)	20.7%	(38/2708)
Fossil Bluff	75%	(123/164)	66%	(109/164)	25%	(41/164)	34%	(55/164)	9.9%	(91/923)	9.6%	(89/923)
Larsen Ice Shelf	87%	(413/477)	77%	(366/477)	13%	(64/477)	23%	(111/477)	10.3%	(285/2771)	8.6%	(238/2771)
Limbert	60%	(21/35)	17%	(6/35)	40%	(14/35)	83%	(29/35)	0.2%	(7/3225)	0.2%	(5/3225)
Pegasus South	38%	(46/121)	48%	(58/121)	62%	(75/121)	52%	(63/121)	0.6%	(14/2421)	1.2%	(28/2421)
Uranus Glacier	36%	(57/160)	17%	(27/160)	64%	(103/160)	83%	(133/160)	0.7%	(11/1641)	0.2%	(3/1641)
Total	66%	(752/1141)	54%	(621/1141)	34%	(389/1141)	46%	(520/1141)	3%	(467/13689)	3%	(401/13689)

2.5.2 Comparison with Passive Microwave Measurements

As an additional assessment of the CWT algorithm here proposed, we compare melting detected from passive microwave observations using approaches proposed in the literature with the outputs of both the CWT and FT3 methods. The SSM/I melting data are derived using two methods. The first is a fixed threshold approach as in Zwally and Fiegles (1994), here denoted as M+30K. The second dataset is produced using a dynamic electromagnetic modeling based detection approach as in Tedesco (2009, here denoted as MT09). Outputs from both methods are projected onto the 2.225 km QuikSCAT grid using nearest neighborhood interpolation method.

The values of seasonal integrated MI for Antarctica between all methods, both AMW and PMW are compared (**Figure 2-9**). For all methods, the PMW M+30K and the CWT approach have the most similar magnitude in seasonal MI, where the relative difference, $\frac{|MI_1 - MI_2|}{\frac{1}{2}(MI_1 + MI_2)}$ between these methods is the M+30K and CWT methods is 9 percent. This is only 2 percent greater than the difference between the CWT and FT3 methods (7 percent). There is a slightly greater relative difference between the FT3 and M+30K of 11 percent. The MT09 method finds on average, a 40 percent greater MI than the FT3 method, and 35 percent greater than the CWT. Results for MI for both AMW methods for all years are presented in the Appendix (**Figure A-13**).

For individual seasons, all methods find a MI maximum during the 2004-2005 melting season. The active and passive methods, however, do not agree on the year of minimum MI. Both the CWT and FT3 approaches find a minimum MI during the 1999-2000 seasons while the passive methods find a minimum during the 2008-2009 seasons.

Based on a comparison of temporal trends, a high degree of correlation is found between all methods. The correlation between the M+30K and the CWT methods have r = .943 ($p<0.001$) and a root mean squared error (RMSE) of 2.74×10^6 [day-km^2]. Between the FT3 and M+30K approaches, r = .922 (p=0.001) and RMSE = 3.10×10^6 [day-km^2] (**Figure 2-9b**). When compared with both active datasets, the MT09 method find an r = .931 (p=0.001) with a RMSE of 2.48×10^6 [day-km^2], and when compared to the FT3, and a r = .911 (p =0 .002) with a RMSE = 2.91×10^6 [day-km^2] for the FT3. For both PMW methods, we find a greater degree of correlation with the CWT and lower RMSE than the FT3.

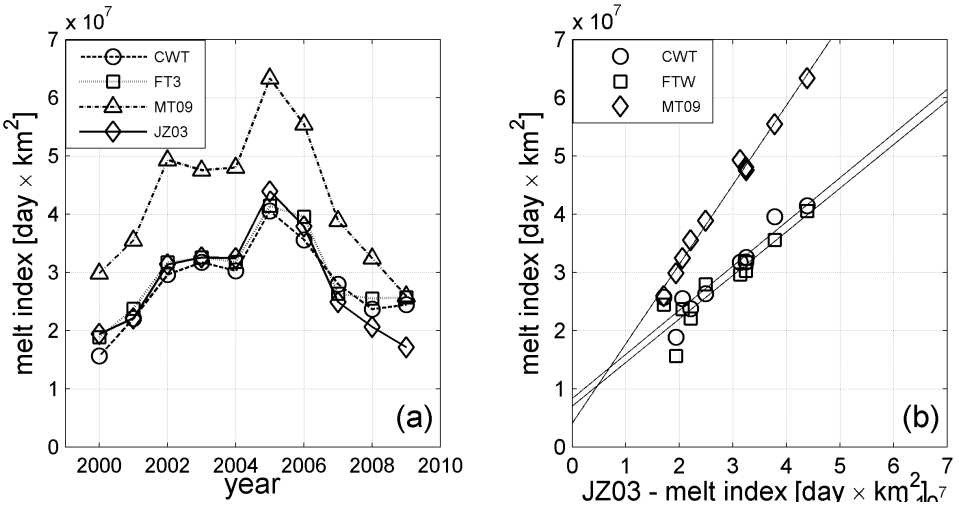

Figure 2-9 *The time series of total melt index (MI), in day-Km^2 for the Antarctic continent plotted for the years 1999 through 2009 derived from the FT3 and CWT methods on an enhanced resolution QuikSCAT active microwave dataset along with estimates from the MEMLS and M+K30 methods and a SSM/I dataset (a). The correlation between the FT3, QuikSCAT dataset MI estimates and the CWT, M+K30 and MEMLS methods indicated using a linear regression.*

The spatial differences between the mean MD estimated using the M+30K approach and the CWT (**Figure 2-10**a) and the FT3 (**Figure 2-10**b) reveals some patterns in the magnitude of difference between methods (ΔMD). Over large ice-shelves (e.g. the Larsen, and Amery), the difference of MD between the M+30K and FT3 approaches is close to +10 days for most areas (**Figure 2-10a**). Over the same regions, the difference of MD between the M+30K and the CWT algorithms difference closer to +20 days (**Figure 2-10**b). The tendency for the PMW data to overestimate AMW estimates (close to +10 or +20 ΔMD in most cases) is usually bordered, to some degree, by an area of underestimation by the PMW measurements. Melting for Antarctica generally occurs at ice-ocean boundaries or in many cases as at areas with sharp contrast in elevation. For these cases mixed pixel effects will likely lead to a decrease in the observed brightness temperatures of melted areas. For example, over the coastal regions of the Dronning Maude Land we find positive ΔMD bordered negative ΔMD. These negative ΔMD are found adjacent to ocean pixels and high elevations, and are likely due to a mixed pixel effect. In another example, the relatively narrow King George VI (lat:-71.965, lon:-67.807) ice shelf, located roughly east of Wilkens Ice Shelf (lat:-67.525, lon:-62.775), appears to increase the apparent MD of the surrounding high elevation areas for the PMW case, resulting in a large positive ΔMD. Since mixed pixel effects dominate the spatial differences between methods, it is difficult to determine a relationship between MD methods over similar areas other than the positive ~10 (FT3) and ~20 (CWT) reported previously.

An analysis of the spatial autocorrelation between the methods using the active microwave datasets and the M+30K method indicates that the FT3 has a higher degree of correlation with the passive microwave M+30K method, with $r = .782$ ($p<0.001$) (**Figure 2-10**c). The CWT method has an autocorrelation of $r = .665$ ($p<0.001$) with the M+30K (**Figure 2-10**d). Both

AMW methods find a RMSE of close to 14 days in comparison with the M+30K. The CWT method finds a 13 day positive bias with respect to the M+30K, whereas for the FT3 method the bias is 3 days. Artifacts in the scatter plot (**Figure 2-10**c and **Figure 2-10**d), in this case vertical stripes of data points, indicate a high degree of variability for many pixels with similar MD as detected using the M+30K. These artifacts are most likely due to the difference in spatial resolution, and a result of the mixed pixel effect previously discussed. From visual interpretation of **Figure 2-10**c and **Figure 2-10**d, and comparison of r values, we can see a larger component of the melt dataset for the FT3 method falls along the 1:1 line. For the CWT method, points appear are biased towards a larger M+30K at for longer MD. It also appears that the CWT method find greater MD for shorter durations, evident by a cluster of points 0 to 50 MD for CWT and 0 to 20 for M+30K. This relationship is similar to the on observation between AMW methods. The relatively strong agreement between AMW and PMW integrated melting extent indicates that the high sub-pixel variability is averaged out when integrated for the entire dataset.

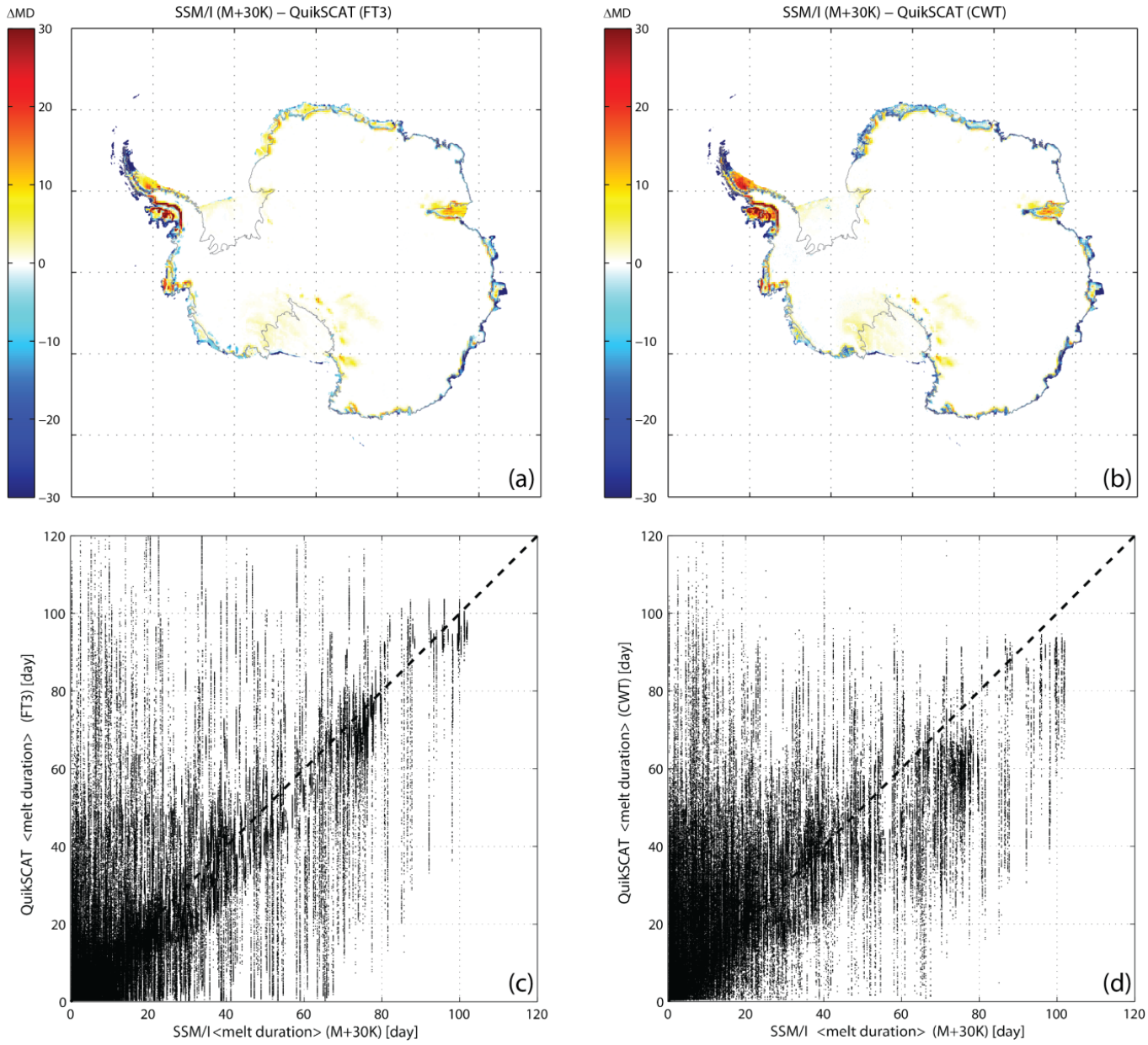

Figure 2-10 *The difference in average melt duration (ΔMD), over the period of 1999-2009, between the up-sampled passive microwave, SSM/I dataset, where melt is estimated using the M+K30 approach and the enhanced resolution QuikSCAT scatterometer dataset, where melt is estimated using the FT3 (a) and CWT (b) methods. Per-pixel scatter plots of average melt duration between SSM/I (M+30K) and the FT3 (c) and CWT (d) approaches.*

2.5.3 **Antarctic Melting and the Southern Antarctic Mode**

The Southern Hemisphere Annual Mode (SAM) is a measure of the atmospheric pressure gradient between the middle and high latitudes (Thompson & Wallace, 2000). The SAM index is determined by the mean monthly zonal sea level pressure difference between the 40^{o} and 65^{o} South latitude (Marshall, 2003). A positive SAM index generally coincides with lower than normal near surface temperatures for Antarctica, leading to a continent scale negative correlation between SAM index and melting over Antarctica (Tedesco & Monaghan, 2009). Positive SAM conditions have been linked to an increase in the westerly flow over the AP, due to the development of a consistent low pressure area to the east of the AP (Marshall et al., 2011). This low pressure system causes an increase in the advection of warmer air to the western edge of the AP. In some cases this warmer air will flow over the Transantarctic Mountains (overflow conditions) to areas of the eastern AP (Van Lipzig et al., 2008). This process is assumed to increase the magnitude of melting for the Eastern Antarctic Peninsula (Marshall, et al. 2011). A regression between the SAM index, averaged from December through February, and yearly MD from CWT and FT3 at each pixel location indicates a strong negative correlation between melting and SAM over several regions of Antarctica. Specifically, there is increased melting during negative SAM conditions for the Amery Ice Shelf and the Dronning Maud Land coast (Appendix Figure 25 and 26) among other areas. This is in agreement with findings from Tedesco and Monahan (2009).

Over the AP, Tedesco and Monahan (2009) find a weak negative correlation between regionally averaged melting for the Antarctic Peninsula and SAM conditions. From correlations found using the QuikScat AMW dataset and SAM on a per-pixel basis (not regionally averaged) we find that correlation with SAM is spatially variable (**Figure 2-11**). For the western and eastern

Antarctic Peninsula ice shelves we find a moderate, positive, correlation with SAM for both the CWT and FTW methods. At higher elevations we find a moderately negative correlation with SAM that is most apparent using threshold-based methods for melt detection. For the eastern AP, the CWT method finds a strong positive correlation with SAM conditions close to the Transantarctic Mountains, while the FT3 does not. In terms of the melting season, it is found that there is also a moderate, but not statistically significant at 95 percent, correlation with early MO detected by the CWT method (averaged over the AP) and positive SAM (r = .57, p = 0.09). This is not the case with the FT3method (r = .05, p = 0.15). This indicates that positive SAM conditions may increase the persistence of the melting season for east AP, when warmer advected air leads to an increased temperature and wind speed.

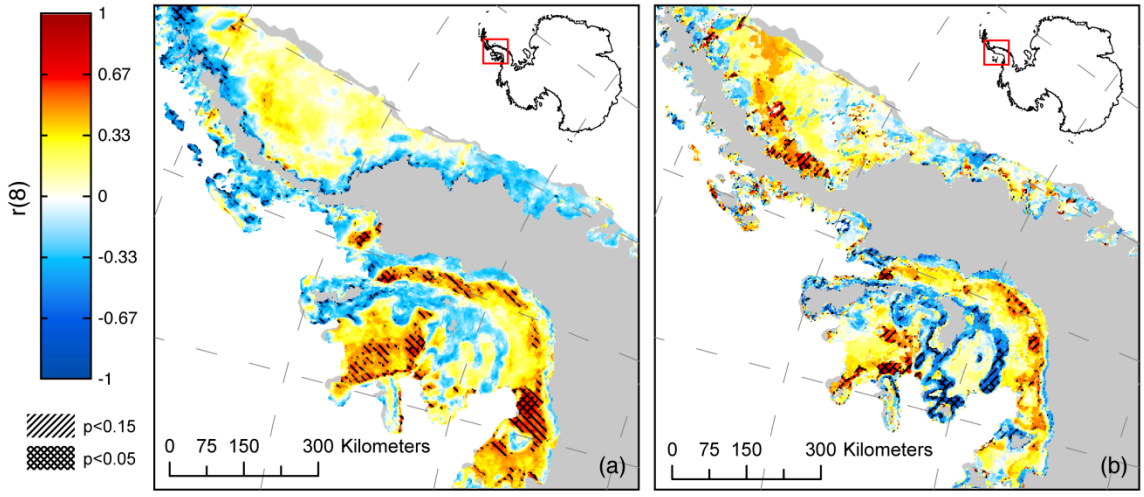

Figure 2-11 *Correlation between SAM(DecJanFeb) and MD for the (a) FT3 method and (b) CWT. Areas with moderate or strong correlations are indicated with hash marks.*

2.6 Summary and Conclusion

The use of a combined continuous wavelet transform and multi-scale analysis (CWT) is able to detect changes in the backscattering signal upon an increase in LWC. This is due to the fact that CWT methodology can identify all discontinuous changes in the data-series including the point of melt onset and refreeze. Further, a simple test of the signal regularity, at the point of backscatter change can be estimated using the Holder exponent. This measure, α, allows for a simple classification of edge "types" based on ideal cases in the literature. Sporadic type changes in normalized backscatter are then separated from those that persist over time using this classification. Using the CWT method also allows for the identification of all scale components of a given backscatter change, so that thresholding is not limited to a single scale. By comparing all scales to observed "dry" signal changes, we can remove the effect of sporadic changes in the backscatter.

From comparison with results using a well-established, fixed threshold methodology (FT3, e.g. Ashcraft and Long, 2006), we assessed the CWT approach proposed in this study. The estimated MD derived from these methods are well correlated, $r = .897$ $(p < 0.001)$ with a root mean squared error (RMSE) of ~ 9 days. Additionally, the CWT method has a positive bias of ~ 15 days with respect to the FT3. It is found that the mean melting season length, estimated in both methodologies agrees within 2 days for the 1999 through 2009. In terms of total mean melting index, these methodologies agree to within 3 percent. However, for the average melt duration, it is found that there is as a 19 percent difference, where the CWT method averages 13 days longer MD in comparison. Since the mean melting extent of the CWT is observed to be smaller than the FT3, the agreement in MI and disagreement in MD must result from a more sustained melting during the melting season. Overall, we find that the minimum melting duration that the CWT

detects, at the minimum scale threshold of 2^5 days, is 6 days in duration, and found by comparing the observational frequency of omitted melting durations by the CWT method. Close to 10 percent of FT3 MD are of small duration (under 10 days in length). This accounts for only 0.1 percent of the melting events detected by the CWT method.

These trends have some regional variability. Over the Dronning Maude Land, we find similar season lengths, but a difference in mean MD of 25 days. A majority of this difference can be attributed to differences in the percent of the season the experiences melt as defined by both methods. For the CWT, close to 95 percent of the days within the melt season show melting, while with the FT3 we observe only 65 percent. From single season observations, we find that this difference is due to fluctuations in backscatter close to the 3dB threshold found in the FT3 method. These changes are most likely due to short refreeze cycles. The CWT will not consider these changes in backscatter since rapid fluctuations do not produce WTMML that increase with scale. It will then define the melting season based on the initial and final transition of the melting season.

From evaluation of melting over the Antarctic Peninsula for both methodologies, it is found that the average MD difference is less than at the continent scale, having a 5 day greater MD found by the CWT method. When observing the season length, there is an apparent early melt onset detected by the FT3 method, 12 days before the CWT. This earlier seasonal melt onset most likely caused by small duration early season melting events, as illustrated during the 2004-2005 season, where the melt index reaches ~80 percent of its maximum seasonal value for close to 8 days. It is shown that the CWT method does detect melting over an equivalent extent until several weeks later. This general tendency of the CWT to omit large scale early and late season melting events accounts for a greater estimated mean MI, 4 percent larger than the FT3 method.

This difference in MI is greatest for low elevation areas and generally decreases with higher elevations. This indicates that a majority of sporadic, large-scale, melting events occur for low elevation ice-shelf regions and that at higher elevations melting is rapid melt/refreeze cycles similar to the Dronning Maude Land.

From a comparison with AWS, we find that overall the FT3 has higher level of agreement with the temperature measurements with a 66 percent total accuracy compared to the 54 percent from the CWT method. This is true for all AWS, apart from the Pegasus South Station where the CWT has a 10 percent greater accuracy than the FT3 method. The FT3 method has a better accuracy in general because of its ability to measure short duration melting events that are common for several stations (e.g. Limbert). For the Pegasus South AWS, it appears that the melting season occurs with a relatively low loss in backscatter, it is therefore never consistently under the 3dB threshold. This lowers the accuracy of the FT3 method, but does not affect the CWT approach.

Compared to M+30K, a PMW derived approach; both AMW melting records find a similar yearly MI, where the FT3 is within 11 percent and the CWT within 9 percent relative difference. These methods find a greater level of disagreement with a dynamic thresholding approach, MT09. The CWT methods find a greater overall agreement in temporal trend for both PMW methods, for the M+30K method $r=.943$ ($p<0.001$) with CWT and $r=.922$ ($p=0.001$) for the FT3 method. Spatially, we find that comparison is dominated by a mixed pixel effect, making it difficult to determine the difference between melt duration on a per-pixel basis. The FT3 method has a higher degree of spatial autocorrelation with PMW (M+30K) approaches than the CWT, with significant variability in AMW derived MD for similar PMW measurements. Since PMW pixels are ~10 times the scale of the spatially enhanced QuikSCAT product we attribute this

variability to mixed pixel effects. Based on the strong correlation in yearly MI totals, the differences in spatial variability appear to be averaged out over the total area.

From all comparisons between AMW methods, it is found that the major difference in melting estimates are for small scale melting events, those under 9 days. This is expected using a CWT-based method since at the set minimum scale of 2^5 days, these events are not sustained, and appear to be 'spike'-like transitions. Apart from these differences, the novel approach agrees with a fixed threshold to within 7 percent in total MI and to within 10 percent accuracy based on AWS comparisons. In addition, this method appears to detect MO of a sustained melting season, unaffected by early melting events. By detecting only sustained melting events, we are able to show linkages with SAM indices not detected using threshold based approaches.

2.7 References

Addison, P. S. (2005). Wavelet transforms and the ECG: a review. *Physiological measurement, 26*, R155.

Ashcraft, I. S., & Long, D. G. (2003). *The spatial response function of SeaWinds backscatter measurements*.

Ashcraft, I. S., & Long, D. G. (2006). Comparison of methods for melt detection over Greenland using active and passive microwave measurements. *International Journal of Remote Sensing, 27*(12), 2469-2488.

Bromwich, D. H., & Nicolas, J. P. (2010). Sea-level rise: Ice-sheet uncertainty. *Nature Geoscience, 3*(9), 596-597.

Chen, J., Wilson, C., Blankenship, D., & Tapley, B. (2009). Accelerated Antarctic ice loss from satellite gravity measurements. *Nature Geoscience, 2*(12), 859-862.

Dowdeswell, J. A. (2006). The Greenland ice sheet and global sea-level rise. *Science, 311*(5763), 963.

Early, D. S., & Long, D. G. (2001). Image reconstruction and enhanced resolution imaging from irregular samples. *Ieee Transactions on Geoscience and Remote Sensing, 39*(2), 291-302. doi: 10.1109/36.905237

Fettweis, X., Tedesco, M., van den Broeke, M., & Ettema, J. (2010). Melting trends over the Greenland ice sheet (1958–2009) from spaceborne microwave data and regional climate models. *Cryosphere Discuss, 4*, 2433-2473.

Fettweis, X., Tedesco, M., van den Broeke, M., & Ettema, J. (2011). Melting trends over the Greenland ice sheet (1958–2009) from spaceborne microwave data and regional climate models. *The Cryosphere [= TC], 5*.

Herrmann, F. J. (2001). Singularity characterization by monoscale analysis: Application to seismic imaging. *Applied and Computational Harmonic Analysis, 11*(1), 64-88.

Joshi, M., Merry, C. J., Jezek, K. C., & Bolzan, J. F. (2001). An edge detection technique to estimate melt duration, season and melt extent on the Greenland ice sheet using passive microwave data. *Geophysical Research Letters, 28*(18), 3497-3500.

Kunz, L. B., & Long, D. G. (2004). *Melt detection in Antarctic ice-sheets using spaceborne scatterometers and radiometers*.

Le Gonidec, Y., Conil, F., & Gibert, D. (2003). The wavelet response as a multiscale NDT method. *Ultrasonics, 41*(6), 487-497.

Lemke, P., Ren, J., Alley, R. B., Allison, I., Carrasco, J., Flato, G., . . . Thomas, R. H. (2007). Observations: Changes in snow, ice and frozen ground. *Titel: Climate change 2007: the physical science basis; summary for policymakers, technical summary and frequently asked questions. Part of the Working Group I contribution to the Fourth Assessment Report of the Intergovernmental Panel on Climate Change*, 337-383.

Li, C., Zheng, C., & Tai, C. (1995). Detection of ECG characteristic points using wavelet transforms. *Biomedical Engineering, IEEE Transactions on, 42*(1), 21-28.

Liu, H., Wang, L., & Jezek, K. C. (2005). Wavelet-transform based edge detection approach to derivation of snowmelt onset, end and duration from satellite passive microwave measurements. *International Journal of Remote Sensing, 26*(21), 4639-4660.

Long, D. G., & Hicks, B. R. (2000). Standard BYU QuikScat/SeaWinds land/ice image products. *Brigham Young Univ., Provo, UT, QuikScat Image Product documentation*.

MacAyeal, D. R., Scambos, T. A., Hulbe, C. L., & Fahnestock, M. A. (2003). Catastrophic ice-shelf break-up by an ice-shelf-fragment-capsize mechanism. *Journal of Glaciology, 49*(164), 22-36. doi: 10.3189/172756503781830863

Mallat, S., & Zhong, S. (1992). Characterization of signals from multiscale edges. *IEEE Transactions on pattern analysis and machine intelligence, 14*(7), 710-732.

Mallat, S. G. (1999). *A wavelet tour of signal processing*: Academic Pr.

Marshall, G. J. (2003). Trends in the Southern Annular Mode from observations and reanalyses. *Journal of climate, 16*(24), 4134-4143.

Marshall, G. J., Di Battista, S., Naik, S. S., & Thamban, M. (2011). Analysis of a regional change in the sign of the SAM–temperature relationship in Antarctica. *Climate Dynamics, 36*(1), 277-287.

Nghiem, S., Steffen, K., Neumann, G., & Huff, R. (2007). *Snow accumulation and snowmelt monitoring in Greenland and Antarctica*.

Nghiem, S. V., Steffen, K., Kwok, R., & Tsai, W. (2001). Detection of snowmelt regions on the Greenland ice sheet using diurnal backscatter change. *Journal of Glaciology, 47*(159), 539-547.

Picard, G., Fily, M., & Gallee, H. (2007). Surface melting derived from microwave radiometers: a climatic indicator in Antarctica. *Annals of Glaciology, 46*(1), 29-34.

Rignot, E., & Thomas, R. H. (2002). Mass balance of polar ice sheets. *Science, 297*(5586), 1502.

Shepherd, A., & Wingham, D. (2007). Recent sea-level contributions of the Antarctic and Greenland ice sheets. *Science, 315*(5818), 1529.

Spencer, M. W., Tsai, W. Y., & Long, D. G. (2003). High-resolution measurements with a spaceborne pencil-beam scatterometer using combined range/doppler discrimination

techniques. *Ieee Transactions on Geoscience and Remote Sensing, 41*(3), 567-581. doi: 10.1109/tgrs.2003.809938

Steig, E. J., Schneider, D. P., Rutherford, S. D., Mann, M. E., Comiso, J. C., & Shindell, D. T. (2009). Warming of the Antarctic ice-sheet surface since the 1957 International Geophysical Year. *Nature, 457*(7228), 459-462.

Taubman, D. S., Marcellin, M. W., & Rabbani, M. (2002). JPEG2000: Image compression fundamentals, standards and practice. *Journal of Electronic Imaging, 11*, 286.

Tedesco, M. (2009). Assessment and development of snowmelt retrieval algorithms over Antarctica from K-band spaceborne brightness temperature (1979-2008). *Remote Sensing of Environment, 113*(5), 979-997.

Tedesco, M., Abdalati, W., & Zwally, H. J. (2007). Persistent surface snowmelt over Antarctica (1987-2006) from 19.35 GHz brightness temperatures. *Geophysical Research Letters, 34*(18). doi: L18504

10.1029/2007gl031199

Tedesco, M., Fettweis, X., Van den Broeke, M., Van de Wal, R., Smeets, C., van de Berg, W. J., . . . Box, J. (2011). The role of albedo and accumulation in the 2010 melting record in Greenland. *Environmental Research Letters, 6*, 014005.

Tedesco, M., Kim, E. J., England, A. W., De Roo, R. D., & Hardy, J. P. (2006). Brightness temperatures of snow melting/refreezing cycles: Observations and modeling using a multilayer dense medium theory-based model. *Geoscience and Remote Sensing, IEEE Transactions on, 44*(12), 3563-3573.

Tedesco, M., & Monaghan, A. J. (2009). An updated Antarctic melt record through 2009 and its linkages to high-latitude and tropical climate variability. *Geophys. Res. Lett, 36*, L18502.

Thompson, D. W. J., & Wallace, J. M. (2000). Annular Modes in the Extratropical Circulation. Part I: Month-to-Month Variability*. *Journal of climate, 13*(5), 1000-1016.

Torinesi, O., Fily, M., & Genthon, C. (2003). Variability and trends of the summer melt period of Antarctic ice margins since 1980 from microwave sensors. *Journal of climate, 16*(7), 1047-1060.

Turner, J., Colwell, S. R., Marshall, G. J., Lachlan-Cope, T. A., Carleton, A. M., Jones, P. D., . . . Iagovkina, S. (2005). Antarctic climate change during the last 50 years. *International Journal of Climatology, 25*(3), 279-294.

Ulaby, F. T., & Stiles, W. H. (1980). THE ACTIVE AND PASSIVE MICROWAVE RESPONSE TO SNOW PARAMETERS .2. WATER EQUIVALENT OF DRY SNOW. *Journal of Geophysical Research-Oceans and Atmospheres, 85*(NC2), 1045-1049. doi: 10.1029/JC085iC02p01045

van den Broeke, M. (2005). Strong surface melting preceded collapse of Antarctic Peninsula ice shelf. *Geophysical Research Letters, 32*(12). doi: L12815 10.1029/2005gl023247

Van den Broeke, M., Bus, C., Ettema, J., & Smeets, C. (2010). Temperature thresholds for degree-day modelling of Greenland ice sheet melt rates. *Geophysical Research Letters, 37*(18), L18501/18501-L18501/18505.

Van Lipzig, N. P. M., Marshall, G. J., Orr, A., & King, J. C. (2008). The relationship between the Southern Hemisphere Annular Mode and Antarctic Peninsula summer temperatures: Analysis of a high-resolution model climatology. *Journal of climate, 21*(8), 1649-1668.

Wang, L., & Yu, J. (2011). Spatiotemporal Segmentation of Spaceborne Passive Microwave Data for Change Detection. *Geoscience and Remote Sensing Letters, IEEE*(99), 909-913.

Wang, L. B., Derksen, C., & Brown, R. (2008). Detection of pan-Arctic terrestrial snowmelt from QuikSCAT, 2000-2005. *Remote Sensing of Environment, 112*(10), 3794-3805. doi: 10.1016/j.rse.2008.05.017

Zwally, H. J., & Fiegles, S. (1994). EXTENT AND DURATION OF ANTARCTIC SURFACE MELTING. *Journal of Glaciology, 40*(136), 463-476.

In-situ multispectral and bathymetric measurements over a supraglacial lake in western Greenland using a remotely controlled watercraft

A version of the following section has been published:

Tedesco, M., & Steiner, N. (2011). In-situ multispectral and bathymetric measurements over a supraglacial lake in western Greenland using a remotely controlled watercraft. The Cryosphere, 5, 445-452.

3 In-situ multispectral and bathymetric measurements over a supraglacial lake in western Greenland using a remotely controlled watercraft

3.1 Abstract

Supraglacial lakes form from meltwater on the Greenland ice sheet in topographic depressions on the surface, affecting both surface and sub-glacial processes. As the reflectance in the visible and near-infrared regions of a column of water is modulated by its height, retrieval techniques using spaceborne remote sensing data (e.g. Landsat, MODIS) have been proposed in the literature for the detection of lakes and estimation of their volume. These techniques require basic assumptions on the spectral properties of the water as well as the bottom of the lake, among other things. In this section, we report results obtained from the analysis of concurrent in-situ multi-spectral and depth measurements collected over a supraglacial lake during early July 2010 in West Greenland (Lake Olivia, 69º36'35"N, 49º29'40"W) and aim to assess some of the underlying hypotheses in remote sensing based bathymetric approaches. In particular, we focus our attention on the analysis of the lake bottom albedo and of the water attenuation coefficient. The analysis of in-situ data (collected by means of a remotely controlled boat equipped with a GPS, sonar and a spectrometer) illustrates the exponential trend of the water-leaving reflectance with lake depth. The attenuation factor values obtained from in-situ measurements are compared with those computed from approaches proposed in the literature. Also, the lake bottom albedo values from in-situ measurements are compared with those obtained from the analysis of

reflectance from shallow waters. Finally, we quantify the error between in-situ measured and satellite-estimated lake depth values for the lake under study.

3.2 Background and rationale

Monitoring the spatio-temporal variability of such lakes over the Greenland ice sheet (GrIS) can benefit studies concerning ice sheet dynamics (*Das et al., 2008, Joughin et al., 1996, Pimentel and Flowers, 2010*) and surface features (e.g., *Lüthje et al., 2006*) and can help understanding their link with recently observed increased surface melting (*Tedesco et al., 2011)*. Recently, several approaches based on the interpretation of visible and near-infrared satellite data have been proposed for estimating supraglacial lake depth (*e.g., Georgiou et al. 2009, Box and Ski, 2007). McMillan et al*. (2007) use satellite imagery to study the evolution of 292 lakes over an area of 22000 km^2; *Sundal et al.* (2009) analyze 268 cloud-free Moderate Resolution Imaging Spectroradiometer (MODIS) images; *Sneed and Hamilton* (2007) estimate the depth of selected lakes based on Advanced Spaceborne Thermal Emission and Reflection radiometer (ASTER) atmospherically corrected reflectance values.

The reflectance of a water column limited by a reflecting bottom can be approximated with the reflectance of the same water body in absence of a bottom plus the bottom contrast, after this contrast has been modulated by the depth of the bottom through an attenuation factor (*Philpot, 1989, Maritorena, 1994*). *Box and Ski (2007)* use MODIS atmospherically corrected reflectance values to compute lake area and volume for those pixels where the presence of a lake is detected. In their study, a pixel is classified as lake if the MODIS band 1 (620 – 670 nm) reflectance is below 0.6 and the ratio $R_{b3/b1}$=band3/band1 is greater than 1.25 (with band 3 being 459 – 479 nm). Moreover, those pixels with reflectance values of the band 6 greater than 0.15 are excluded

from the analysis to reduce the impact of cloud cover (*Box and Ski, 2007)*. For those pixels where a lake is detected, lake depth is then estimated using a regression formula obtained from the fitting of in-situ lake depth measurements to satellite reflectance values. The main advantage of the method proposed by *Box and Ski (2007)* lies in its low computational cost. However, results are based on a limited number of measurements over selected lakes and the extension of the method to other areas would require further validation and assessment. A physically-based retrieval has been proposed by *Sneed and Hamilton (2007).* This is the approach that will be used in this study as it offers the opportunity of evaluate some of the theoretical assumptions adopted in the retrieval scheme. The approach is briefly described and discussed in the following.

For retrieval purposes, the following hypotheses on the bottom albedo *Ad* and on the attenuation factor *g* are made: (*hyp. 1*) in the absence of actual measurements the value of *Ad* is assumed to be uniform and (*hyp. 2*) *Ad* is estimated from reflectance values of shallow waters along the lake edge *(e.g., Sneed and Hamilton, 2007);* the attenuation factor *g* is computed assuming that (*hyp. 3)* suspended or dissolved organic or inorganic particulate matter is minimal and that *(hyp. 4)* a linear relationship exists between the attenuation factor and the diffuse attenuation coefficient (e.g., *Maritorena, 1994)*. Measurements of organic, chlorophyll and suspended minerals by *Sneed and Hamilton (2007)* confirmed that concentrations are appreciably small (less than 1 mg/L). Similar concentrations were confirmed by our analysis of water samples collected from different lakes. Though spectrally similar to the diffuse attenuation coefficient for downwelling light *Kd, g* and *Kd* cannot be used interchangeably and a possible range of $1.5\ Kd < g < 3\ Kd$ is suggested by *Philpot (1989)* in the case of strongly absorbing waters. The value of Kd differs from g in that it accounts for the for directional scattering dependencies (Mobley, 2004). The value of $g \approx \alpha \cdot Kd$ with $\alpha = 2$ has been used by *Sneed and Hamilton (2007*) and *Maritorena et al.*

(1994), with the latter warning that such a choice will lead to an unquantifiable underestimation of the actual attenuation.

Focusing on the bottom albedo *Ad, Sneed and Hamilton (2007)* and *Georgiou et al. (2009)* suggest that the dominant uncertainty derives from the selection of *Ad*. As said, for this parameter the assumption of a uniform distribution over the lake area is used for retrieval purposes and its value is estimated by from the pixels adjacent to those showing a rapid decrease in the red band *(Sneed and Hamilton, 2007)*. In other words, because of the relatively small attenuation in the green and blue bands with respect to the red band, the bottom albedo *Ad* is assumed to be spectrally similar to the pixels where water is shallow, at the edge of the lake.

The assumptions applied to the estimation of *Ad* and the choice of α are a source of uncertainty on the accuracy of lake depth retrieval from spaceborne data. Here we report, for the first time, in-situ concurrent spectral and depth data collected over a supraglacial lake in West Greenland by means of instruments mounted on a remotely controlled boat. We analyze the spatial distribution of *Ad* to assess the hypothesis of its spatial uniformity and compare *Ad* mean values with those obtained from shallow waters at the lake edge. We also study the spectral dependency of both *Ad* and *g* obtained from in-situ measurements and compare their values against those obtained using literature approaches. This analysis is extended to satellite methods for the estimates of lake depth from either the Landsat and MODIS sensors with those obtained in-situ, quantifying the uncertainty of current procedures for multispectral bathymetry of supraglacial lakes.

3.3 Supraglacial lake bathymetry from visible data.

In the following, we briefly summarize the equations used for estimating lake depth from visible

data, together with the hypotheses behind the retrieval scheme.

The expression for reflectance immediately below the water surface for optically shallow, homogeneous water is given by (*Philpot, 1989*):

$$R(0^-) = R_\infty + (Ad - R_\infty) \exp(-gz) \qquad (1)$$

where *Ad* is the irradiance reflectance (albedo) of the bottom, $Ad = Eu(z)/Ed(z)$, with *Eu* being the upwelling irradiance and *Ed* the downwelling irradiance at depth z, and R_∞ is the irradiance reflectance of an optically deep water column. Solving *Eq. 1* for *z* gives:

$$z = -(\ln(Ad - R_\infty) - \ln(R(0^-) - R_\infty))/g \qquad (2)$$

The coefficient *g* accounts for losses in both the upward and downward directions and is given by $g \approx Kd + aDu$ (*Philpot, 1989*), where *Kd* is the diffuse attenuation coefficient for downwelling light, *a* is the beam absorption coefficient, and *Du* is an upwelling light distribution function or the reciprocal of the upwelling average cosine (*Mobley, 2004*). According to *Philpot (1989)*, the two attenuation coefficients *g* and *Kd* are spectrally similar as long as the diffuse attenuation is not dominated by scattering. However, *Kd* and *g* cannot be used interchangeably and a possible range of $1.5\ Kd < g < 3\ Kd$ can be assumed in the case of strongly absorbing waters. *Philpot (1989)* approximates $g \approx 2Kd$, for purposes of computation based on studies over a range of coastal waters (*Table I, Philpot 1989*). We use the values of the diffuse attenuation coefficient *Kd* of optically pure water by *Pope and Fry (1997*).

3.4 The remotely controlled boat and the instruments

A commercially-available remotely controlled boat (http://www.viperfishing.co.uk/Site/Viper_Storm_2.html, **Figure *3-1***) was customized and

equipped with a GPS/sonar (HDS-5 Lowrance), an above-surface irradiance sensor for incoming solar radiation, a below-surface downward looking radiance sensor, a spectrometer (Ocean Optics) and a micro-computer (used to synchronize the data from the different instruments). The boat is made of glossy acrylic capped ABS and propelled by dual jet-pump engines. Lake depth was measured by means of a 50/200 kHz transducer. The depth uncertainty was estimated to be of the order of 20 – 30 cm by testing the set up in a swimming pool before the shipping and deployment to Greenland. However, the uncertainty on depth might be higher than the one obtained in the pool because of the roughness of the bottom of the supraglacial lake, which might be responsible for multiple echoes. The boat is designed to carry loads up to 6 Kg and is controlled remotely up to a distance of 1000 m, making it ideal for our application. The original design of the boat was altered and customized to accommodate our needs with specific parts of the watercraft machined at our laboratory. The decision to use a remotely controlled boat, as opposed to a manned watercraft, aimed to eliminate life-threatening risks associated with a possible rapid drainage of the lake *(e.g., Das et al., 2008)*.

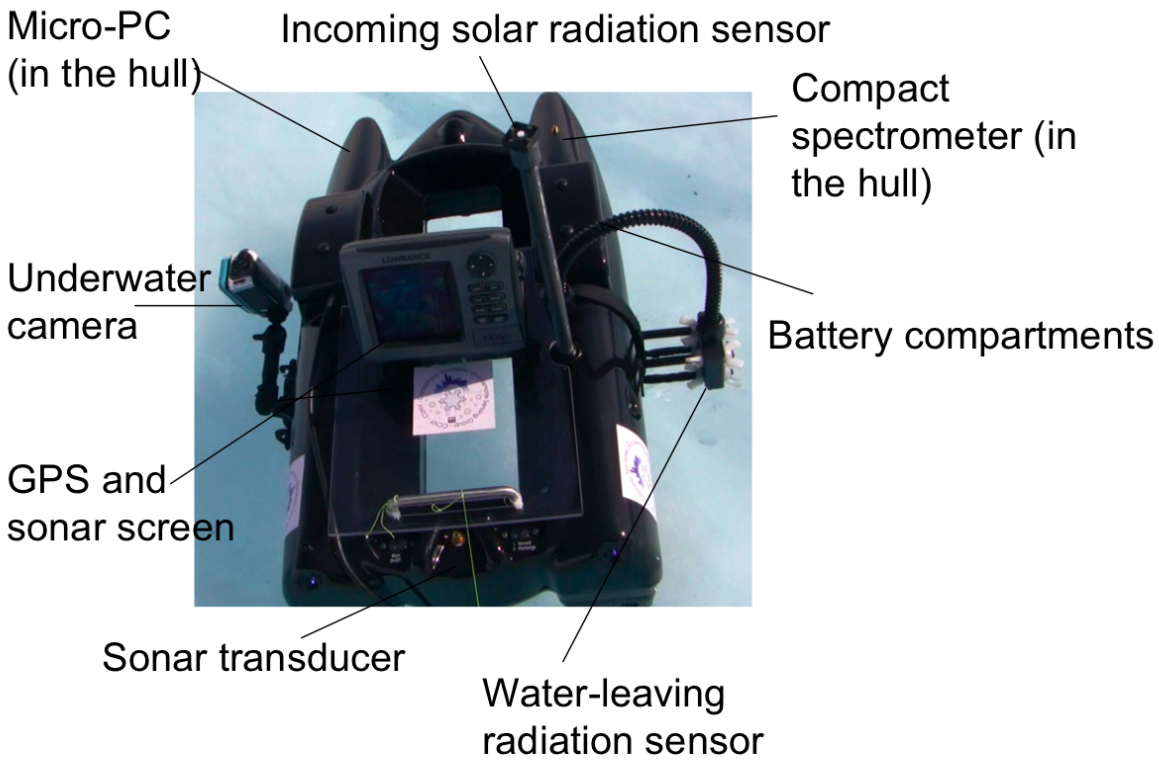

Figure 3-1 *The customized remotely controlled boat with labeled instrumentation*

The boat was deployed on July 2nd, 3rd and 5th, 2010, on the west margin of the GrIS (Lake Olivia, 69º36'35"N, 49º29'40"W), with deployment time usually occurring when the sun was at zenith and measurements lasting for a few hours. As the boat average speed was 1 m/s and the GPS data were recorded every second, we estimate a spatial resolution of 1 m for the in-situ data. The spectral (450 – 1050 nm, with a 0.3 nm resolution) and depth data collected between two subsequent GPS acquisitions were averaged and assigned to the first of the two GPS locations. The total number of samples used in our analysis is ~ 6000. Although, the boat used for this study is much smaller than manned boats and casts a relatively small shadow, we acknowledge that this shadowing might still be a source of uncertainty. During the maneuvering of the boat,

we paid attention in avoiding that the boat would not cast a shadow across the instrumental field-of-view while driving it. Another mitigating factor includes the use of an arm mounted on the side of the boat in order to position the spectral sensor at a certain distance from the hull. Ideally, measurements for bathymetric studies should be taken normal to the water surface as this will change the depth of the observed water column as well as alter the optical parameters used in depth retrieval .In future studies observation angle measures will be collected using electronic sensors to compensate for off-normal data collection.

The irradiance and radiance sensors were cross-calibrated in the laboratory following *Mueller (2003)*. The diffuse irradiance leaving the outlet of an integrating sphere, illuminated by a calibrated xenon lamp, was measured by the irradiance sensor directed at the outlet. Radiance measurements were then taken of a Spectralon © target (99 % reflectance) put in place of the irradiance sensor. The spectral intensity measured by each sensor is shown in **Figure *3-2***. These measurements were used to derive a spectral response factor (F), plotted in **Figure *3-3***, that allows for the calculation of reflectance from irradiance (E_+) and radiance (L_-) intensity measurements and cross-calibrate the two sensors. The calibration coefficient is then derived using the spectral response factor estimated in the previous step (**Figure *3-4***).

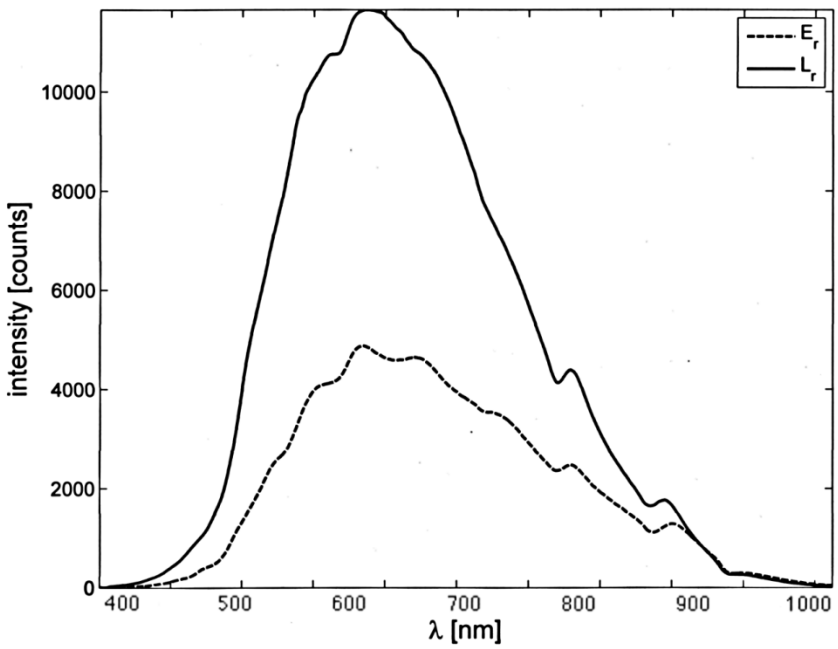

Figure 3-2 *Measured spectral intensity in counts, from an integrating sphere, illuminated by a xenon light source for both optical sensors. The cosine collector irradiance intensity (E_r) is measured directly from the integrating sphere port, while the radiant intensity (Lr) is measured from the surface of a Spectralon plate at an equivalent distance.*

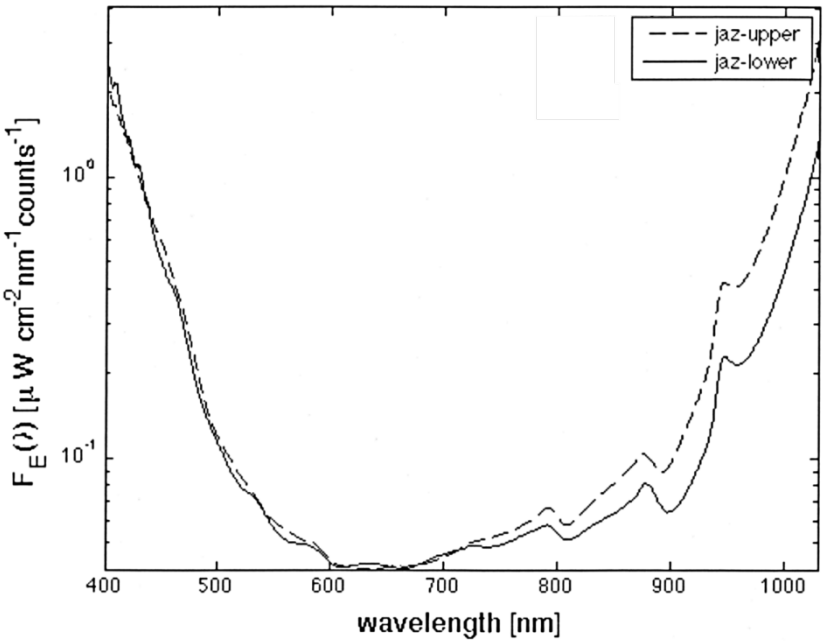

Figure 3-3 The calculated spectral response factor (F_E), in irradiance per count**.** F_E values are plotted on a logarithmic scale.

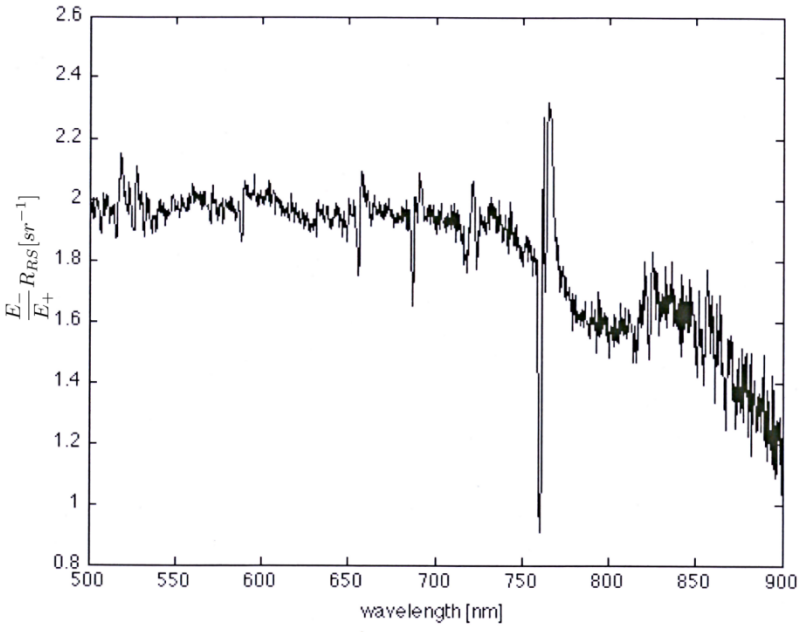

Figure 3-4 Spectral calibration factor used to convert the measured and calculated irradiance ratio (E_+/E_-) to remote sensing reflectance (R_{RS}).

Though spectral data were collected up to 1050 nm, we focus our analysis on the 450 - 650 nm range. The reason for this choice is related to the strong absorption (e.g., low reflectance) at wavelengths above ~ 650 nm. As shown in the literature (*e.g., Sneed and Hamilton, 2007)*, this can be used to increase the sensitivity to lake detection with respect to the use of wavelengths around or below 650 nm. However, the strong absorption in the near-infrared region compromises the use of such band for depth retrieval. Because in this study we are mostly interested in assessing lake depth retrieval, rather than lake detection, we focus on wavelengths below 650 nm. We also note that, as a consequence of the strong absorption by water in the near infrared region, in-situ spectral measurements in that band for lake depth above a few tens of centimeters were characterized by an extremely low signal/noise ratio (e.g., comparable to the

dark current measurement) therefore, excluded from our analysis. Measurements for lake depth values less than 1 m are also excluded from our analysis because of the relatively small sensitivity of the reflectance data in the Landsat and MODIS blue and green bands to shallow waters.

The measured reflectance upwelling just below the pond surface should be consistent between boat deployments, since the optical properties of the water and lake bottom should not change significantly over a short period. Therefore the magnitudes of measured reflectance in bandwidths corresponding to the MODIS blue (Band 3) and green (Band 4) channels, as well as the autocorrelation between these values should also remain constant. Upon comparison of red and green channels, (**Figure *3-5***) for July 2nd, July 3rd and July 4th, the large degree of difference in absolute reflectance magnitude is apparent, although reflectance autocorrelation remains constant as expected. The disparity between reflectance values observed during July 4th leads us to exclude this dataset from consideration.

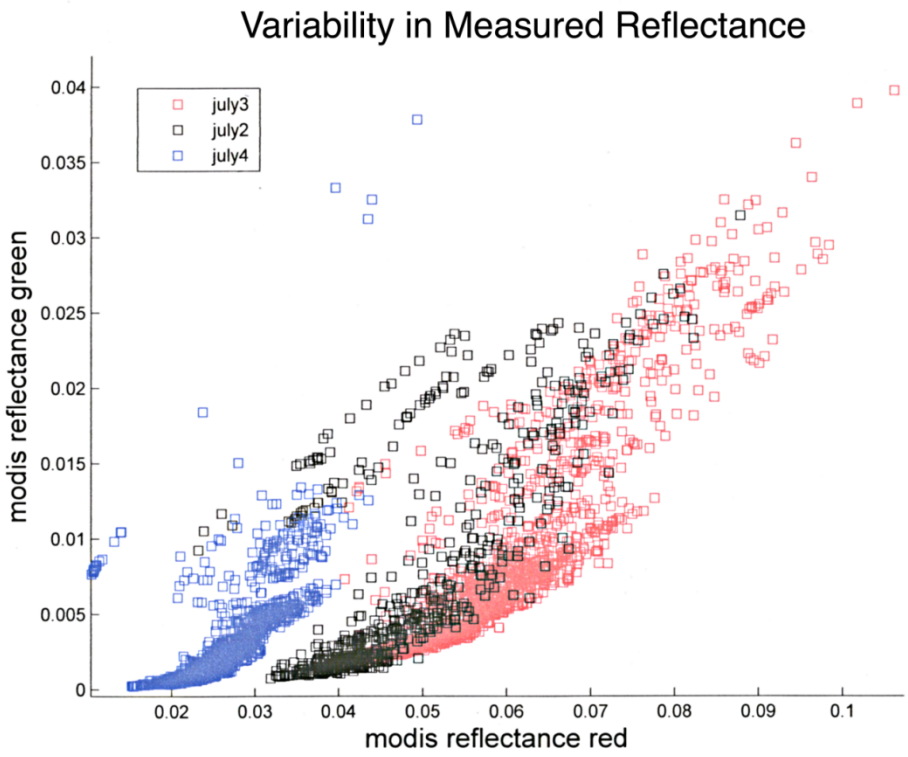

Figure 3-5 Spectral correlation and variability in in-situ reflectance, collected over Lake Olivia on the 2nd, 3rd and 5th of July 2010, over the wavelengths corresponding to the blue (Band 3) and green (Band 4) MODIS channels.

3.5 Analysis of in-situ data

The boat paths and the corresponding measured depth are superimposed in **Figure *3-6*** on a high-resolution (0.5 m) image collected on July 4th, 2010 by the WorldView-2 sensor (http://worldview2.digitalglobe.com/). Shallow waters are generally located along the edge of the lake, with depth increasing toward its center, up to ~ 4.5 m.

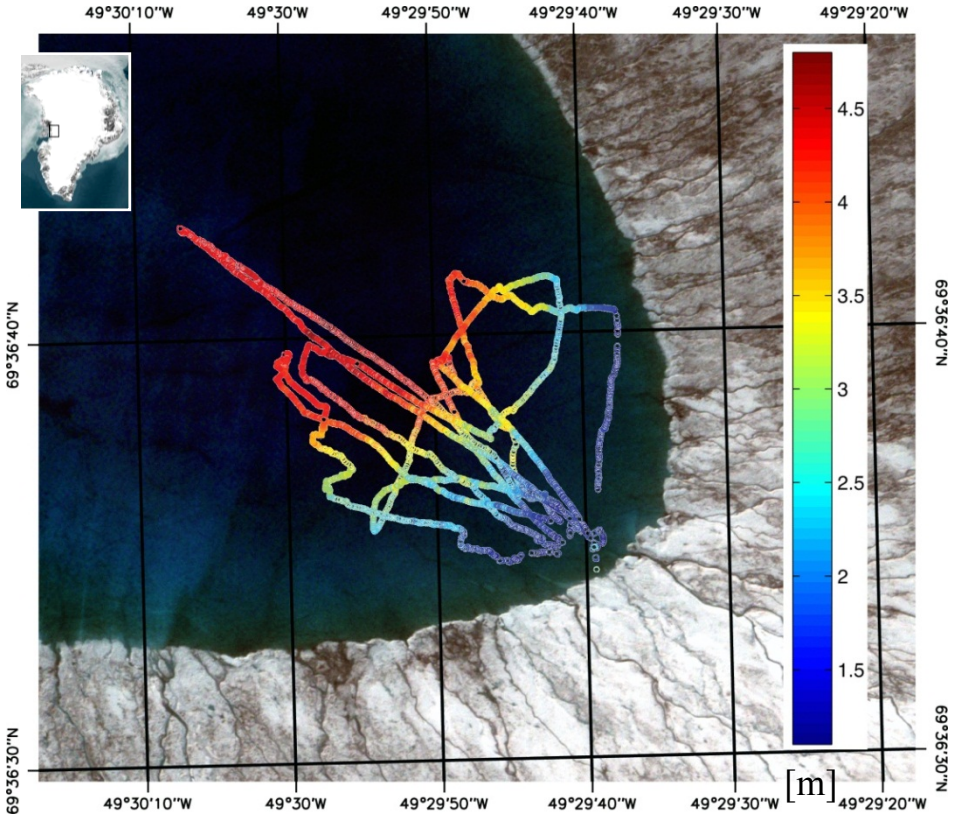

Figure 3-6 Boat paths and measured depth values imposed over a high-resolution (0.5 m) Wordlview-2 image.Reflectance measurements made over these depths, are plotted as Landsat EMT+ bandwidth matching histograms in Figure 3-7 and MODIS bandwidths in Figure 3-8.

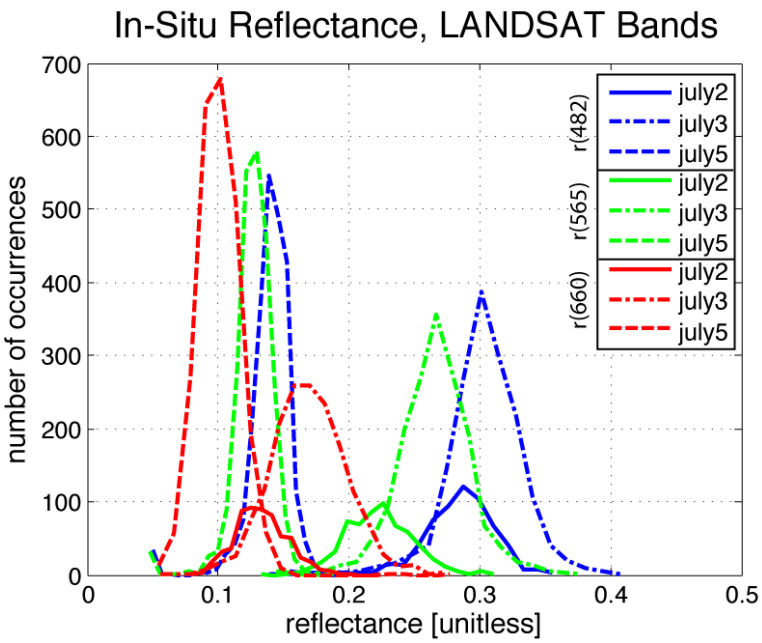

Figure 3-7 Histogram of measured in-situ reflectance over wavelengths corresponding to LANDSAT EMT+ bands 1, 2 and 3. These measurements are separated by measurement day: July 2nd, July 3rd and July 5th**.**

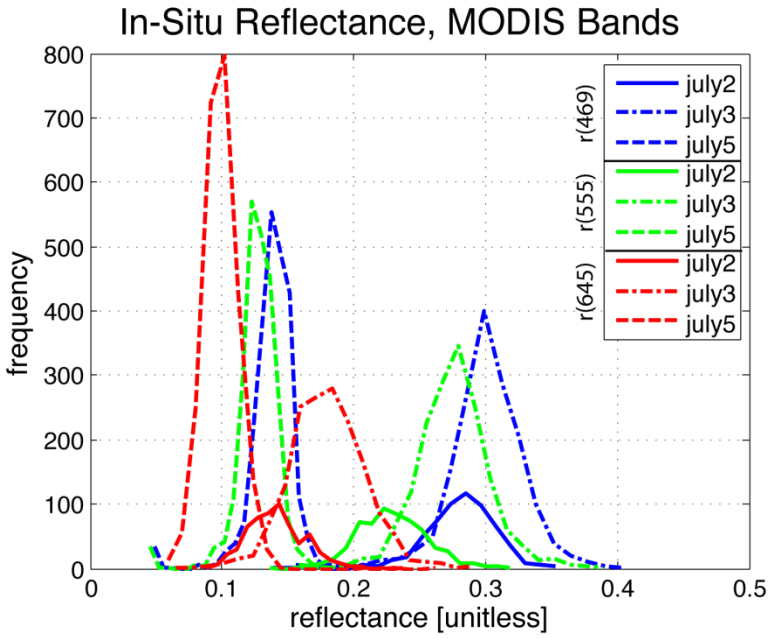

Figure 3-8 Reflectance histogram, to the previous figure, although using wavelengths corresponding to MODIS bands 1, 3 and 4.

In I (as well as **Figure *3-10***, **Figure *3-11***, **Figure *3-12***, **Figure *3-13*** and **Figure *3-14***) we plot the in-situ water-leaving reflectance spectrally averaged over the Landsat band 1 ($B1_{LANDSAT}$, 450 – 515 nm), band 2 ($B2_{LANDSAT}$, 525 – 605 nm) and band 3 ($B3_{LANDSAT}$, 630 – 690 nm) vs. the in-situ measured lake depth. In-situ measured water-leaving reflectance is fitted with Eq. 1, using *Ad, g* and R_∞ as free fitting parameters. The values obtained for *g* are: $g_{B1\_LANDSAT\_fit}$=0.023 m^{-1}, $g_{B2\_LANDSAT\_fit}$=0.24 m^{-1} and $g_{B3\_LANDSAT\_fit}$=0.81 m^{-1}. The corresponding *g* values obtained assuming $g=2Kd$ (with *Kd* obtained from *Pope and Fry, 1997)* are $g_{B1\_LANDSAT\_2Kd}$=0.045 m^{-1}, $g_{B2\_LANDSAT\_2Kd}$=0.21 m^{-1} and $g_{B3\_LANDSAT\_2Kd}$=0.65 m^{-1}. The fitted values of *g* are consistent with those computed assuming $g=2Kd$, though differences exist.

To address these differences, we analyzed the spectral dependency of the bottom albedo *Ad*

and of the coefficient α. **Figure *3-15***a and 15b show, respectively, the values of α and Ad in the 450 – 650 nm region obtained by minimizing the difference between measured water-leaving reflectance values and those simulated using Eq. 1, with α, Ad and R_∞ as free fitting parameters and z measured in-situ. For convenience, the values for R_∞ are incorporated in **Figure *3-15***c, though this parameter is excluded from our analysis. The iterative fitting procedure terminates when the difference between measured and simulated water leaving reflectance, ΔR, is smaller than a threshold value ΔR_T. The sensitivity of the fitting procedure to the choice of ΔR_T is shown Figure 4, where bars represent the range of the fitted coefficients when ΔR_T is set to 0.01, 0.025, 0.05 and 0.1. The spectrally averaged values for α for the Landsat bands 1 and 2 and the spectrally similar MODIS bands 3 and 4 are, respectively: $\alpha_{B1\_LANDSAT}$=1.91, $\alpha_{B2\_LANDSAT}$=2.33, α_{B3_MODIS}=1.73 and α_{B4_MODIS}=2.4. For the lake under study, the optimal (fitted) values for α differ by ~ + 15 % (-15 %) from the constant value of α = 2. An error of 15 % on α translates into a lake depth retrieval error of ~ 17 % when using the Landsat band 2. **Figure *3-15*** also suggests that α increases with wavelength, which cannot be easily explained, aside from a possible chlorophyll concentration in the water, currently considered to be unlikely. A possible explanation is a higher variability of lake-bottom albedo in the blue region, producing a higher degree of uncertainty in our approximated α in that range.

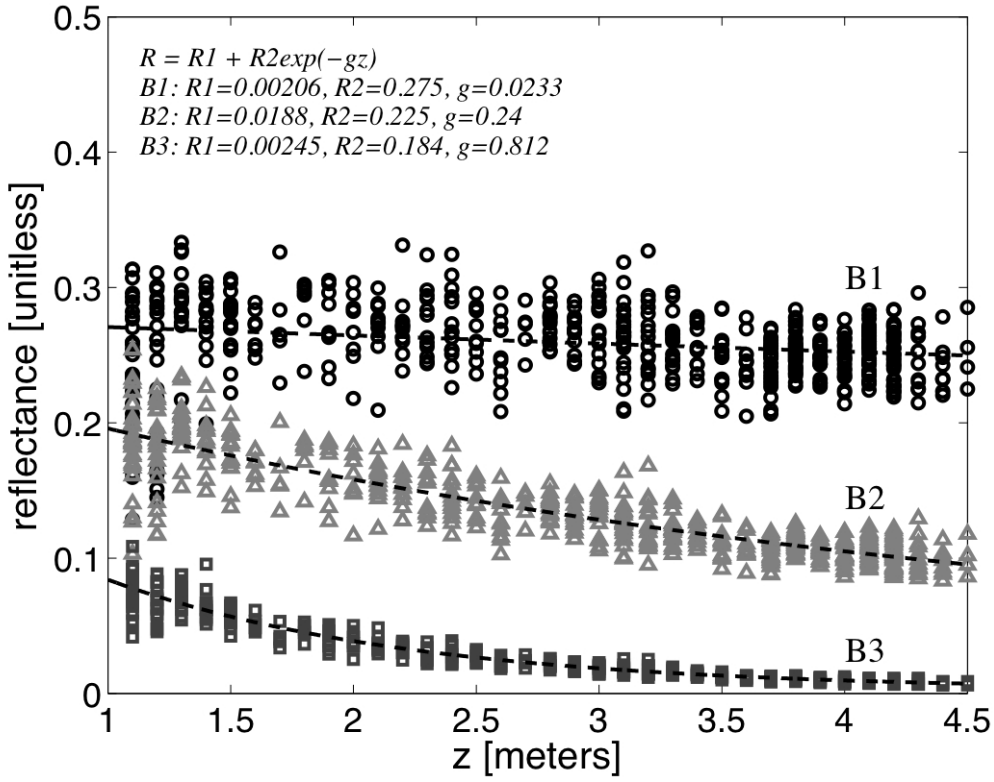

Figure 3-9 In-situ measured water-leaving reflectance values vs. lake depth for the Landsat bands 1, 2 and 3 and exponential fitting

The fitted values of *Ad* are greater at shorter wavelength and decrease with increasing wavelength, displaying a spectral behavior similar to that of glacier ice albedo (*e.g., Grenfell and Perovich, 2004)*. To evaluate the assumption of estimating the value of *Ad* from the reflectance of shallow waters, we use data collected by Landsat over Lake Olivia on July 9th, 2010 (http://glovis.usgs.gov), converted into planetary reflectance following *Chander et al. (2009)*.

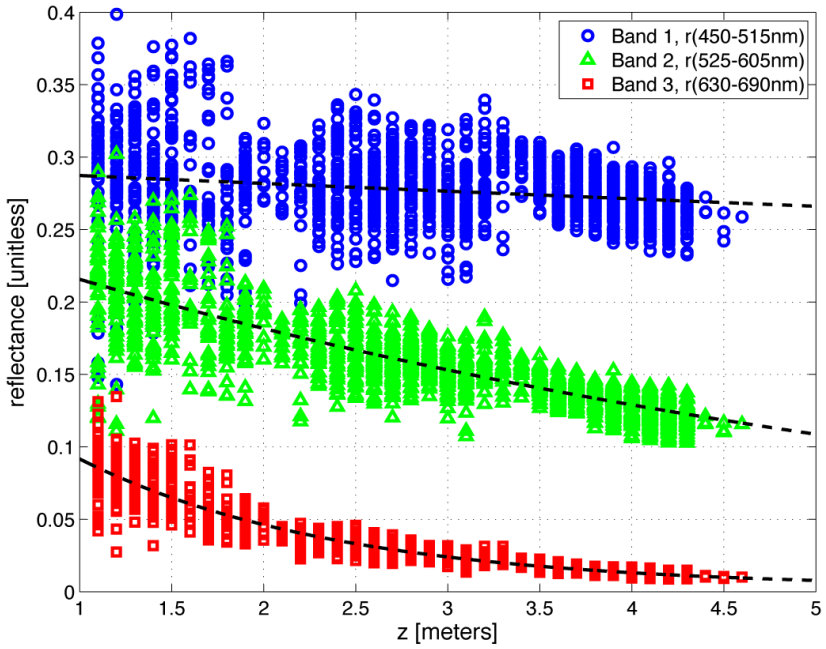

Figure 3-10 Similar to I, using data from July 3rd.

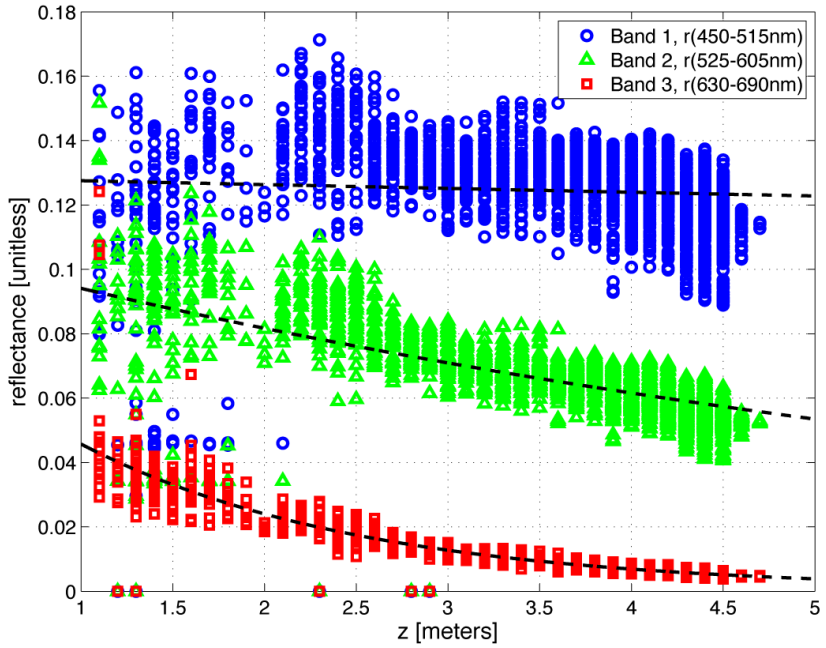

Figure 3-11 Similar to I, using data from July 5th.

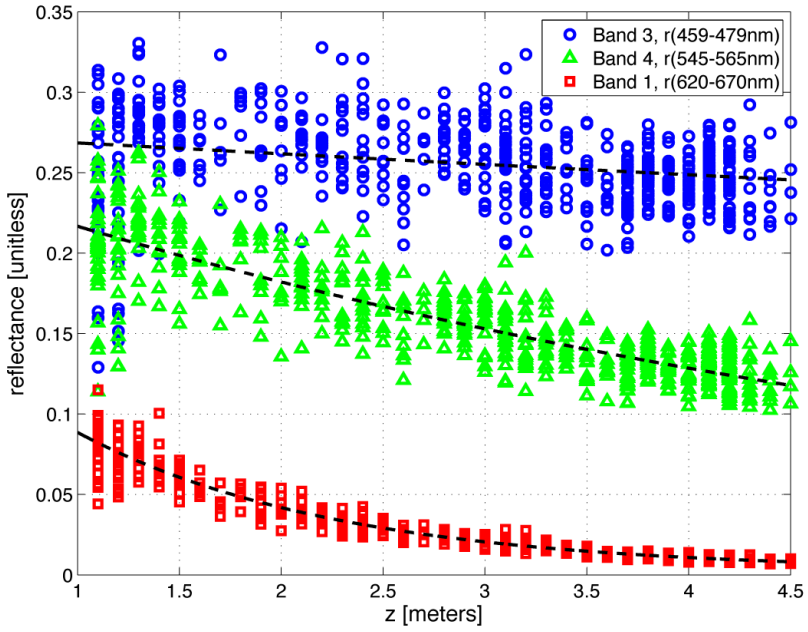

Figure 3-12 Similar to Figure 9, using data from July 2nd and wavelengths corresponding to MODIS bands 1, 3 and 4.

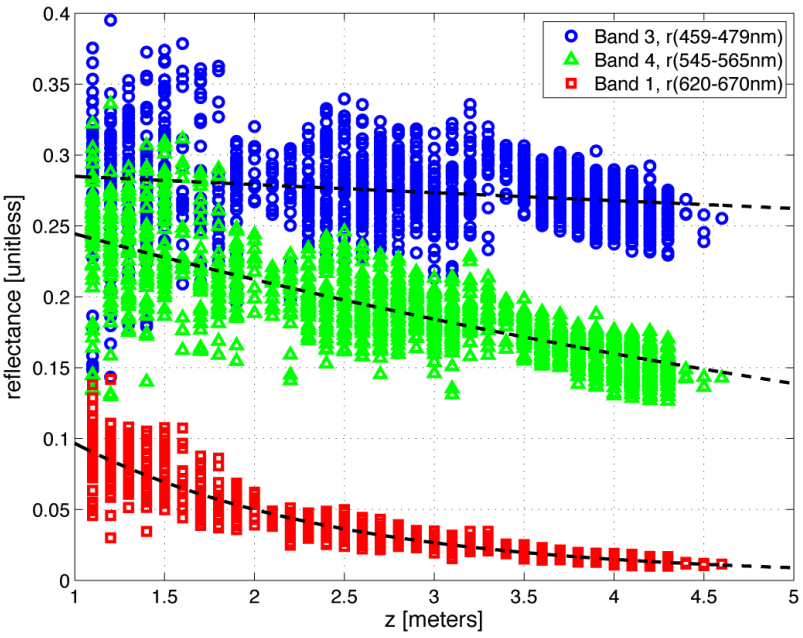

Figure 3-13 Similar to Figure 9, using data from July 3rd and wavelengths corresponding to MODIS bands 1, 3 and 4.

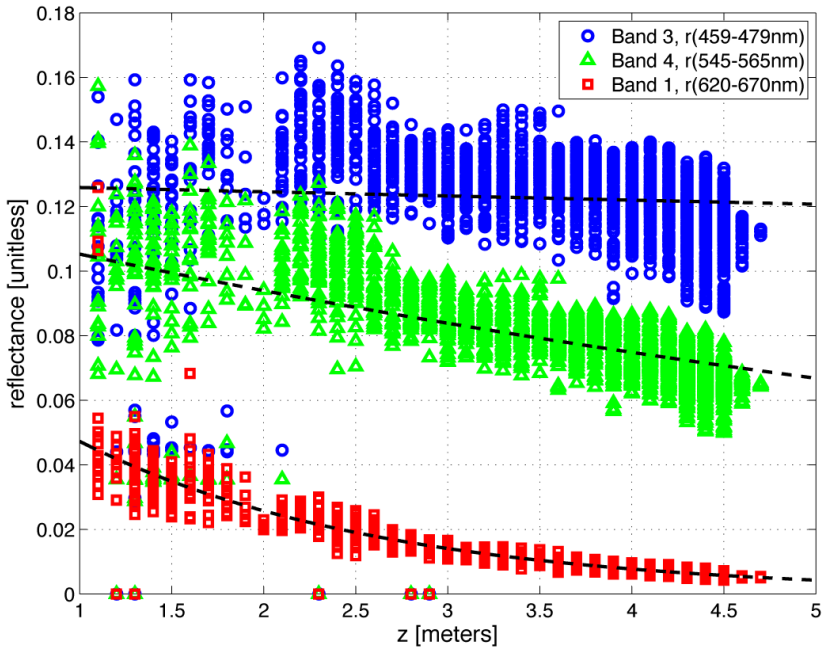

Figure 3-14 Similar to Figure 9, using data from July 5th and wavelengths corresponding to MODIS bands 1, 3 and 4.

Though Landsat and in-situ data were not collected on the same day, we assume that the lake depth did not change considerably between July 6th and July 9th. This is supported by the small depth change (< 0.2 m) recorded by a pressure transducer positioned into the lake during the period July 1st – July 6th and by the simple visual analysis of daily WorldView-2 radiances collected between July 4th and July 9th. Reflectance values at the top of the atmosphere (TOA) were corrected for atmospheric effects using the Fast Line-of-sight Atmospheric Analysis of Spectral Hypercubes (FLAASH) atmospheric correction (*Alder-Golden et.al. 1999*) implemented in the software ENVI®. In absence of atmospheric data, to simulate mid-summer conditions over the section of Greenland under study, the FLAASH model was initialized using a mid-latitude winter atmospheric model and maritime aerosol model. Aerosol optical depth was calculated

using a 2-band VIS and SWIR ratio method using band 3 and 7 respectively (*Kaufman et al., 1997*). The average difference between atmospherically corrected and TOA reflectance values over the lake was -3.9% (± 0.98 %) in the case of band 1 and -2.4% (± 2.1 %) for band 2. The choice of the atmospheric model applied to the TOA reflectance values can be a source of uncertainty on the lake depth estimates. This uncertainty cannot be estimated in absence of information on the vertical profile of the atmospheric parameters used in the model. However, we decided to use the atmospherically corrected reflectance values for our analysis for consistency with the MODIS data used in this study.

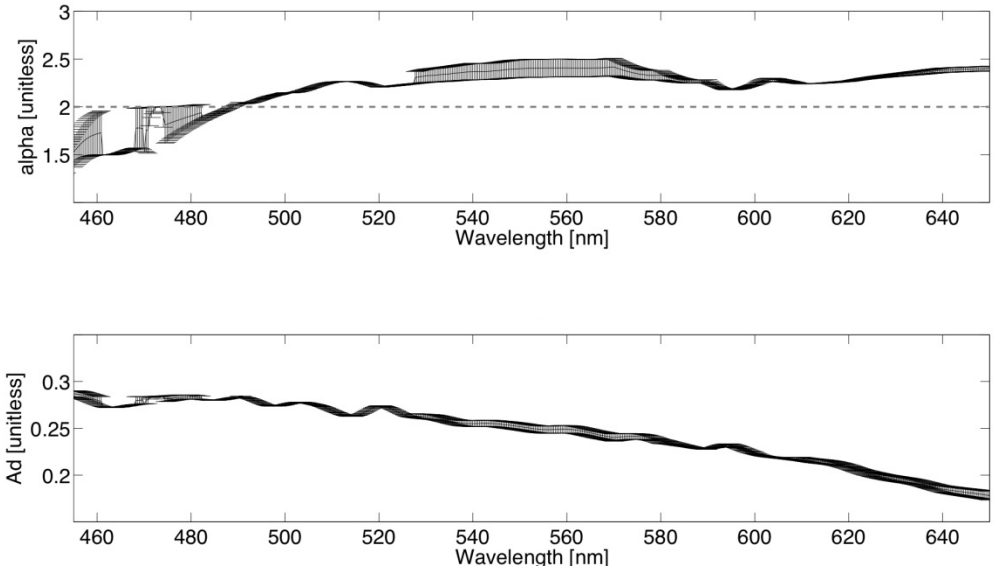

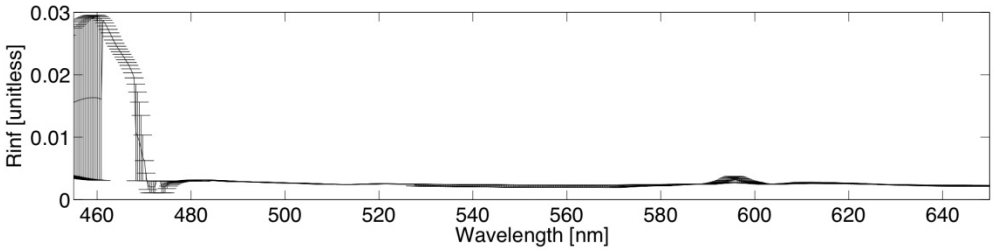

(c)

Figure 3-15 Spectral dependency of α (top) and Ad (bottom) values derived from the minimization of the difference ΔR between measured and theoretical water-leaving reflectance values. Bars represent the range of values when different ΔR values are used (see text for details).

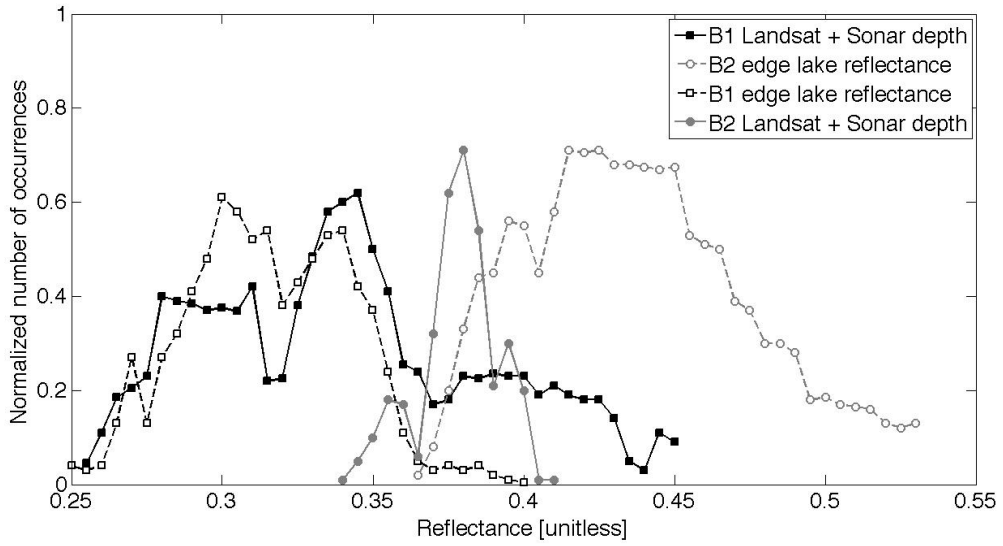

Figure 3-16 Distribution of Ad values for the Landsat bands 1 and 2 estimated from Eq. 2 using lake depth measured by the boat (cont. lines) and of reflectance values from the edge lake (dashed lines).

Figure *3-16* illustrates the distribution of *Ad* for the Landsat band 1 (black lines) and band 2 (gray lines) obtained resolving Eq.2 for *Ad,* with *z* obtained from in-situ measurements and R_∞

from the Landsat image where deep water ($z > 40\ m$) is present (e.g., *Sneed and Hamilton, 2007)*. The distributions of the reflectance values at the two bands estimated from pixels along the lake edge are also plotted. The mean *Ad* values obtained from solving Eq. 2 are $Ad_{LANDSAT\_B1}$ = 0.37±0.012 and $Ad_{LANDSAT\_B2}$ = 0.3±0.024; the mean reflectance values for pixels along the lake edge are R_{Edge_B1} = 0.42±0.058 for band 1 and R_{Edge_B2} = 0.34± 0.062 for band 2. The range of values obtained using these parameters are indicated in **Figure *3-17***.The percentage error between the mean *Ad* value and the mean of the reflectance values along the lake edge is ~ 10 % in both cases of the blue and green Landsat bands. From Eq. 2, this translates into an average error on lake depth retrieval between ~ -10 % and ~ -15 % when using, respectively, the Landsat bands 1 or 2. The error on depth is at a `maximum for shallow waters with an underestimation down to ~ -25 % (blue) and ~ -40 % (green) and reduces to ~ -5 % for both channels for lake depth values up to 10 m.

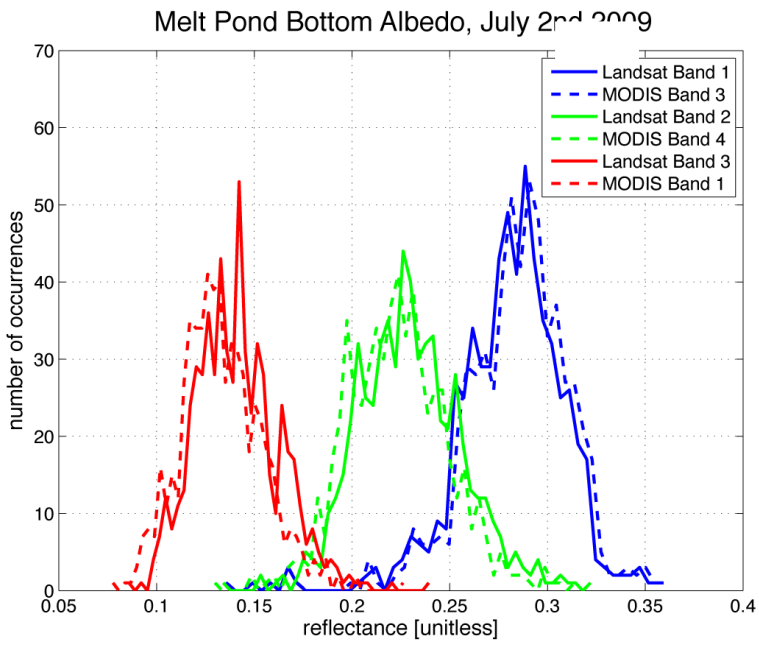

Figure 3-17 Bottom albedo estimates calculated using Eq(2) and in-situ reflectance measuremetns collected on July 2nd 2010.

3.6 Assessment of lake depth from satellite data

Here we compare the lake depth values estimated with Landsat and MODIS with those measured in-situ. Table 1 reports the mean, standard deviation and maximum values of lake depth obtained from satellite data, together with the root mean square error, the mean absolute error, correlation and percentage error between spaceborne-estimated lake depth using either Landsat and 500 m MODIS reflectance product (http://modis.gsfc.nasa.gov/data/dataprod/dataproducts.php?MOD_NUMBER=09) and the values measured by the sonar. Results obtained from MODIS are averaged over the period July 2nd - July 5th, 2010, when in situ data were collected. We decided to use the abovementioned MODIS product (rather than correcting level 1 MODIS data for atmopshere and extract reflectance values) because of the potential large use of such product in estimating spatio-

temporal variability of supraglacial lakes at a relatively low computational cost. However, we point out that the MODIS reflectance product (MOD09) makes use of multiple daily observations. Within each tile, areas with clouds or low elevation sun angles are not used and other criteria are applied to select those observations used to generate the product (http://modis-sr.ltdri.org/products/MOD09_UserGuide_v1_2.pdf). Consequently data acquired at different times can be potentially used for generating the final product. We also point out that the MODIS nominal spatial resolution of 250 m is only valid for those cases when the observation angle is close to the nadir. When the target is on the side of the swath, the instantaneous field of view (IFOV) becomes larger and, hence, a larger surface is responsible for the reflectance value. If this surface contains the lake edge, the overall reflectance might be higher than the one obtained when the observation angle was close to nadir, because of the presence of ice or snow. Lastly, another factor affecting the remote sensing algorithm is the presence of ice on the lake surface, which has been observed from the analysis of high resolution visible images and during our fieldwork. The resultant dataset of MODIS Terra and Aqua measurements at 500 m resolution is plotted in **Figure *3-18***. To indicate the ability of MODIS to detect melt ponds, we present the ratio of red to infrared channels taken over Lake Olivia. This is often used to indicate the presence of pooled water on the ice surface, is shown at a spatial resolution of 250 meters (**Figure *3-19***).

Results obtained in the case of MODIS when using either $\alpha=2$ or the values of α obtained from the fitting procedure above described (Figure 4b) are reported. The values of the bottom albedo *Ad* are obtained from the mean of the reflectance of shallow waters on the edge of the lake (*e.g., Sneed and Hamilton, 2007)*. As a reference, the mean, standard deviation and maximum depth of the lake depth values measured by the sonar are also shown in the first row of the table. Results

indicate that the use of the Landsat band 1 tends to overestimate lake depth, with an RMSE ranging between 2.7 and 3 m, a maximum lake depth on the order of 8 m (against the value of 4.55 m measured in situ) and a mean value of ~ 6 m. Lake depth is also overestimated when using the MODIS band 3, that is spectrally similar to the Landsat band 1. Maximum depth values from MODIS are close to those estimated by Landsat band 1 but the mean values from MODIS are higher than those obtained with Landsat. Results improve when using either the Landsat band 2 or MODIS band 4, with mean depth values ranging between 0.71 m (AQUA) and 3.64 m (Landsat). Best results are obtained with Landsat when using $\alpha=2.33$ (from fitting). In this case, mean, standard deviation and maximum depth provide the closest estimates to the measured ones, with a RMSE of 0.59 m. MODIS band 4 tends to underestimate lake depth with respect to in-situ data. In the case of MODIS, the use of the α fitted value deteriorates the performance of the remote sensing algorithm, further reducing the values of the estimated lake depths.

Table 3-1 Statistics on lake depth retrieval using different space-borne sensors, bands and hypot heses on the value of the α coefficient

	Mean [m]	Std. dev. [m]	Max. [m]	RMSE [m]	Correlation
SONAR	2.83	0.97	4.55	n/a	n/a
Landsat BAND 1 (450 – 515 nm)					
$\alpha=2$	5.95	1.47	8.21	2.76	0.78
$\alpha=1.91$	5.98	1.52	8.35	3.02	0.77
Landsat BAND 2 (525 – 605 nm)					
$\alpha=2$	3.64	0.91	4.87	0.67	0.85
$\alpha=2.33$	2.92	0.78	4.21	0.59	0.87

MODIS TERRA (AQUA) - BAND 3 (459 – 479 nm)					
$\alpha = 2$	6.5 (2.3)	1.93 (1.47)	8.65 (4.14)	n/a	n/a
$\alpha = 1.91$	6.93 (2.44)	2.04 (1.56)	9.18 (4.39)	n/a	n/a
MODIS TERRA (AQUA) - BAND 4 (545 – 565 nm)					
$\alpha = 2$	2.1 (0.9)	0.92 (0.9)	2.9 (1.9)	n/a	n/a
$\alpha = 2.33$	1.71 (0.71)	0.75 (0.74)	2.44 (1.56)	n/a	n/a

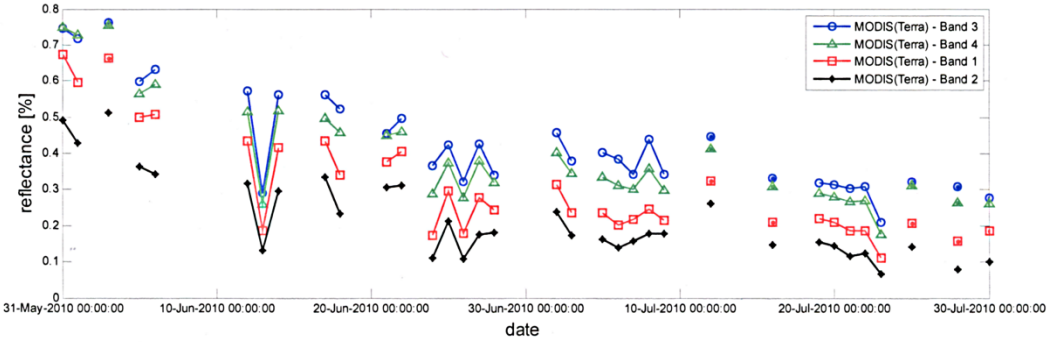

Figure 3-18 MODIS Terra reflectance measurements of Lake Olivia during the melting season of 2010 using MODIS Bands 1 through 4.

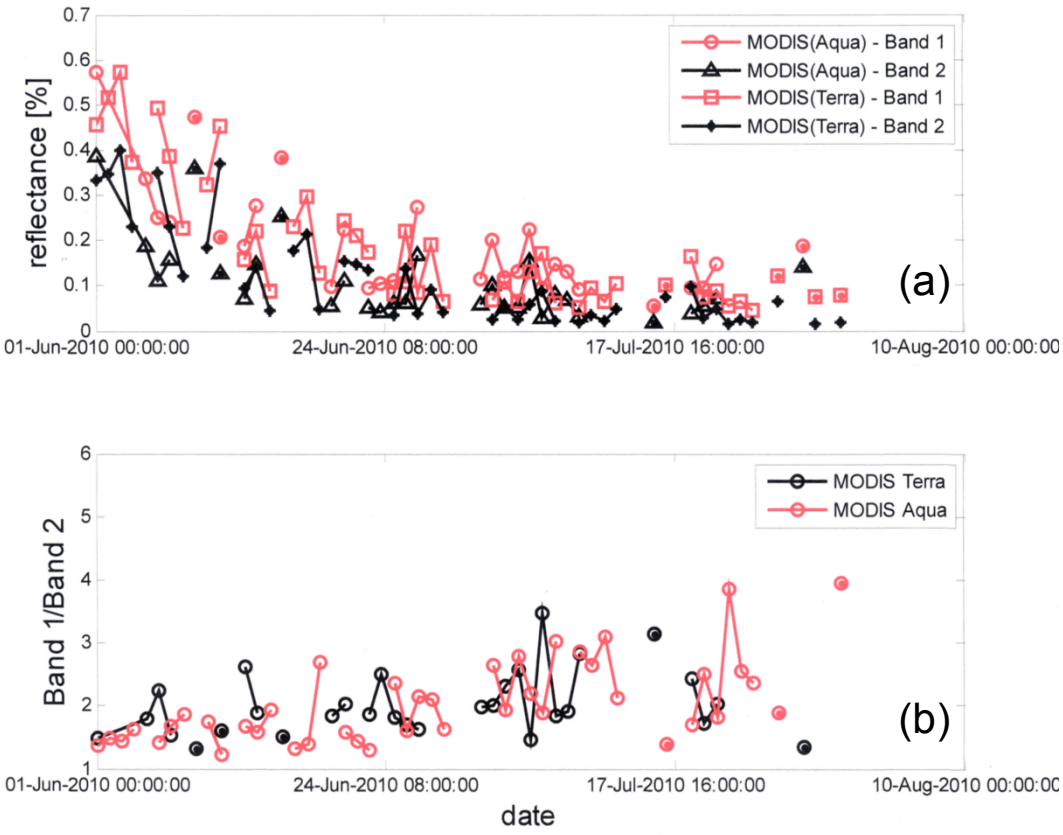

Figure 3-19 (a) Reflectance measurements during the melting season of 2010 of Lake Olivia at 500 meters from MODIS Terra and Aqua. (b) The red to infrared ratio of data values reported in (a).

In Table 2 we report the results of our analysis aimed at quantifying the error on lake depth retrieval from the assumptions of a uniform *Ad* value for the whole lake and using the reflectance values of the pixels at the edge of the lake for *Ad*. Lake depth values are estimated using Eq. 2, with *Ad* values given by the mean of the distributions of the bottom albedo values obtained form the concurrent analysis of surface and satellite data or by the mean of the reflectance values along the lake edge. The table includes the mean, standard deviation, maximum value of lake

depth obtained from the satellite data together with the root mean square error, the mean absolute error, correlation and percentage error between the lake depth values estimated with the different configurations and the values measured by the sonar. Results from both Landsat (bands 1 and 2) and MODIS (bands 3 and 4) are reported. In general, best results are obtained when using the Landsat band 2 when *Ad* is given by the mean of the *Ad* distribution computed from the conjunct analysis of satellite and surface data. Depth estimates using Landsat band 1 show a larger standard deviation and higher maximum depth values (above the maximum measured depth), likely as a consequence of the smaller diffuse attenuation coefficient in the blue band (*Smith and Baker, 1980, Pope and Fry, 1997)*. Maximum lake depth values estimated when using Landsat band 2 are closer to the value measured in situ. The MODIS sensor on TERRA provides smaller lake depth values than those obtained with the one mounted on AQUA. Given the short time-series it is not possible to assess whether this is a consistent bias. The values estimated by MODIS on TERRA are the closest to those estimated by Landsat and measured in situ. Lake depth values estimated from MODIS when using band 4 are generally smaller than those measured in situ.

3.7 Conclusions and future work

We collected in-situ concurrent multi-spectral and depth observations over a supraglacial lake in West Greenland in order to assess spaceborne bathymetry. Such measurements allowed us to study the spectral dependency of the bottom albedo *Ad* and coefficient α, with the latter linearly relating the attenuation coefficient *g* and the diffuse attenuation factor *Kd.* Results show that, as expected, the spectral behavior of *Ad* is similar to that of glacier ice albedo. The increase of α with wavelength from in-situ data cannot be easily explained without assuming chlorophyll, or

other absorbing materials, in the water, which is present at a very minimal concentration according to our preliminary analysis of water samples. One explanation for the spectral behavior of α is that the bottom albedo has a higher variability in the blue region, attributing some of the loss due to a darker blue ice to loss along the water column.

We assessed a widely used literature technique in which *Ad* is assumed to be uniform and equal to the reflectance of shallow waters along the lake edge. The analysis of in-situ measurements show a Gaussian-like behavior of *Ad,* with this variability appearing to be intrinsic to the albedo of the bottom, consisting of large patches of cryoconite, fine particles of highly absorbing atmospherically transported aerosols. The difference between the mean *Ad* value obtained from in-situ measurements and the mean of the reflectance values along the lake edge obtained from Landsat is on the order of ~ 10 %. This translates into an average error on lake depth retrieval of -11.8 % (-15.9 %) when using the Landsat band 1 (band 2). The error is maximum for shallow waters with an underestimation down to -23.7 % (-42.7 %) and reduces to -4.6 % (-4.7 %) for lake depth values up to 10 m. This should be accounted for when assuming a Ad value for depth retrieval (*hyp* 1 and 2, pg, in Background and rationale).

In the case of α, the values obtained from in-situ measurements differ by ~ 15 % from those computed using literature approaches. Best spaceborne-based estimates were obtained when using either the Landsat band 2 or the spectrally similar MODIS band 4. In the case of Landsat, best results are obtained when using the α value derived from in-situ measurements ($\alpha = 2.33$). However, this is not true in the case of MODIS, where best results are obtained using the values suggested in the literature ($\alpha = 2$). In the case of MODIS, however, mixed-pixel effects and relatively coarse resolution can be responsible for large uncertainty. For example, the presence of

ice within a pixel will increase the reflectance with respect to a pixel containing only liquid water, leading to an underestimation of the lake depth. This is especially true for relatively small lakes and for those pixels containing the lake edges. In the future, we plan to collect a more comprehensive in-situ data set on the inherent optical properties of melt pond water and to extend our analysis to multiple lakes. We also plan to use a more sophisticated model of the water column (*Lee, 1999*), in which depth estimations can be made with a fully physical model of water constituents.

3.8 References

Adler-Golden, S. M., M. W. Matthew, L. S. Bernstein, R. Y. Levine, A. Berk, S. C. Richtsmeier, P. K. Acharya, G. P. Anderson, G. Felde, J. Gardner, M. Hoke, L. S. Jeong, B. Pukall, A. Ratkowski, and H.-H Burke. Atmospheric Correction for Short-wave Spectral Imagery Based on MODTRAN4. SPIE Proceedings on Imaging Spectrometry, Vol. 3753, pp. 61-69, 1999

Box, J. E. and K. Ski: Remote sounding of Greenland supra-glacial melt lakes: implications to sub-glacial hydraulics, *J. Glaciol.,* 181, 257 – 265*,* 2007.

Chander, G., B. L. Markham and D. L. Helder: Summary of current radiometric calibration coefficients for Landsat MSS, TM, ETM+, and EO-1 ALI sensors, *Remote Sensing of Environment* 113, 893–903, 2009.

Das, S. B., I. Joughin, M.D. Behn, I.M. Howat, M.A. King, D. Lizarralde and M.P. Bhatia: Fracture propagation to the base of the Greenland ice sheet during supraglacial lake drainage, *Science*, 320, 778-781, 2008.

Georgiu, S., A. Shepherd, M. McMillan and P. Nienow: Seasonal evolution of supraglacial lake volume from ASTER imagery, *Annals of Glaciology,* 50(52), 95 – 100, 2009.

Grenfell, T. C., and D. K. Perovich: Seasonal and spatial evolution of albedo in a snow-ice-land-ocean environment, *J. Geophys. Res.*, *109*, C01001, doi:10.1029/2003JC001866, 2004.

Joughin, I., S. Tulaczyk, M. Fahnestock and R. Kwok: A mini-surge on the Ryder Glacier, Greenland, observed by satellite radar interferometry, *Science*, 274, 228–230, 1996

Kaufmann, Y. J., A. E. Wald, L. A. Remer, B.-C. Gao, R.-R. Li, and L. Flynn,. The MODIS 2.1-mm Channel-Correlation with Visible Reflectance for Use in Remote Sensing of Aerosol. IEEE Transactions on Geoscience and Remote Sensing. Vol. 35, pp. 1286-1298, 1997.

Lee, Z., et al.: Hyperspectral remote sensing for shallow waters. 2. Deriving bottom depths and water properties by optimization, *Applied Optics*, *38*(18), 3831-3843, 1999.

Lüthje, M., L.T. Pedersen, N. Reeh, and W. Greuell: Modelling the evolution of supra-glacial lakes on the West Greenland ice-sheet margin, *Journal of Glaciology*, 52, 608-618, 2006.

Maritorena, S., A. Morel, and B. Gentili: Diffuse reflectance of oceanic shallow waters: Influence of water depth and bottom albedo, *Limnol. Oceanogr*., 39(7), 1689– 1703, 1994

McMillan, M., P. Nienow, A. Shepherd, T. Benham, and A. Sole: Seasonal evolution of supra-glacial lakes on the Greenland ice sheet. *Earth and Planetary Science Letters*, 262, 484-492, 2007.

Mobley, C.D.: Estimation of the remote-sensing reflectance from above-surface measurements, *Appl. Optics,* 38(36), 7442-7455, 1997.

Mueller, J.: In-Water Radiometric Profile Measurements and Data Analysis Protocols, *NASA/TM-2003-21621/Rev-Vol III, 7,* 2003.

Mueller, J., G. McClain, R. Bidigare, C. Trees, W. Balch, J. Dore, D. Drapeau, D. Karl, and L. Van: Ocean optics protocols for satellite ocean color sensor validation, revision 5, volume V: Biogeochemical and bio-optical measurements and data analysis protocols, NASA Tech. Memo. 2003-211621, Rev, 5, 2003.

Philpot, W. D., Bathymetric mapping with passive multispectral imagery, *Appl. Optics*, 28(8), 1569– 1578, 1989.

Pimentel, S. and G. E. Flowers: A numerical study of hydrologically driven glacier dynamics and subglacial flooding, *Proc. R. Soc. A* doi: 10.1098/rspa.2010.0211, 2010.

Pope, R.M.and E. S. Fry, Absorption spectrum (380–700 nm) of pure water. II. Integrating cavity measurements, *Appl. Opt.*, 36, 8710-8723, 1997.

Smith, R. C. and K. S. Baker: Optical properties of the clearest natural waters (200-800 nm), *Appl. Optics*, Vol. 20, No. 2, 1981.

Sneed, W. A., and G. S. Hamilton: Evolution of melt pond volume on the surface of the Greenland Ice Sheet, *Geophys. Res. Lett.*, *34*, L03501, doi:10.1029/2006GL028697, 2007.

Sundal, A.V., A. Shepherd , P. Nienow , E. Hanna, S. Palmer , P. Huybrechts: Evolution of supra-glacial lakes across the Greenland Ice Sheet, *Remote Sensing of Environment* 113, 2164–2171, 2009.

Tedesco, M., X. Fettweis, M. R. van den Broeke, R. S. W. van de Wal, C. J. P. P. Smeets, W. J. van de Berg, M. C. Serreze and J. E. Box, The role of albedo and accumulation in the 2010 melting record in Greenland , *Environ. Res. Lett.* 6 014005

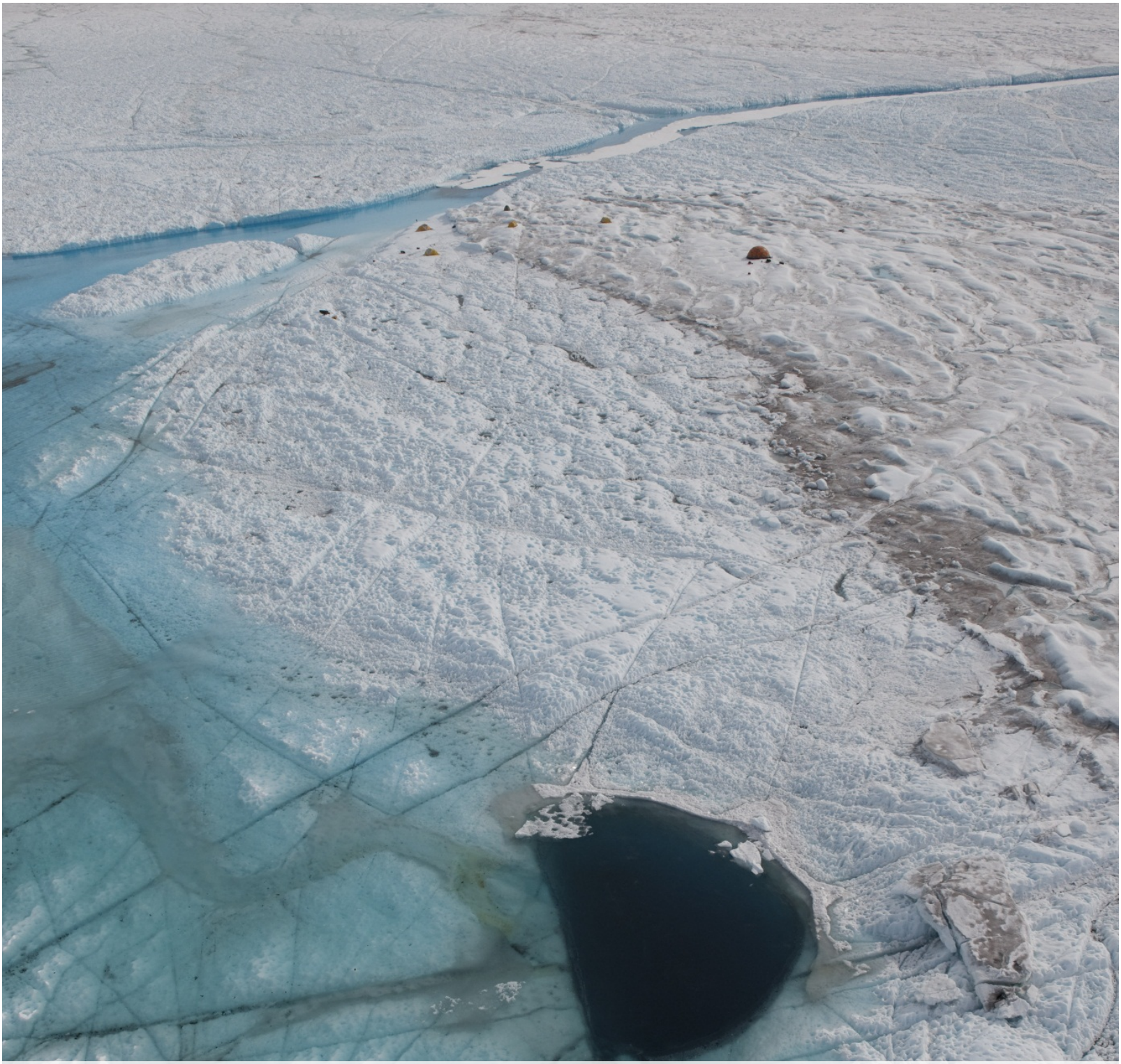

Measurement and modeling of ablation of the bottom of supraglacial lakes in Western Greenland

Published as:

Tedesco, M., Luthje, M., Steffen, K., Steiner, N., Fettweis, X., Willis, I., . . . Banwell, A. (2012). Measurement and modeling of ablation of the bottom of supraglacial lakes in western Greenland. *Geophysical Research Letters, 39*. doi: L0250210.1029/2011gl049882

4 Measurement and modeling of ablation of the bottom of supraglacial lakes in Western Greenland

M. Tedesco
City College of New York, City University of New York, New York, USA

M. Lüthje
GeoScandia, Birkerød, Denmark

K. Steffen
Cooperative Institute for Research in Environmental Sciences, University of Colorado at Boulder, Boulder, Colorado, USA

N. Steiner
City College of New York, City University of New York, New York, USA

X. Fettweis
Department of Geography, University of Liege, Liege, Belgium

I. Willis
Scott Polar Research Institute, Department of Geography, University of Cambridge, Cambridge, UK

N. Bayou
Cooperative Institute for Research in Environmental Sciences, University of Colorado at Boulder, Boulder, Colorado, USA

A. Banwell
Scott Polar Research Institute, Department of Geography, University of Cambridge, Cambridge, UK

4.1 Abstract.

We report measurements of ablation rates of the bottom of two supraglacial lakes and of temperatures at different depths collected during the summers of 2010 and 2011 in west Greenland. To our knowledge, this is the first time that such data sets are reported and discussed in the literature. The measured ablation rates at the bottom of the two lakes are of the order of ~ 6 cm/day, versus a rate of ~ 2.5 – 3 cm/day in the case of bare ice of surrounding areas. Though our measurements suggest the presence of a vertical temperature gradient, it is not possible to

draw final conclusions as the measured gradient is smaller than the accuracy of our temperature sensors. In-situ measurements are compared with the results of a thermodynamic model forced with the outputs of a regional climate model. In general, the model is able to satisfactorily reproduce the measured quantities with RMSE of the order of 3 – 4 cm for the ablation and ~ 1.5 ºC in the case of water temperature. Our results confirm that the ablation at the bottom of supraglacial lakes plays an important role on the overall lake volume with the ablation in the case of ice covered by a lake being 110 – 135 % of that over bare ice at nearby locations. Beside ice sheet hydrological implications, melting at the bottom of a supraglacial lake might affect estimates of lake volume from spaceborne visible and near-infrared measurements.

4.2 Introduction and background.

Supraglacial lakes form annually in topographic depressions of the surface of the Greenland ice sheet (GrIS, e.g., *Selmes et al., 2011*), affecting ice loss through increased surface ablation and, during drainage, affecting basal water pressures and ice velocities (e.g, *Lüthje et al., 2006; Das et al., 2008; Pimentel and Flowers, 2010; Sundal et al., 2011*). Over the past years, several studies have estimated the area and volume of supraglacial lakes from spaceborne observations (e.g., *Sneed and Hamilton, 2007; Box and Ski, 2007; McMillan et al, 2007)* and some have been able to validate these estimates from ground based measurements (*Tedesco and Steiner, 2011; Sneed and Hamilton, 2011*).

Very little is known about the contribution of the melting of the bottom of supraglacial lakes to their total volume, with this aspect being generally neglected in studies dealing with volume estimates. This is possibly due to the absence of *in-situ* observations, which can be used to understand the physical processes involved or to validate theoretical models. To fill this gap,

here we report measurements of ablation rates of the bottom of two supraglacial lakes collected during the summers of 2010 and 2011 in West Greenland. Temperature values were also collected at different depths within the lakes to study the vertical distribution of water temperature (being this an important factor for understanding, modeling and quantifying convection rate at lake bottom). To our knowledge, this is the first time that such data sets are reported and discussed in the literature. *In-situ* measurements are compared with the outputs of a fully physically-based thermodynamic model which, in turn, is forced with the outputs from a regional atmospheric model, coupled with a snow model.

In-situ measurements confirm the crucial role played by supraglacial lakes in enhancing ice ablation and suggest the presence of a vertical temperature gradient within the lake. Model's outputs compare favorably with measurements. In the following we discuss the methods used to collect the data, the measured quantities and the comparison between modeled and measured values of both ablation rates and lake water temperature.

4.3 *In-situ* measurements.

The ablation rate of the bottom of a supraglacial lake (*ABLR* hereafter) is obtained from the data recorded by two pressure transducers, with the first (top) sensor being firmly secured at a fixed height to an aluminum pole drilled in the ice where a supraglacial lake is assumed to form. The second (bottom) sensor is loosely attached to the same pole and resting on the ice surface so that it can slide downwards following the ice bottom along the pole as the bottom of the lake melts, while still remaining close to the pole (*Figure 4-1)*. The ABLR is then calculated from the difference between the time series of the depths recorded by the two sensors. The depth measured by the top sensor is indeed the height of the water column above the sensor where the

depth measured by the bottom sensor is the depth measured by the top sensor plus the original height difference between the two sensors plus the thickness of the ice lost from the bottom of the lake, where the sensor is sitting. The ablation rate can therefore be obtained from the difference in the slopes of the curves describing the filling rates measured by the two sensors. One assumption underlying this technique is that the aluminum pole does not considerably sink into the ice. The analysis of our data shows that this is a reasonable assumption, as the vertical displacements of the poles that are within the ice for relatively short periods (~ 5 – 10 days) were found to be considerably smaller than the measured ablation rates.

Figure 4-1 Configuration of the top and bottom pressure transducers deployed at lake Ponting on June 13th, 2011. The aluminum pole was drilled into the ice down to 3m. The difference between the heights of the two sensors is 0.7 m.

In-situ data were collected during the summers of 2010 and 2011 at two different locations in west Greenland. The first pair of sensors was deployed on May 17th, 2010 nearby (~ 200 m) the Swiss Camp station of the Greenland Climate Network (69.569 N, -49.342 E, 1149 m a.s.l., GC-Net, *Steffen et al., 1996*) where satellite images and in-situ surveys indicated a lake would form annually (Lake Bluesnow hereafter). The top sensor was initially located 2m above the bottom one. The lake filled on June 10th and both sensors were underwater from June 23rd. The lake drained on June 28th. The second pair of sensors was deployed ~ 10 km north of the JAR-1 GC-Net station on June 13th, 2011 (69. 589 N, -49.783 E, 962 m a.s.l., Lake Ponting hereafter). In this case, the top sensor was initially positioned 0.7 m above the bottom one. The two sensors were underwater from June 14th and the lake drained on June 19th.

All sensors recorded pressure and temperature every five minutes on an internal data logger and were recovered following lake drainage. The sensors have a water level (temperature) accuracy of 0.5 cm (0.35 ºC) and a resolution of 0.21 cm (0.1 ºC). For each lake, pressure data were corrected for altitude and for barometric pressure changes using data collected by a third pressure sensor located in close proximity (within 1 km) of the lake.

4.4 Modeling tool.

We model the ABLR and water temperature using a one-dimensional enthalpy approach model (*Alexiades and Solomon, 1993*). In the following we give a brief description of the model and refer the reader to *Lüthje et al., 2006* for more details. The volume of ice down to a depth Z is divided into N control volumes, with the volumes being initialized with an enthalpy corresponding to a temperature profile with a depth gradient of 2 $K \cdot m^{-1}$, based on measurements

from Pâkitsoq, West Greenland (*Lüthje et al., 2006)*. The model accounts for conductive heat transport through ice following *Alexiades and Solomon, 1993*. Turbulent heat transfer through lake water is also accounted for. The heat flux between the turbulent lake and the ice bottom is computed using the '*four thirds'* law *(Linden, 2000)*. The model is forced with the net energy flux at the interface between surface and atmosphere. Specific inputs are surface air temperature, shortwave incoming radiation, albedo, atmospheric pressure, incoming and outgoing longwave radiation, latent heat and sensible heat fluxes. These are obtained from the *Modèle Atmosphérique Régional* (MAR) model, a regional atmospheric model coupled with a snow model (*e.g. Fettweis et al. 2011; Tedesco et al. 2011*). The ERA-INTERIM reanalysis (2002-May 2011) and the operational analysis (June 2011 – to date) data from the European Centre for Medium-Range Weather Forecasts (ECMWF, http://www.ecmwf.int/) are used to initialize the meteorological fields and to force the lateral boundaries every 6 hours. Note that ECMWF fields are used only at the boundaries of the region containing the GrIS (see *Fettweis, 2007* for details) and that the inputs to the ablation model are obtained from the atmospheric model within MAR. MAR outputs are produced at a horizontal spatial resolution of 25 km and their accuracies have been assessed over the GrIS *(e.g., Fettweis et al., 2011)*. To further investigate the potential use of MAR outputs to satisfactorily drive the ablation model, we compared MAR outputs with *in-situ* measurements available from the GC-Net stations. Figure 1 illustrates the comparison between GC-Net measured (circles) and MAR simulated (lines) surface temperature, shortwave incoming radiation, albedo and atmospheric pressure at the Swiss Camp (Lake Bluesnow, left plots) and JAR-1 (Lake Ponting, right plots) stations. The plots indicate that the MAR model is favorably reproducing the trends of the GC-Net measured quantities, though, as expected, differences exist. The root mean square error (RMSE) between the measured and simulated

quantities is 0.85°C (0.38°C) for temperature, 9.7 W/m^2 (8.3 W/m^2) for the shortwave incoming radiation, 0.14 (0.11) for the albedo and 5.7 hPa (24.3 hPa) for pressure for the Swiss Camp (JAR-1) station. Differences between simulated and measured quantities can be, among other things, due the coarse spatial resolution of the MAR outputs with respect to the plot-scale nature of the *in-situ* measurements. Also, the elevation changes within the 25 km MAR grid are +50 m for Swiss Camp and -164 m for JAR-1 and this could explain the bias between the modeled and measured quantities.

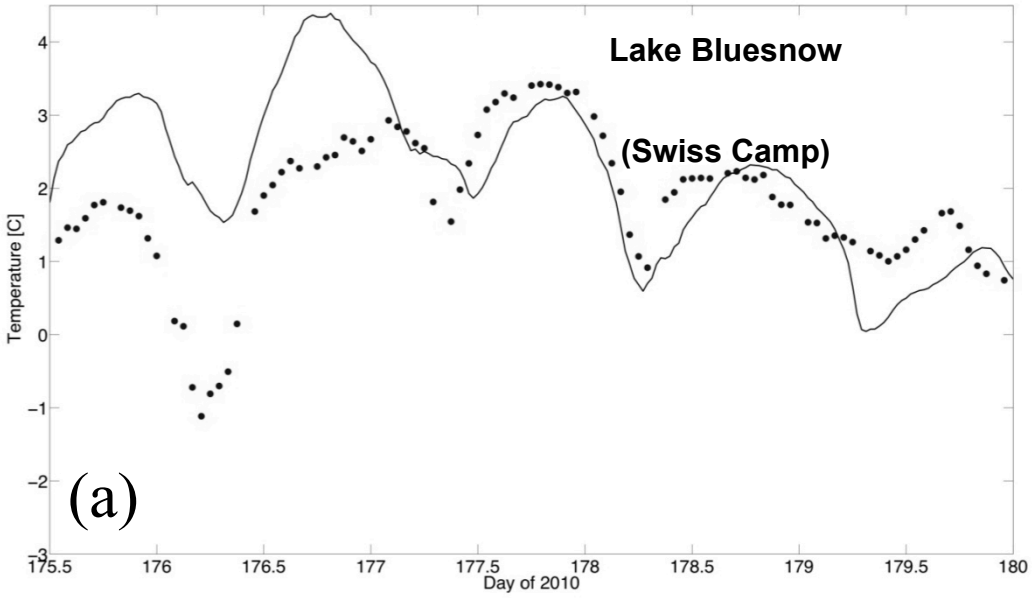

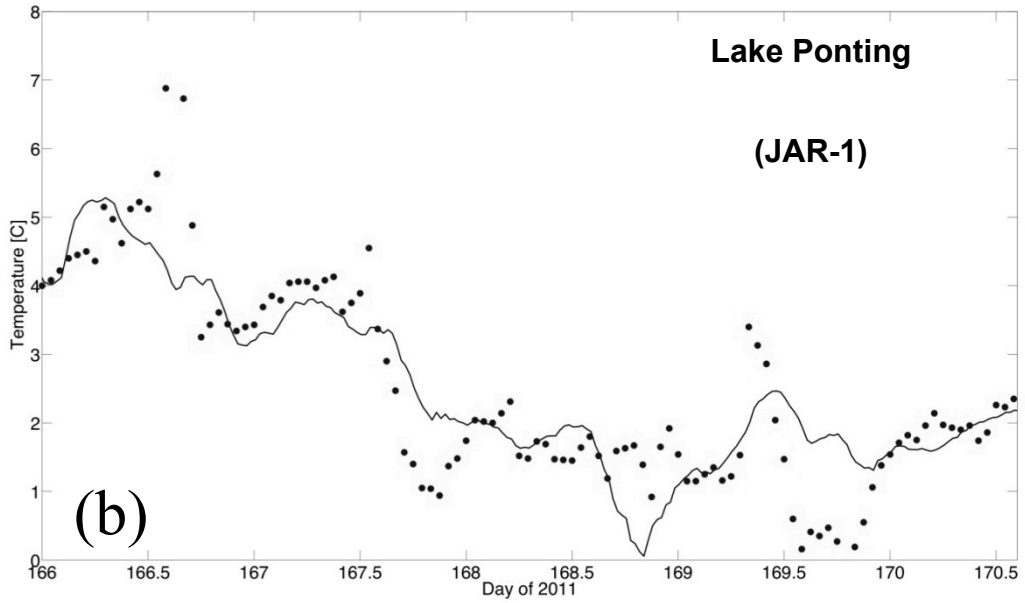
Lake Ponting
(JAR-1)
(b)
Temperature [C]
Day of 2011

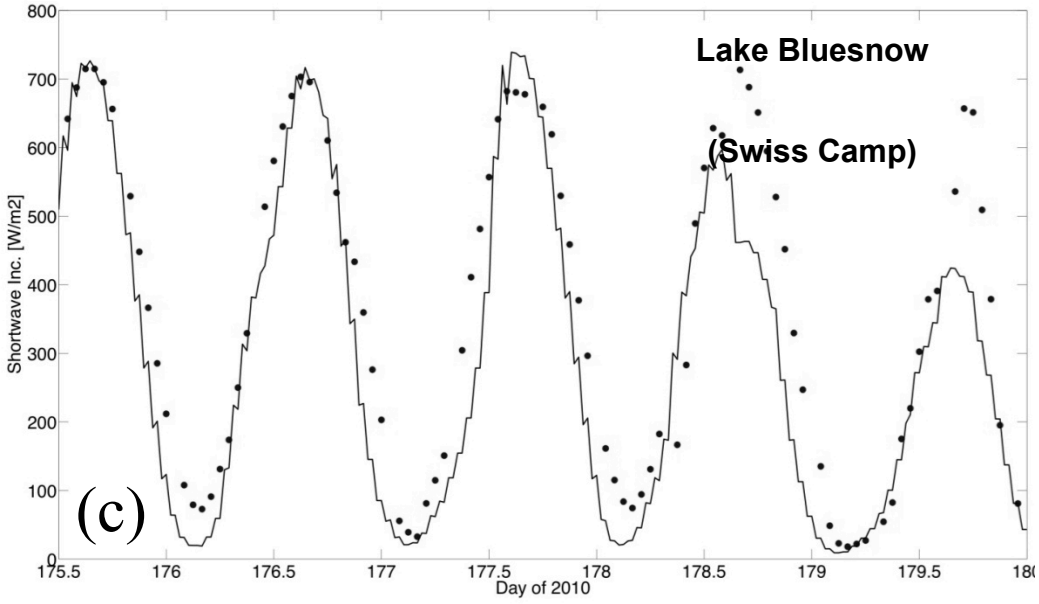
Lake Bluesnow
(Swiss Camp)
(c)
Shortwave Inc. [W/m2]
Day of 2010

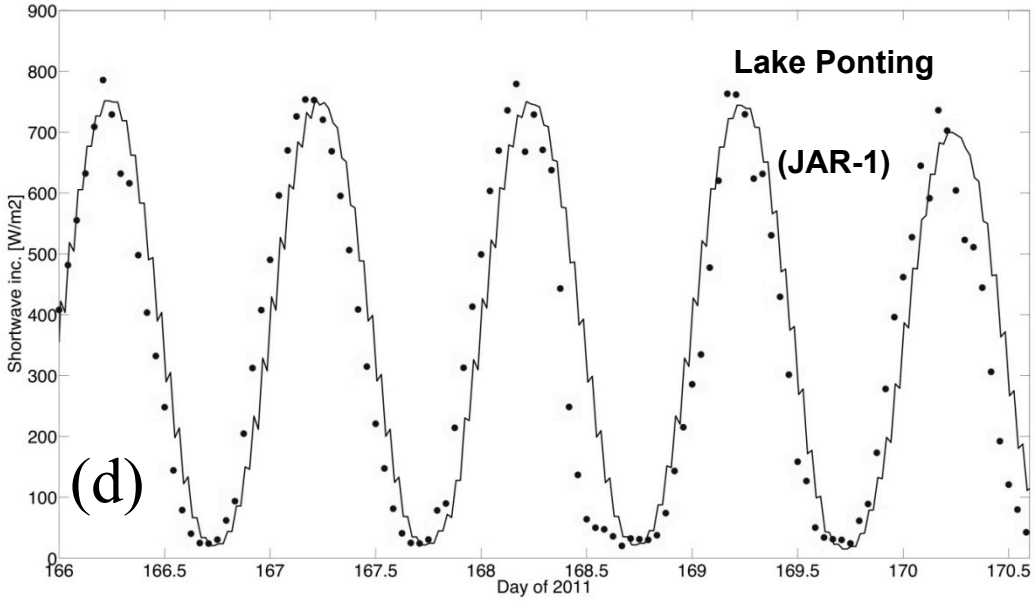
Lake Ponting
(JAR-1)
(d)
Shortwave inc. [W/m2]
Day of 2011

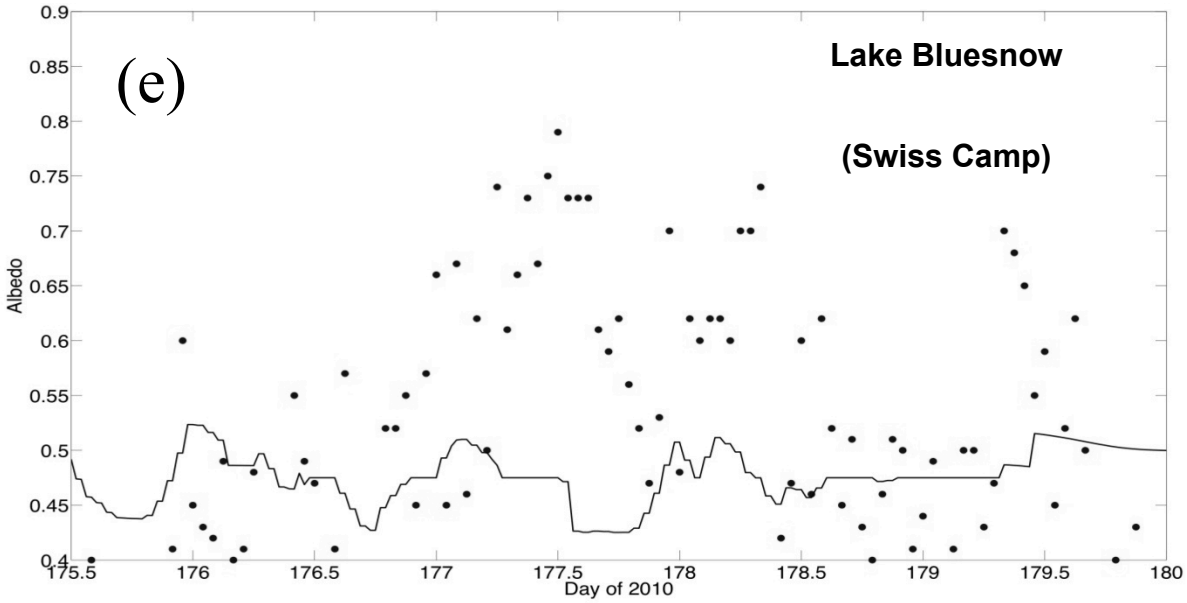
(e)
Lake Bluesnow
(Swiss Camp)
Albedo
Day of 2010

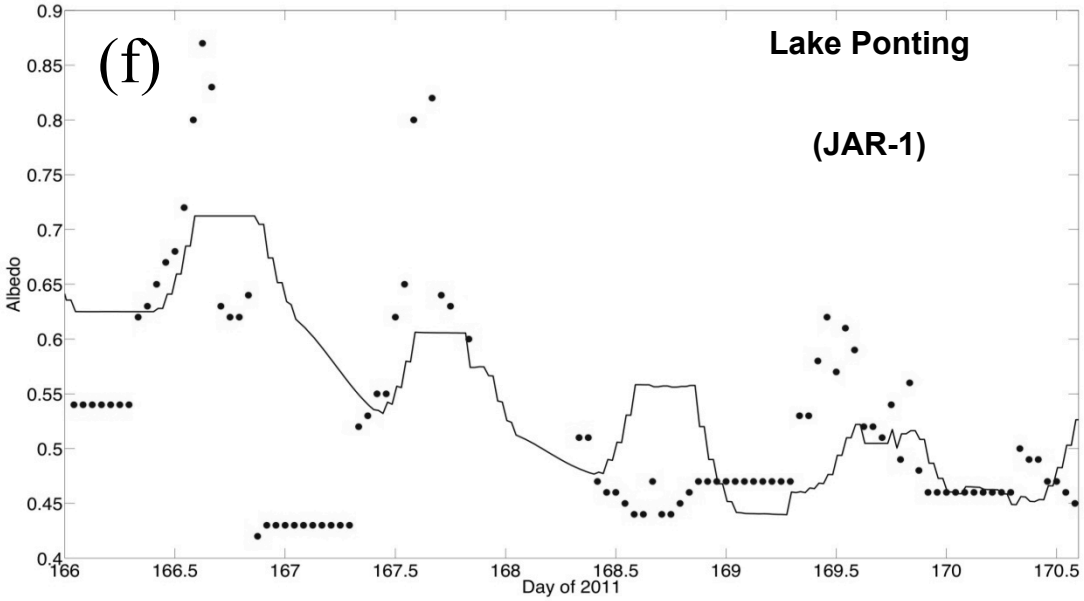
(f)
Lake Ponting
(JAR-1)
Albedo
Day of 2011

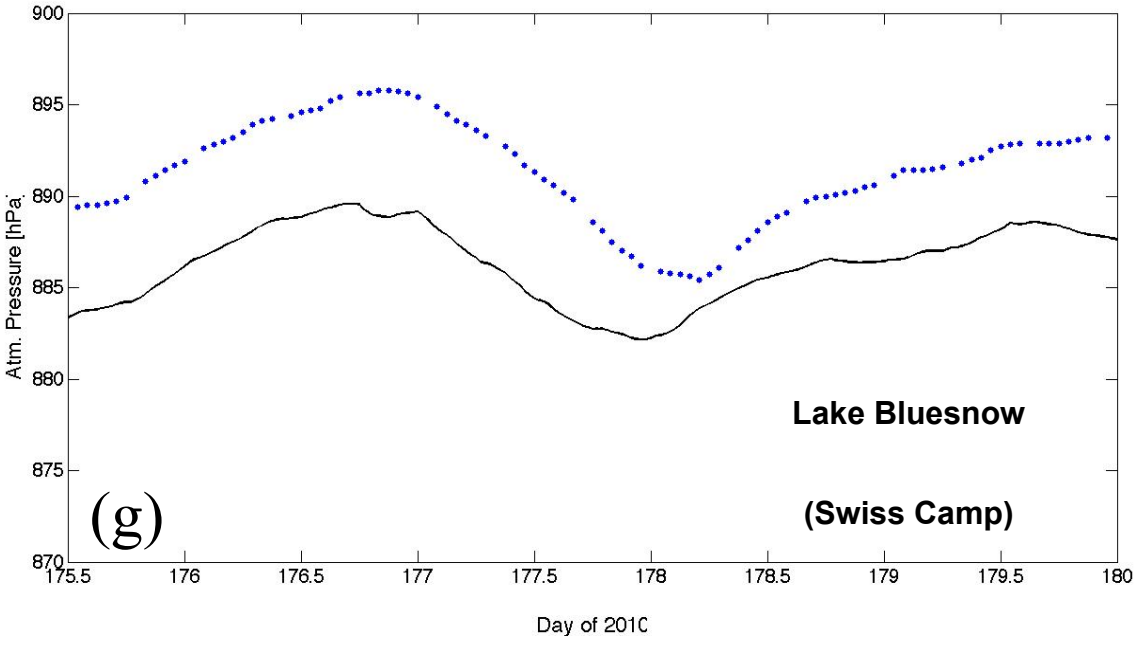
Lake Bluesnow
(Swiss Camp)
(g)
Atm. Pressure [hPa]
Day of 2010

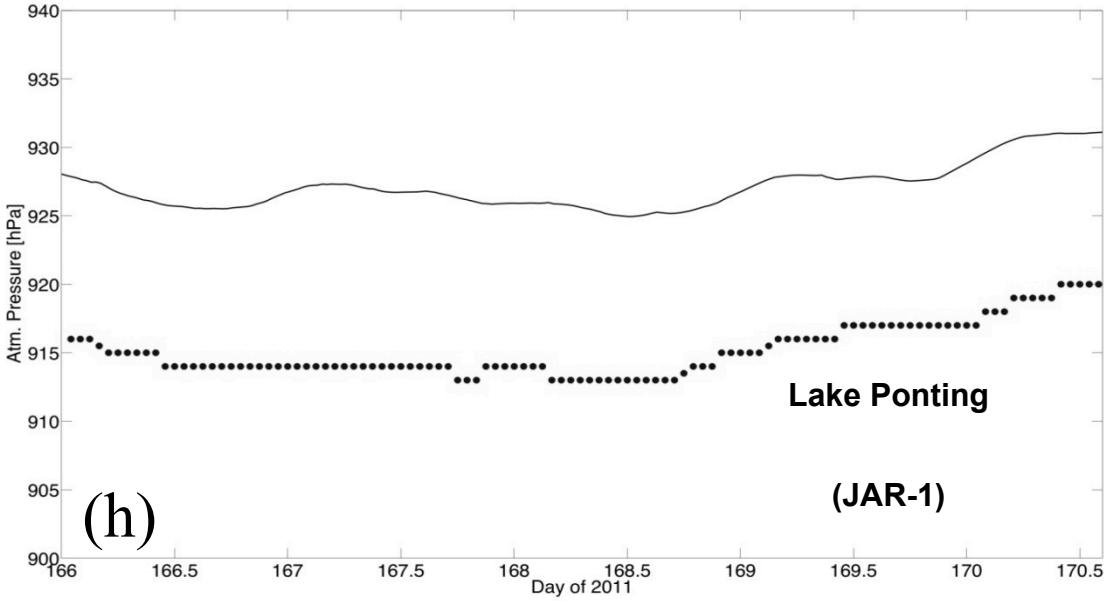

Figure 4-2 GC-Net measured (circles) and MAR simulated (lines) of (a,b) air temperature [ºC], (c,d) shortwave incoming radiation [W/m2], (e,f) albedo and (g,h) atmospheric pressure [hPa] for the Swiss Camp (left plots) and JAR-1 (right plots) stations.

4.5 Results

Figure 4-3 shows the comparison between measured and simulated ABLR (a,c) and water temperatures (b,d) for Lake Bluesnow (a,b) and Lake Ponting (c,d) . In plots a) and c), continuous black lines show the measured ABLR. In plots b) and d), continuous black lines refer to the temperature measured by the top sensor where the dashed black lines indicate the temperature measured by the bottom sensor. As mentioned above, the top sensors were located respectively 2 m (Lake Bluesnow) and 0.7 m (Lake Ponting) above the ice surface when they were deployed. Therefore, in our simulations we assume these values to be the initial water level in the lake to compare modeled and measured ablation rates. However, this might not account for

the ablation occurring during the period when the bottom sensor was underwater but the top sensor was not (on the order of 1 – 2 days). Consequently, to account for this aspect and to evaluate the sensitivity of the model to the initial water level, in Figure 2 we show modeled ablation rates (gray curves with symbols) assuming different initial water levels. In the case of Lake Bluesnow, we show model outputs with initial water level ranging between 0 m (e.g., bare ice) and 3 m. Initial water levels range between 0 m and 1 m in the case of the Lake Ponting.

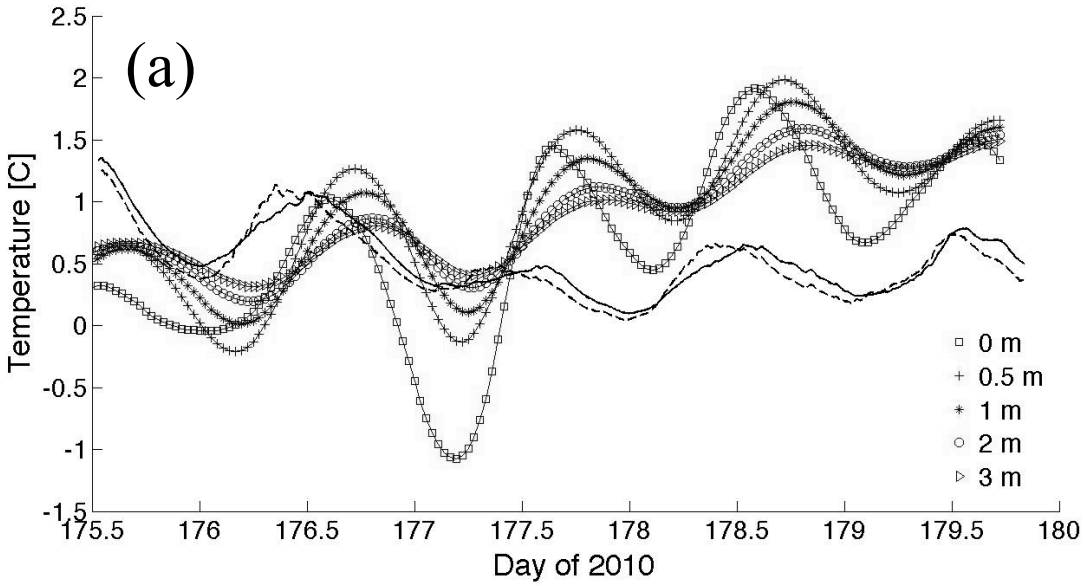

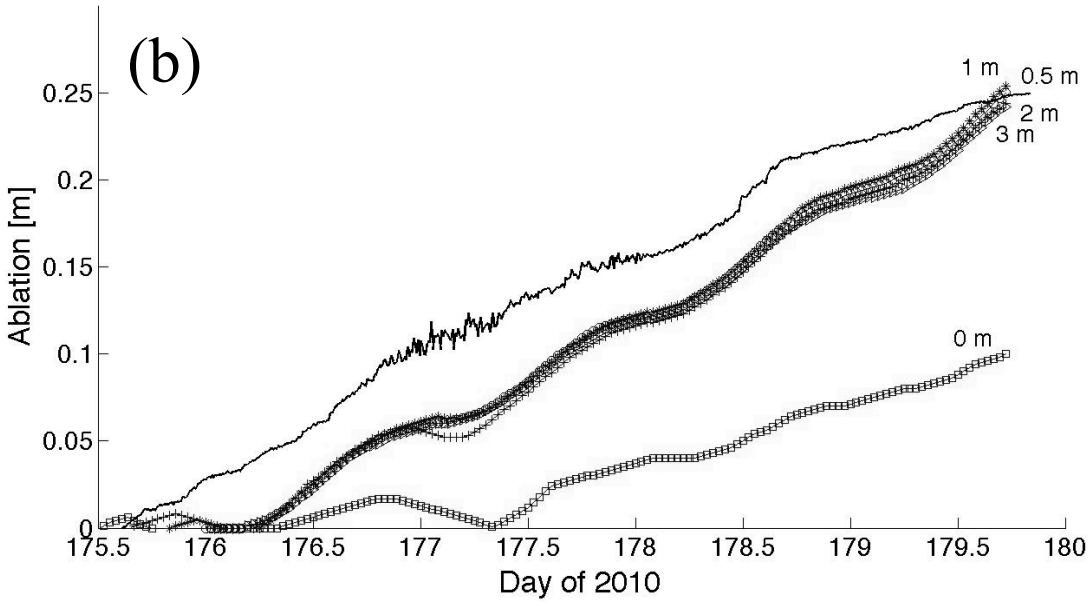
(b)
1 m
0.5 m
2 m
3 m
0 m
Ablation [m]
0.25
0.2
0.15
0.1
0.05
0
175.5
176
176.5
177
177.5
178
178.5
179
179.5
180
Day of 2010

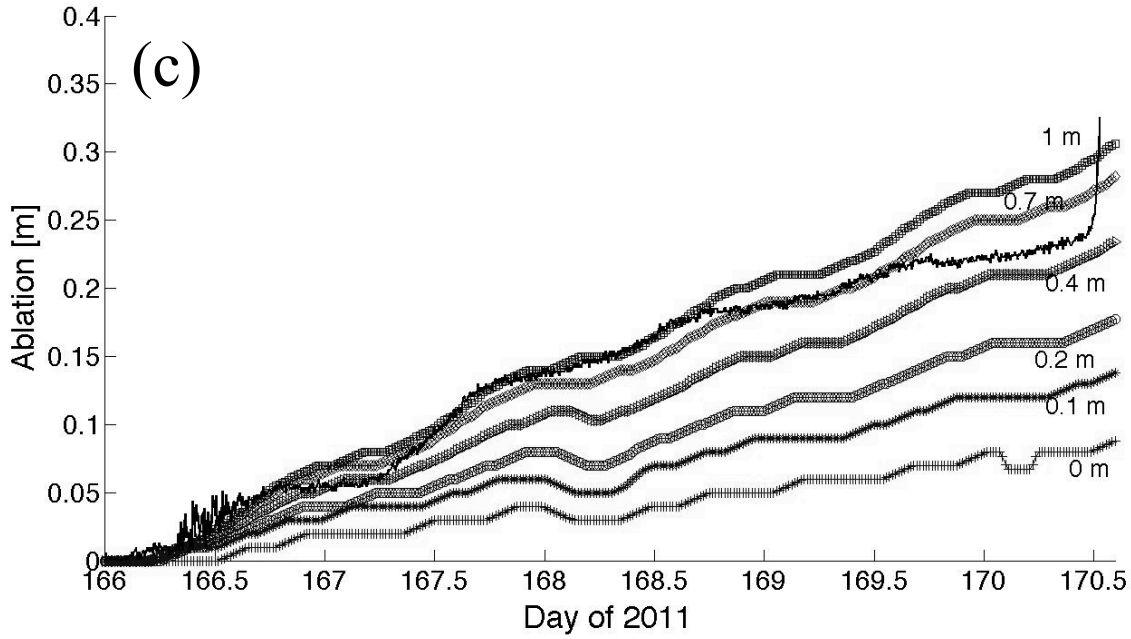
(c)
1 m
0.7 m
0.4 m
0.2 m
0.1 m
0 m
Ablation [m]
0.4
0.35
0.3
0.25
0.2
0.15
0.1
0.05
0
166
166.5
167
167.5
168
168.5
169
169.5
170
170.5
Day of 2011

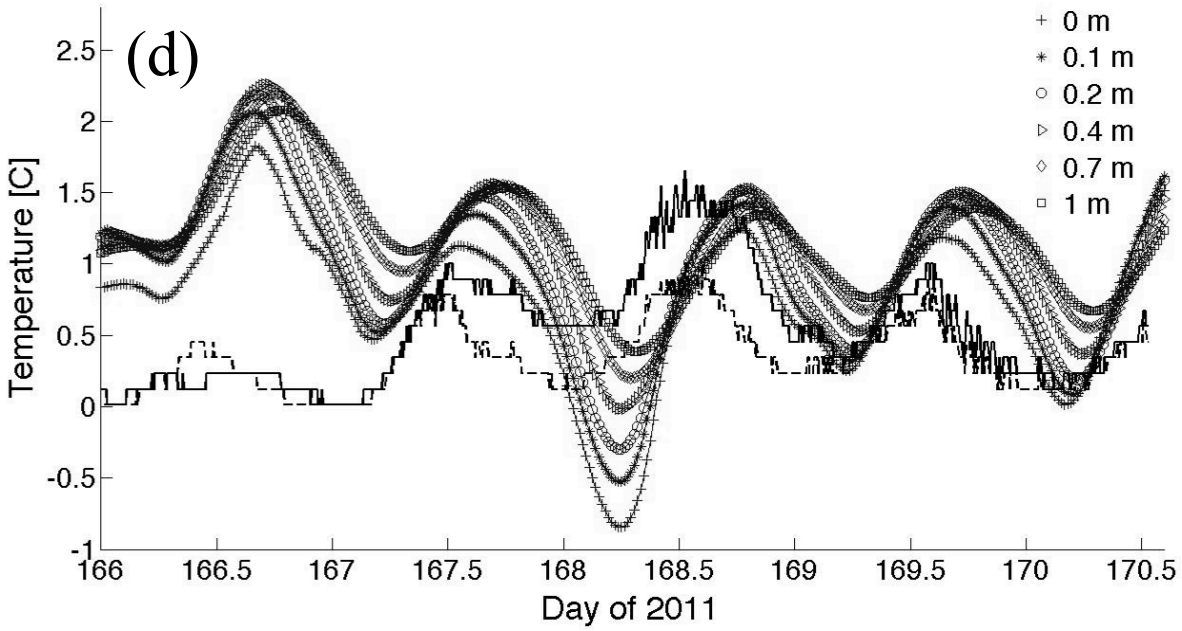

Figure 4-3 GC-Net measured (circles) and MAR simulated (lines) of (a,b) air temperature [ºC], (c,d) shortwave incoming radiation [W/m2], (e,f) albedo and (g,h) atmospheric pressure [hPa] for the Swiss Camp (left plots) and JAR-1 (right plots) stations.

In-situ measurements show that the total measured ablation for the bottom of Lake Bluesnow (Ponting) for the period when both sensors were underwater (~ 5 days in both cases) is ~ 0.25 m (~ 0.33 m) with a linear trend of 6.2 cm/day (5.7 cm/day). Ablation of bare ice over the same period obtained from GC-Net sonic ranger measurements is ~ 0.12 m (0.14 m) in the case of the Swiss Camp (JAR-1) station. Our measurements confirm that the ablation in the case of bare ice is considerably smaller than that measured when the lakes are present. The values of the final ABLR measured at Lakes Blusenow and Ponting are, respectively, 2.1 (110 %) and 2.35 (135 %) times greater than those estimated from GC-Net measurements over bare ice at nearby locations, in agreement with *Lüthje et al. (2006).*

From the analysis of the temperature data, we observe that, in general, the bottom sensors record lower temperature values (dashed line in Figure 4-3 2 b) and d)) than those measured by the top sensors. However, it is not possible to affirm that an actual vertical temperature gradient exists within the water column because the temperature differences between the top and bottom sensors are within the accuracy of the temperature sensor. The time series of the temperatures recorded by the two sensors also indicate that shifts in the relative position of the maxima and minima daily temperature exist (e.g., days 178 – 179 at Lake Bluesnow). A possible cause of this might be the fact that the vertical distance between the two sensors within the lake changes with time (as a consequence of the sinking of the bottom sensor). However, it is not possible to formulate any conclusive hypothesis with the data at our disposal and more measurements could help understanding this issue.

When comparing modeled and measured quantities, for Lake Bluesnow we obtain a rate of 5.4 cm/day when considering an initial water level of 2m (versus a measured value of 6.2 cm/day) and an RMSE between the measured and simulated ablation values of 4.7 cm. For Lake Ponting we obtain a modeled ablation rate of 5.74 cm/day with an initial water level of 0.7 m (versus a measured value of 6.8 cm/day) and an RMSE of 3.2 cm. In contrast to Lake Bluesnow, the model outputs for Lake Ponting are more sensitive to the different considered initial water levels. This is because the values of the initial water level for Lake Ponting are smaller than those we use in the case of Lake Bluesnow. For both lakes, discrepancies between modeled and measured ABLR might be due to intrinsic limitations of the model (e.g., knowledge of physical processes and their implementation) and to the uncertainty associated with the atmospheric forcing generated with the MAR model. We will evaluate the sensitivity of the thermodynamic model to the input parameters by perturbating the MAR outputs within a range that will be decided based

on the relative error between measured and simulated quantities. Factors extrinsic to the model can also be responsible of the differences between the measured and simulated values. For example, the presence of patchy snow and/or of cryoconite, highly absorbing atmospherically transported aerosol, at the bottom of the lake (observed during fieldwork activities). This will act to decrease the albedo of the lake bottom. This aspect is not accounted for in our model but it will, however, affect the measured ABLR.

Temperature values simulated by the model for Lake Bluesnow are consistent with observed values for the first two days of the observational period. For the remaining three days the model generally tends to overestimate the water temperature and the RMSE for the whole period between measured and simulated top (bottom) temperatures (considering an initial water level of 2 m) is 1.64 ºC (1.59 ºC). Conversely, the model tends to overestimate the measured water temperature at the beginning of the observation period in the case of the Lake Ponting, to perform better over the last three days, with an overall RMSE of 1.23 ºC (1.18 ºC) in the case of the temperature measured by the top (bottom) sensor. One possible explanation of the differences between the simulated and measured temperatures is that the model treats the lake as a closed system that heats up, excluding the influx of melt water from the surrounding areas which would eventually tend to cool the water within the lakes.

4.6 Conclusions.

We reported *in-situ* measurements of the ablation rate at the bottom of two supraglacial lakes on the GrIS, together with water temperatures measured at two different depths within the lakes. In agreement with results obtained from previous studies using modeling tools, our measurements indicate that the ablation rate at the bottom of a supraglacial lake is about two times that of an

equivalent nearby bare ice surface. To our knowledge, this is the first time that this is proved through observations, confirming the importance of such lakes for ice sheet surface ablation and hydrological processes. The measured daily ablation rate at the bottom of the two lakes was of the order of ~ 6 cm/day, versus a rate of ~ 2.5 – 3 cm/day in the case of bare ice. This is likely due to an increase in the absorbed solar insulation by water compared to ice and snow. Measured ablation rates at the bottom of the two lakes were compared with those obtained from a physical model forced with the outputs of a regional atmospheric model coupled with a snow physical model. In general, the model was able to satisfactorily reproduce the measured ablation rates, with RMSE values of 4.7 and 3.2 cm, respectively.

We also reported measurements concerning the vertical profile of water temperature. Observed differences between the temperatures measured at different depths were smaller than the accuracy of the temperature sensors, hence making impossible to draw any conclusion. The model was generally capable of reproducing the water temperature (assumed to be uniform in the model), though overestimation by the model occurred.

The results reported in this study confirm that the ablation at the bottom of supraglacial lakes can play an important role on the overall lake volume. For example, in the case of Lake Ponting the overall depth of the lake increased by ~ 3m during the period when both sensors were underwater, of which 0.33 m due to the melting of its bottom. This can be be especially important for those lakes whose lifetime is relatively long, especially those that do not drain during a melt season (*Selmes et al., 2011)*. Moreover, studies investigating ice sheet surface hydrology processes, and in particular those modeling runoff and streamflow, should account for the ablation of the bottom of the lakes. The general agreement between measured and modeled

quantities for the two lakes studied in this paper suggests that it would be possible to account for this quantity by forcing the ablation model used in this study with outputs from the MAR model.

Acknowledgments

The work at City College of New York was supported by the NASA Cryosphere Program and the NSF grant ANS 0909388. World Wildlife Fund (WWF), St Catharine's College, Scandinavian Studies Fund, and B.B. Roberts Fund are all acknowledged for financially supporting part of the fieldwork activities.

4.7 References

Alexiades, V., and A.D. Solomon (1993), *Mathematical modeling of melting and freezing processes.* Washington DC, Hemisphere Publishing Corp.

Box, J. E., and K. Ski (2007), Remote sounding of Greenland supraglacial melt lakes: implications for subglacial hydraulics, *Journal of Glaciology, 53, No. 181*

Das, S.B., I. Joughin, M. D. Behn, I. M. Howat, M. A. King, D. Lizarralde, and M. P. Bhatia (2008), Fracture Propagation to the Base of the Greenland Ice Sheet During Supraglacial Lake Drainage, *Science, 320, 5877*, pp. 778 – 781, DOI: 10.1126/science.1153360

Fettweis, X. (2007), Reconstruction of the 1979-2006 Greenland ice sheet surface mass balance using the regional climate model MAR, *The Cryosphere, 1, 21-40*

Fettweis, X., M. Tedesco, M. van den Broeke, and J. Ettema (2011), Melting trends over the Greenland ice sheet (1958–2009) from spaceborne microwave data and regional climate models, *The Cryosphere*, *5, 359-375*, doi:10.5194/tc-5-359-2011

Lüthje, M., L.T. Pedersen, N. Reeh, and W. Greuell (2006), Modelling the evolution of supraglacial lakes on the West Greenland ice-sheet margin, *Journal of Glaciology*, *52(179)*

Linden, P.F (2000), *Convection in the environment*. In Bachelor, G.K., H.K. Moffatt and M.G. Worster, eds. Perspectives in fLiud mechanics, Cambridge, Cambridge University Press, 287–343

McMillan, M., P. Nienow, A. Shepherd, T. Benham, and A. Sole (2007), Seasonal evolution of supra-glacial lakes on the Greenland Ice Sheet, *Earth and Planetary Science Letters* 262, 3-4, 484-492

Pimentel, S., G.E. Flowers, and C.G. Schoof (2010), A hydrologically coupled higher-order flow-band model of ice dynamics with a Coulomb friction sliding law, *J. Geophys. Res.* 115, F04023, doi:10.1029/2009JF001621

Selmes, N., T. Murray, and T. D. James (2011), Fast draining lakes on the Greenland Ice Sheet, *Geophys. Res. Lett.*, *38*, L15501, doi:10.1029/2011GL047872.

Sneed, W. A., and G. S. Hamilton (2007), Evolution of melt pond volume on the surface of the Greenland Ice Sheet, *Geophysical Research Letters*, **34**, L03501, doi:10.1029/2006GL028697

Sneed, W. A., and G. S. Hamilton (2011), Validation of a method for determining the depth of glacial melt ponds using satellite imagery, *Annals of Glaciology 52(59)*, 15 – 22

Steffen, K., J. E. Box, and W. Abdalati (1996), Greenland Climate Network: GC-Net, in Colbeck, S. C. Ed. CRREL 96-27 Special Report on Glaciers, Ice Sheets and Volcanoes, tribute to M. Meier, 98-103

Sundal, A.V., A. Shepherd, P. Nienow, E. Hanna, S. Palmer, and P. Huybrechts (2011), Melt-induced speed-up of Greenland ice sheet offset by efficient subglacial drainage, *Nature*, 469 (7331): 521 DOI: 10.1038/nature09740

Tedesco , M. , X. Fettweis, M. R. van den Broeke, R. S. W. van de Wal, C. J. P. P. Smeets, W. J. van de Berg, M. C. Serreze, and J. E. Box (2011), The role of albedo and accumulation in the 2010 melting record in Greenland, *Environ. Res. Lett.* 6 014005

Tedesco M., and N. Steiner (2011), In-situ multispectral and bathymetric measurements over a supraglacial lake in western Greenland using a remotely controlled watercraft *The Cryosphere*, 5, 445-452

Conclusions and Future Study

5 Conclusions

Observations of melt processes for the Greenland and Antarctica Ice Sheets (GrIS and AIS, respectively) are important in quantifying current melting rates and for predictions for the response to glaciers to future climate change. This work introduces methods that advance the current capability to observe melt processes, both from in-situ measurements and remote sensing techniques. Specifically two melt related processes are addressed: the total extent and duration of seasonal surface melting for the AIS and melting ponding on the GrIS. These two processes are integral to the rate of total ice loss for the AIS and GRIS, since surface melting leads to runoff and melt ponding. Melt ponding, in turn, leads to increased discharge during drainage events as well as an increase in the rate of ablation of the ice sheet.

Microwave frequency and visible-near infrared satellite methods are employed in this work to successfully gather information on melt processes. This study leverages the advantages of both instrument types to maximize their potential to observe melt processes (i.e. discerning liquid water from ice at the surface or just below). Microwave frequency satellite instruments have large magnitude response to liquid water as well as a high temporal resolution and spatial coverage (due to large spatial coverage and ability to penetration cloud cover) making it optimal for measuring melting extent. Microwave instruments are less adept at detecting high spatial detail or resolving contrasts in liquid water content (LWC). Visible-NIR wavelength satellite instruments have the ability to make high resolution observations and due to their greater penetration depth into water at blue to green wavelengths can be used to estimate water depth from upwelling radiance measurements.

The presently advanced study of the visible-near infrared spectrum finds that a) it is feasible for supraglacial lake depths to be retrieved using a focus on vis-nir, and b) the accuracy of these estimates validities existing estimates for water flux to the base of glaciers. Detailed in-situ concurrent multi-spectral and depth observations, collected over a supraglacial lake in West Greenland were used to evaluate the spectral dependency of the bottom albedo, A_d, diffuse absorption factor and to quantify spaceborne bathymetry. The latter linearly relates the attenuation coefficient g and the diffuse attenuation factor K_d. Results show that, as hypothesized, the spectral behavior of A_d is similar to that of glacier ice albedo. The increase of a with wavelength from in-situ data cannot be easily explained without assuming chlorophyll, or other absorbing materials in the water, which is present in minimal concentrations according to preliminary analysis of water samples. One explanation for the spectral behavior follows that the bottom albedo has a greater variability in the blue region. With a fixed bottom albedo, some of the loss due to a darker blue ice is attributed to loss along the water column. By assessing a widely-used technique in which A_d is assumed to be uniform and equal to the reflectance of shallow waters along the lake edge it is demonstrated that estimates of A_d manifest Gaussian-like behavior. This indicates that there is an expected and quantifiable error associated with A_d data that will be reflected in estimates derived for lake depth. The present study attributes the bulk of the variability to differences in the reflectivity of heterogeneous ice and to cryoconite – a dark aerosol that contributes to a reduction in albedo that is hard to directly quantify.

In the case of ***a***, a second attenuation factor, values obtained from in-situ measurements differ by ~15 % from those computed using literature approaches. Best spaceborne-based estimates resulted when using either the Landsat band 2 or the spectrally similar MODIS band 4. In the case of Landsat, the best results are obtained when using the ***a*** derived from in-situ

measurements ($\boldsymbol{a}$ = 2.33). However, this is not true in the case of MODIS, where best results are obtained using the values suggested in the literature ($\boldsymbol{a}$ = 2). In the case of MODIS, however, mixed-pixel effects and relatively coarse resolution can be responsible for a large degree of uncertainty.

A combined continuous wavelet transform and multi-scale analysis (CWT) is able to isolate changes in the backscattering signal upon melting events. The CWT methodology, in itself, can identify all discontinuous changes in a single season of QuikSCAT backscatter observations. Based on the fundamentals of wavelet analysis, the set of identified discontinuous changes must include both the point of melt onset and the point of refreeze, providing there is melting. By considering only those transitions with substantial large-scale components, here defined as greater than 2^5 days, small-scale transitions similar to signal noise are eliminated. The addition of multi-scale analysis also eliminates those transitions that are sporadic (noisy in time). The combination of these methods provides a melt detection methodology aimed at detecting melting at a seasonal scale that may represent a substantial improvement over traditional measurements as discussed in the future studies section.

Results from the CWT method, when compared with a fixed threshold methodology find melt durations (MD) that are well correlated, $r = .897$ $(p < 0.001)$ in mean value, with a root mean squared error (RMSE) of ~ 9 days. Generally, the CWT method has a positive bias of ~ 15 days with respect to the FT3, due to the identification of only sustained melting during the melting season. From single season observations, it is evident that the major sources of negative differences in algorithm results (FT3>CWT) are from fluctuations in backscatter close to the 3dB threshold, and most likely from short refreeze cycles or a lower magnitude backscatter change with increasing LWC. From the evaluation of melting over the Antarctic Peninsula (AP) for both

methodologies, it is found that the average MD difference is less than at the continent scale, indicating that a majority of sporadic, large-scale, melting events occur primarily on low elevation ice-shelves and that at higher elevations on the AP. This is an expected result for the Antarctic Peninsula that comparatively receives a majority of the weather.

Additionally, a comparison with AWS reveals that overall the FT3 has higher level of agreement with the temperature measurements with a 66 percent total accuracy compared to the 54 percent from the CWT method. The FT3 method has a better overall accuracy because of its ability to measure short duration melting events that are common for several stations (e.g. the Limbert AWS) and are expressed in the air temperature record. This is true for all AWS, apart from the Pegasus South Station where the CWT has a 10 percent greater accuracy than the FT3 method. For the Pegasus South AWS, it appears that the melting season occurs with a relatively low loss in backscatter, it is therefore never consistently under the 3dB threshold.

A comparison between active (QuikSCAT) and passive microwave instruments (SSM/I), we find that methods find similar values in terms of total melt index (MI) compared to M+30K, a PMW derived approach; both AMW melting records similar yearly MI.

In chapter 2, in-situ concurrent multi-spectral and depth observations were collected over a supraglacial lake in West Greenland in order to assess spaceborne bathymetry. Such measurements provided the opportunity to study the spectral dependency of the bottom albedo *Ad* and coefficient *a,* with the latter linearly relating the attenuation coefficient *g* and the diffuse attenuation factor *Kd.* Results show that, as expected, the spectral behavior of *Ad* is similar to that of glacier ice albedo. The increase of *a* with wavelength from in-situ data cannot be easily explained without assuming chlorophyll, or other absorbing materials, in the water, which is

present at a very minimal concentration according to our preliminary analysis of water samples. One explanation for the spectral behavior of *a* is that the bottom albedo has a higher variability in the blue region, attributing some of the loss due to a darker blue ice to loss along the water column.

This study reexamined a technique widely used in the literature in which Ad is assumed to be uniform and equal to the reflectance of shallow waters along the lake edge. The analysis of in-situ measurements show a Gaussian-like behavior of *Ad,* with this variability appearing to be intrinsic to the albedo of the bottom, consisting of large patches of cryoconite. The difference between the mean *Ad* value obtained from in-situ measurements and the mean of the reflectance values along the lake edge obtained from Landsat is on the order of ~ 10 %. This translates into an average error on lake depth retrieval of -11.8 % (-15.9 %) when using the Landsat band 1 (band 2). The error is maximum for shallow waters with an underestimation down to -23.7 % (-42.7 %) and reduces to -4.6 % (-4.7 %) for lake depth values up to 10 m.

In the case of *a*, the values obtained from in-situ measurements differ by ~ 15 % from those computed using literature approaches. Best spaceborne-based estimates were obtained when using either the Landsat band 2 or the spectrally similar MODIS band 4. In the case of Landsat, best results are obtained when using the ***a*** value derived from in-situ measurements (***a*** **= 2.**33**)**. However, this is not true in the case of MODIS, where best results are obtained using the values suggested in the literature (***a*** **= 2**). In the case of MODIS, however, mixed-pixel effects and relatively coarse resolution can be responsible for large uncertainty. For example, the presence of ice within a pixel will increase the reflectance with respect to a pixel containing only liquid water, leading to an underestimation of the lake depth. This is especially true for relatively small lakes and for those pixels containing the lake edges. In the future, a more comprehensive

collection of in-situ data set on the inherent optical properties of melt pond water is planned at multiple lakes. This will facilitate the use a more sophisticated model of the water column (*Lee, 1999*), in which depth estimations can be made with a fully physical model of water constituents.

In Chapter 3, *in-situ* measurements of the ablation rate at the bottom of two supraglacial lakes on the GrIS are reported, together with water temperatures measured at two different depths within the lakesThese results agree with those obtained from previous studies using modeling tools, with measurements indicating that the ablation rate at the bottom of a supraglacial lake is about two times that of an equivalent nearby bare ice surface. To our knowledge, this is the first time that this is proved through observations, confirming the importance of such lakes for ice sheet surface ablation and hydrological processes. The measured daily ablation rate at the bottom of the two lakes was of the order of ~ 6 cm/day, versus a rate of ~ 2.5 – 3 cm/day in the case of bare ice. Measured ablation rates at the bottom of the two lakes were compared with those obtained from a physical model forced with the outputs of a regional atmospheric model coupled with a snow physical model. In general, the model was able to satisfactorily reproduce the measured ablation rates, with RMSE values of 4.7 and 3.2 cm, respectively.

We also reported measurements concerning the vertical profile of water temperature. Observed differences between the temperatures measured at different depths were smaller than the accuracy of the temperature sensors, hence making impossible to draw any conclusion. The model was generally capable of reproducing the water temperature (assumed to be uniform in the model), though overestimation by the model occurred.

The results reported in this study confirm that the ablation at the bottom of supraglacial lakes can play an important role on the overall lake volume. For example, in the case of Lake Ponting the

overall depth of the lake increased by ~ 3m during the period when both sensors were underwater, of which 0.33 m due to the melting of its bottom. This can be especially important for those lakes whose lifetime is relatively long, especially those that do not drain during a melt season. Melting at the bottom of a supraglacial lake might also be expected to alter its reflective properties, with implications for satellite-based techniques used to estimate lake volume from visible and near-infrared observations. Such techniques assume that the reflective properties of the bottom of the lake are the same as those of the areas along the lake shore. Given the different ablation rates between bare and water-covered ice, the assumption adopted in the satellite-based techniques might introduce error on the lake volume estimates if the optical properties of the ice exposed at the bottom of the lake are different from those at the lake's edge. Moreover, studies investigating ice sheet surface hydrology processes, and in particular those modeling runoff and stream-flow, should account for the ablation of the bottom of the lakes.

6 Future Study

The CWT method makes it possible to filter changes based on multiple scale components. It would be advantageous in future study to find an optimal scale for the measurement of synoptic melting events. Currently, the choice of a minimum temporal threshold is based on previous work (see Chapter 1). A quantitative method to optimize the scale threshold based on direct field observations would constitute a substantial improvement to the method. This may be implemented by using long-term spatial patterns in seasonal above-zero temperatures, or other climate parameters, to derive a scale based directly on observations from model data or reanalysis data. In this way we can create an observationally tuned time-scale threshold that would reduce the effect of weather events on the melting record.

Because of the nature of a dynamic-change methodology, the method is not limited to the instrumentation that it is currently applied. The importance of this is illustrated in the case of the QuikSCAT satellite that experienced antennae failure in 2009, limiting the scope of the observational record. Currently operational satellite scatterometers, including the ASCAT instrument, do not match previous instrumentation in frequency or tempo-spatial resolution. Based on differences in the microwave response to LWC, a fixed-threshold melt-detection method, as currently defined, cannot be applied directly to this new data record. Additional investigation is required to establish an appropriate threshold. Conversely, since the main requirement for a dynamic method, that the microwave response to LWC remains much greater than other snow property changes, the method still applies for ASCAT, a C-band scatterometer, Therefore the CWT method can be applied directly because the timing of melting remains the same while the magnitude changes.

An additional use of the CWT, currently funded, is directed at comparing QuikSCAT-derived melt record with the regional climate (MAR). This will help to extend the current melting record for the Antarctic Peninsula to mid-twentieth century. These combined proposed studies are anticipated to place the melting interval for glacial on a much-improved footing.

In the future, a more comprehensive in-situ data set will be collected on the inherent optical properties of melt pond water with analysis extended to multiple lakes. A more sophisticated model of the water column will be implemented, in which depth estimations can be made with a fully physical model of water constituents.

The general agreement between measured and modeled ablation rates for the two lakes studied in Chapter 3 suggests that it would be possible to account for this quantity by forcing the ablation

model used in this study with outputs from the MAR model. This would be the natural extension of this particular study.

A. Appendix - *Supplemental Material for Chapter 2*

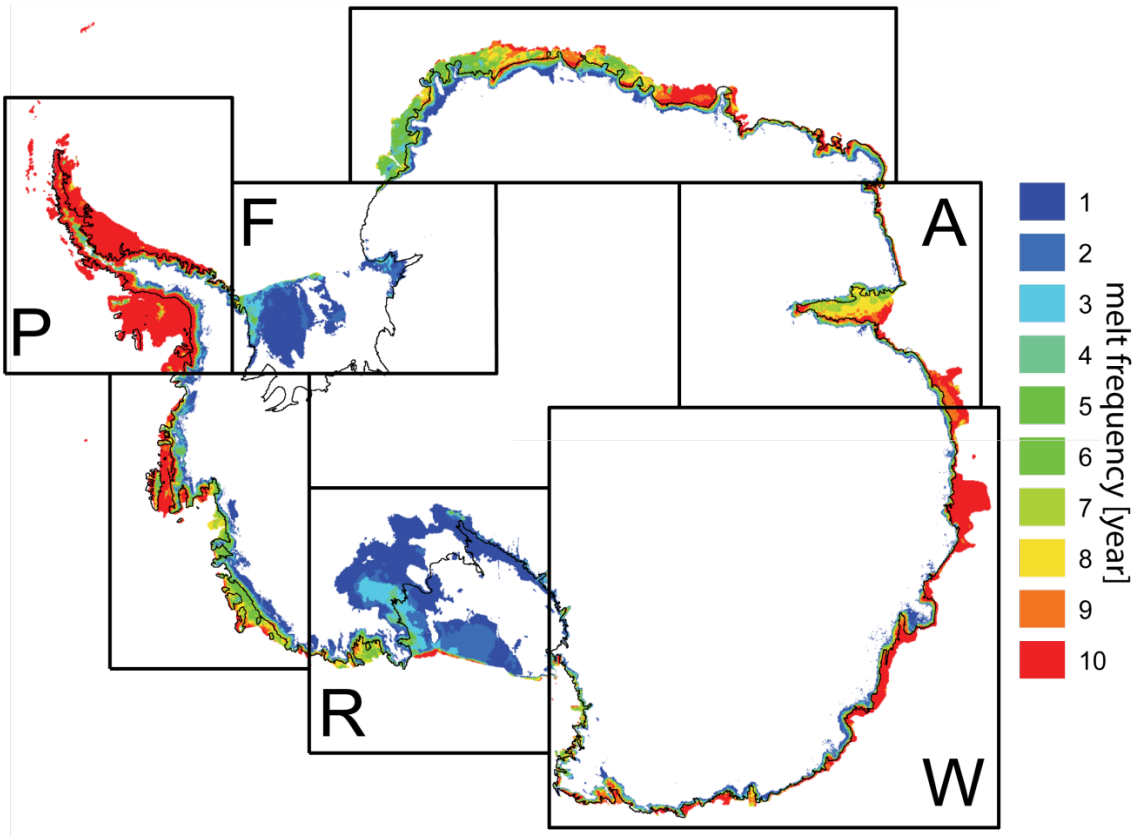

Figure A-1 The observed frequency of yearly melting for the period 1999:2009. Sections refer: Antarctic Peninsula (P), Fimbilt (F), Dronning Maude Land (D), Amery (A), Wilkes Land (W), Ross (R), Marie Byrd Land (M)

.

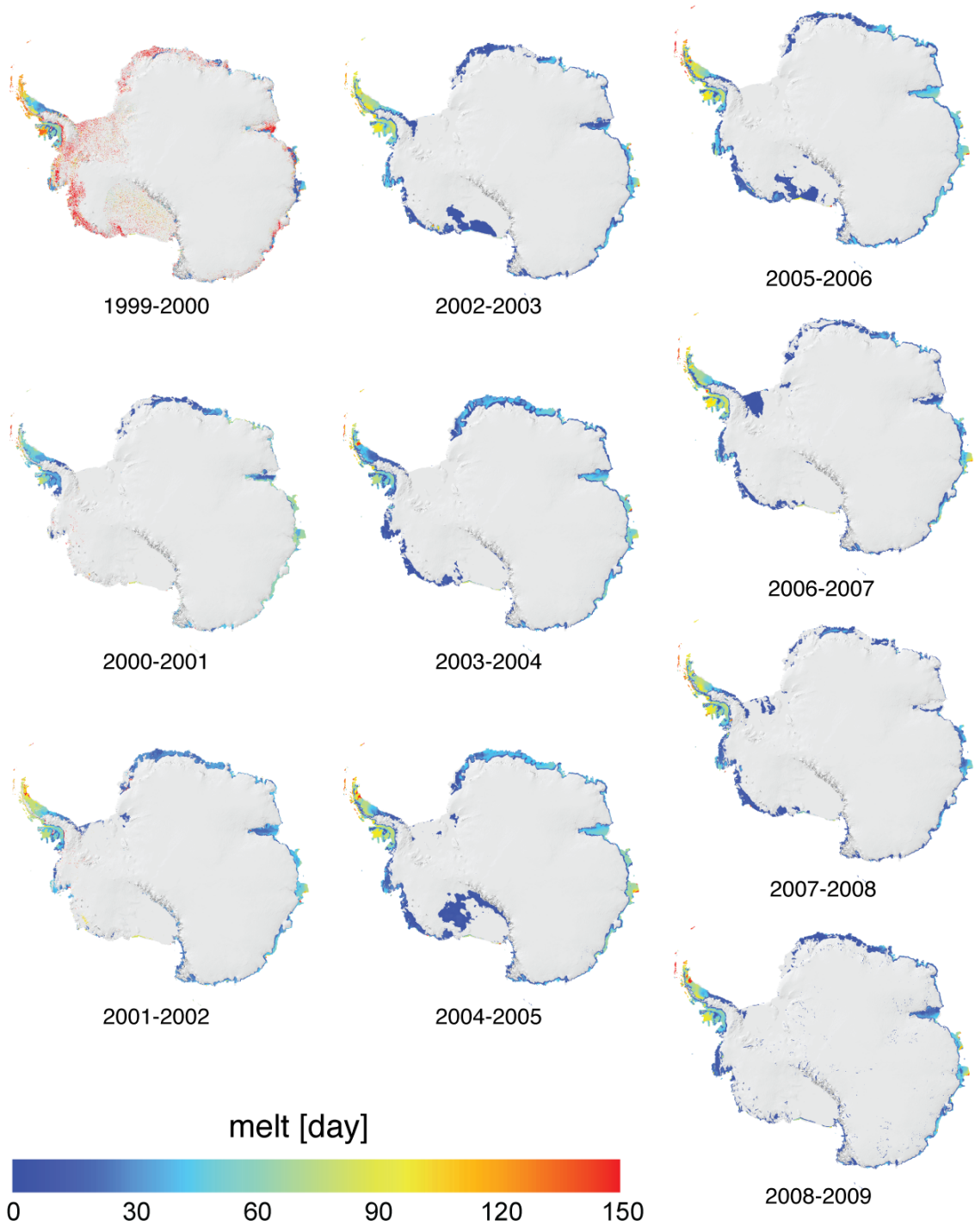

Figure A-2 Yearly melt duration as determined by the CWT method

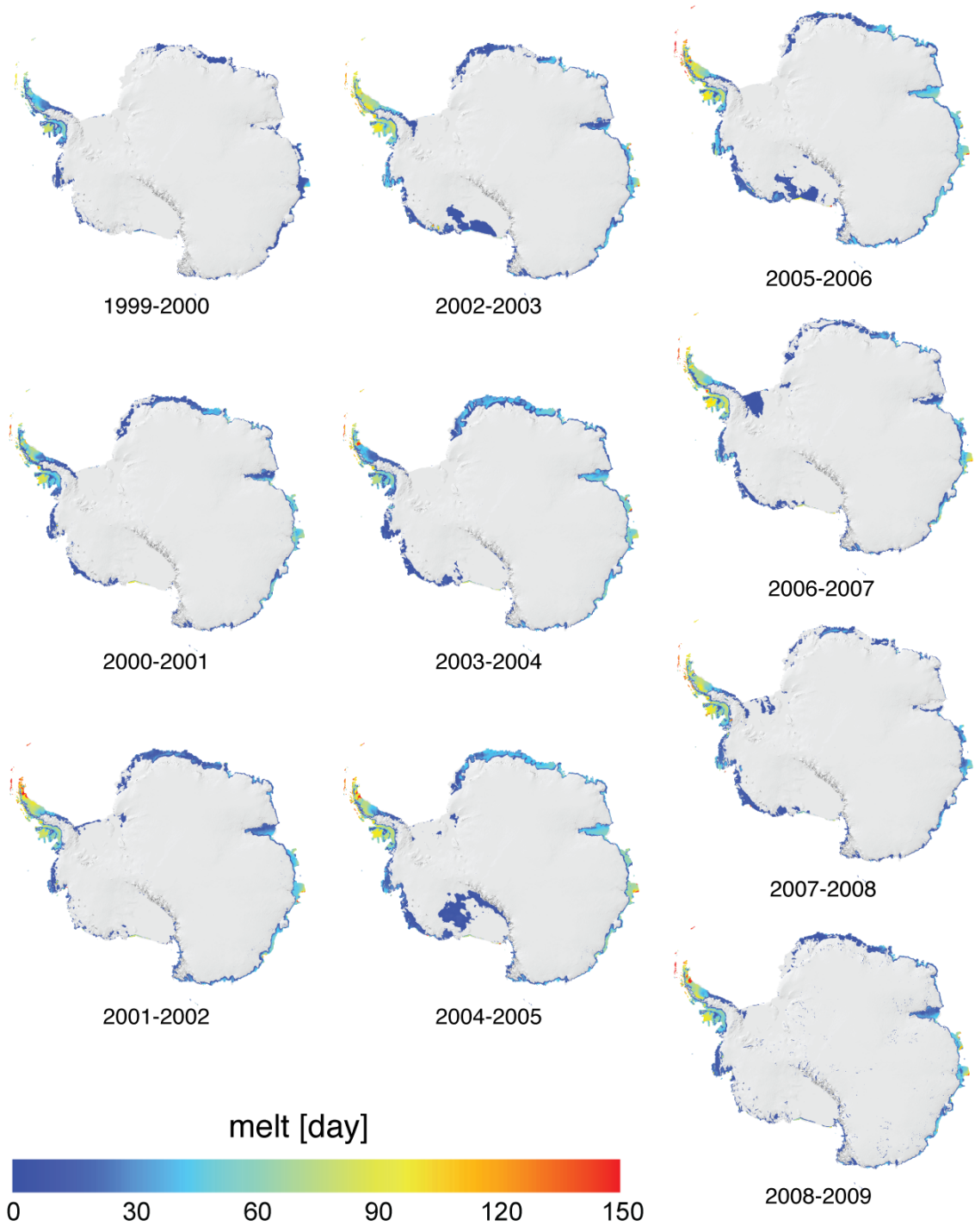

Figure A-3 Yearly melt duration as determined by the FT3 method

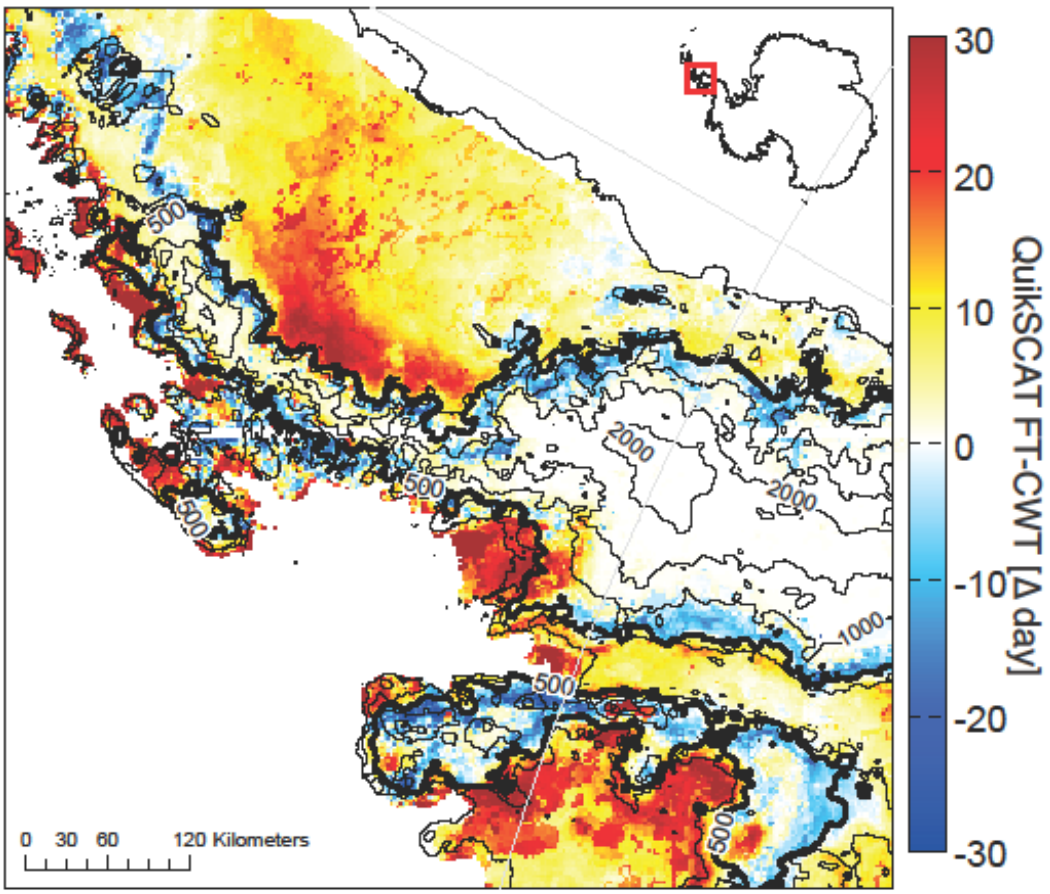

Figure A-4 Difference in MD for an enlarged section of the Antarctic Peninsula as found by the CWT and FT3 methods, where$\Delta MD = (MD_{FT3} - MD_{CWT})$. Elevation contours from Bamber et al (2009)[1].

[1] Bamber, J., Gomez-Dans, J., & Griggs, J. (2009). A new 1 km digital elevation model of the Antarctic derived from combined satellite radar and laser data–Part 1: Data and methods. *The Cryosphere, 3*(1), 101-111.

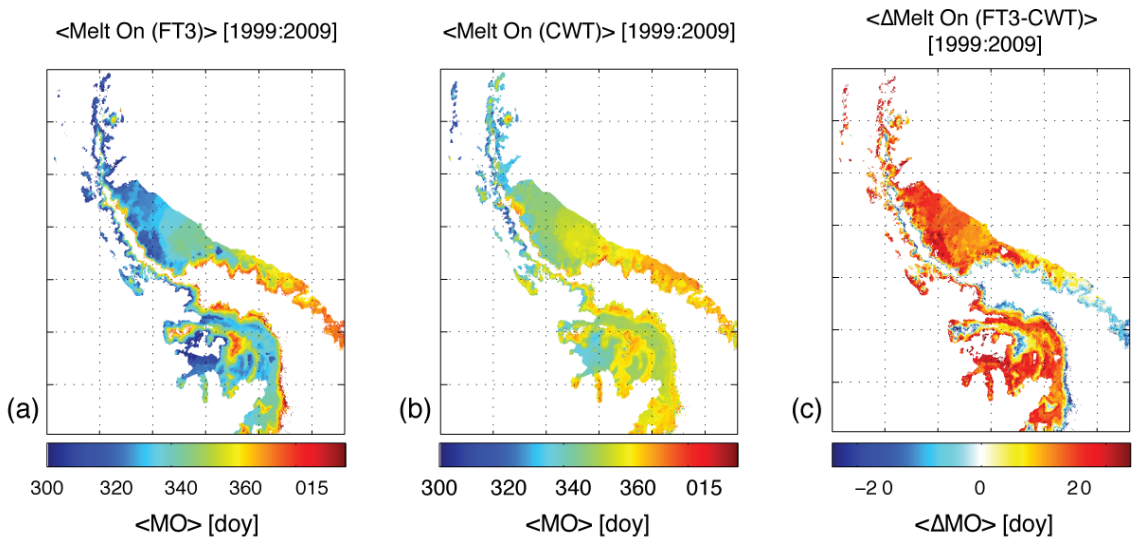

Figure A-5 Mean melt onset over the Antarctic Peninsula determined using (a) FT3, (b) CWT and (c) the difference between FT3 and CWT where $\Delta MO = (MO_{FT3} - MO_{CWT})$

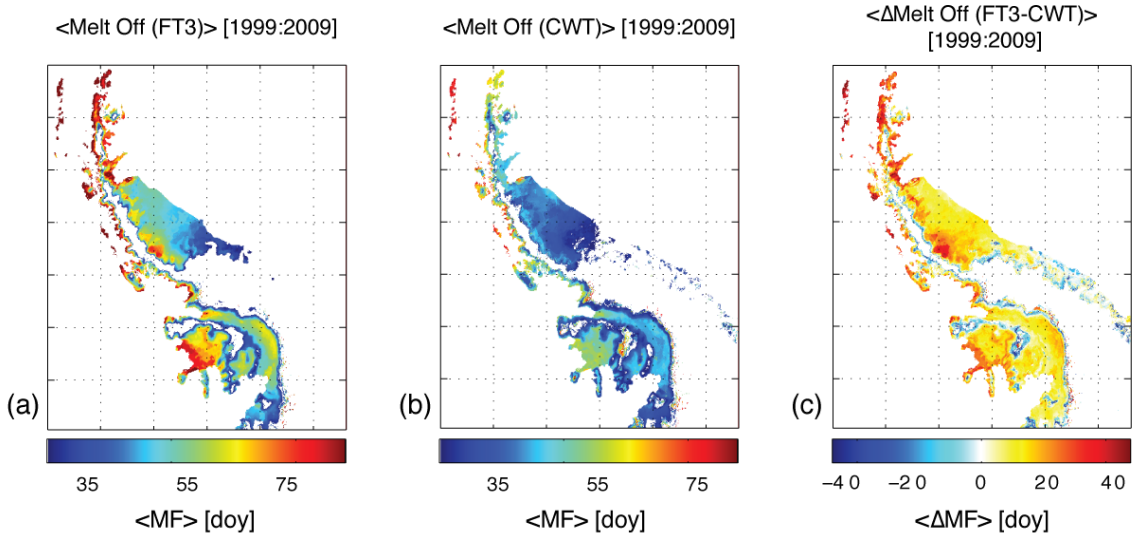

Figure A-6 Mean melt refreeze date over the Antarctic Peninsula determined using (a) FT3, (b) CWT and (c) the difference between FT3 and CWT where $\Delta MF = (MF_{FT3} - MF_{CWT})$

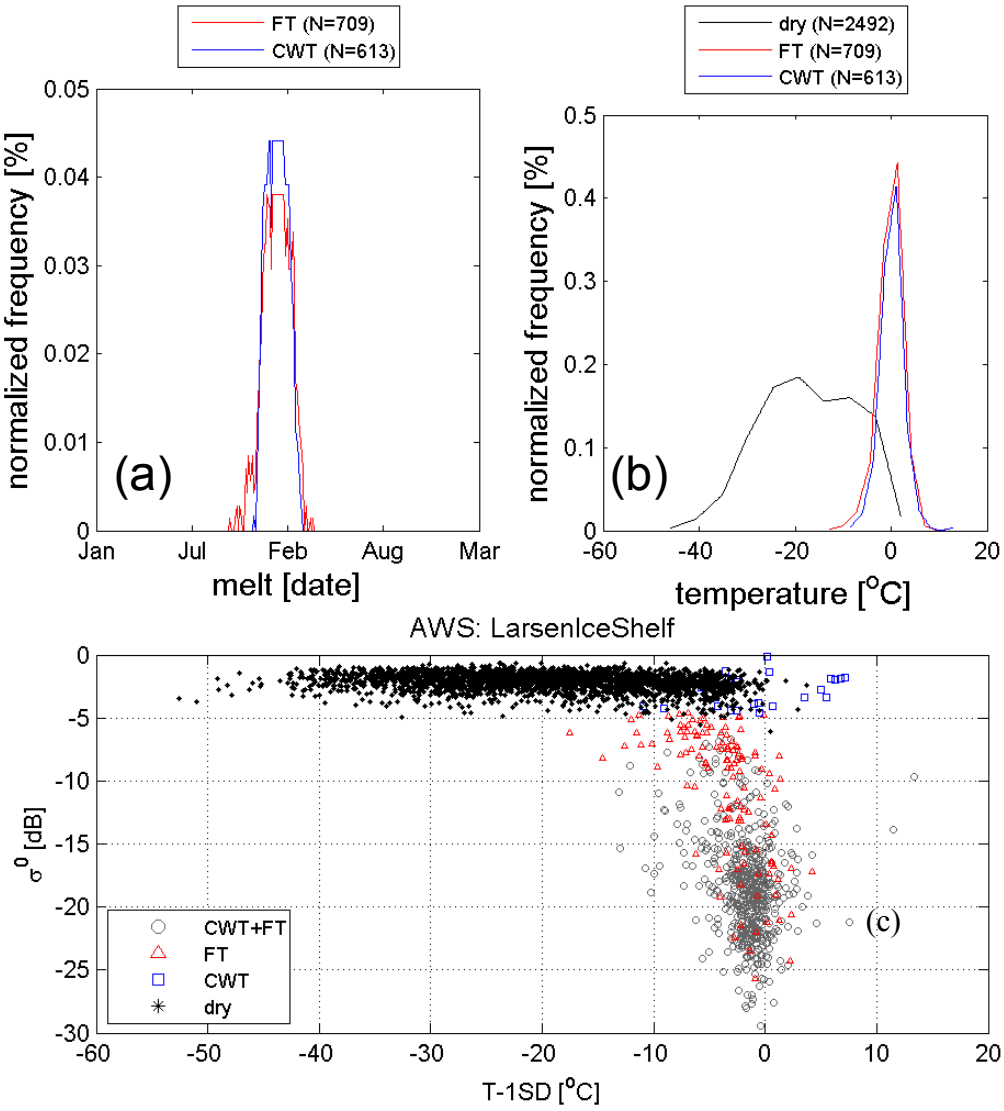

Figure A-7 (a) The frequency of DOY that is detected as melted determined by the CWT and FT3 method. (b) Observed temperature at the time of melt detection from the CWT and FT3 method. (c) Observed temperature during QuikSCAT observation is colored based on the classification by the CWT and FT3 algorithm. This data is for the Larsen Ice Shelf AWS from 1999-2009.

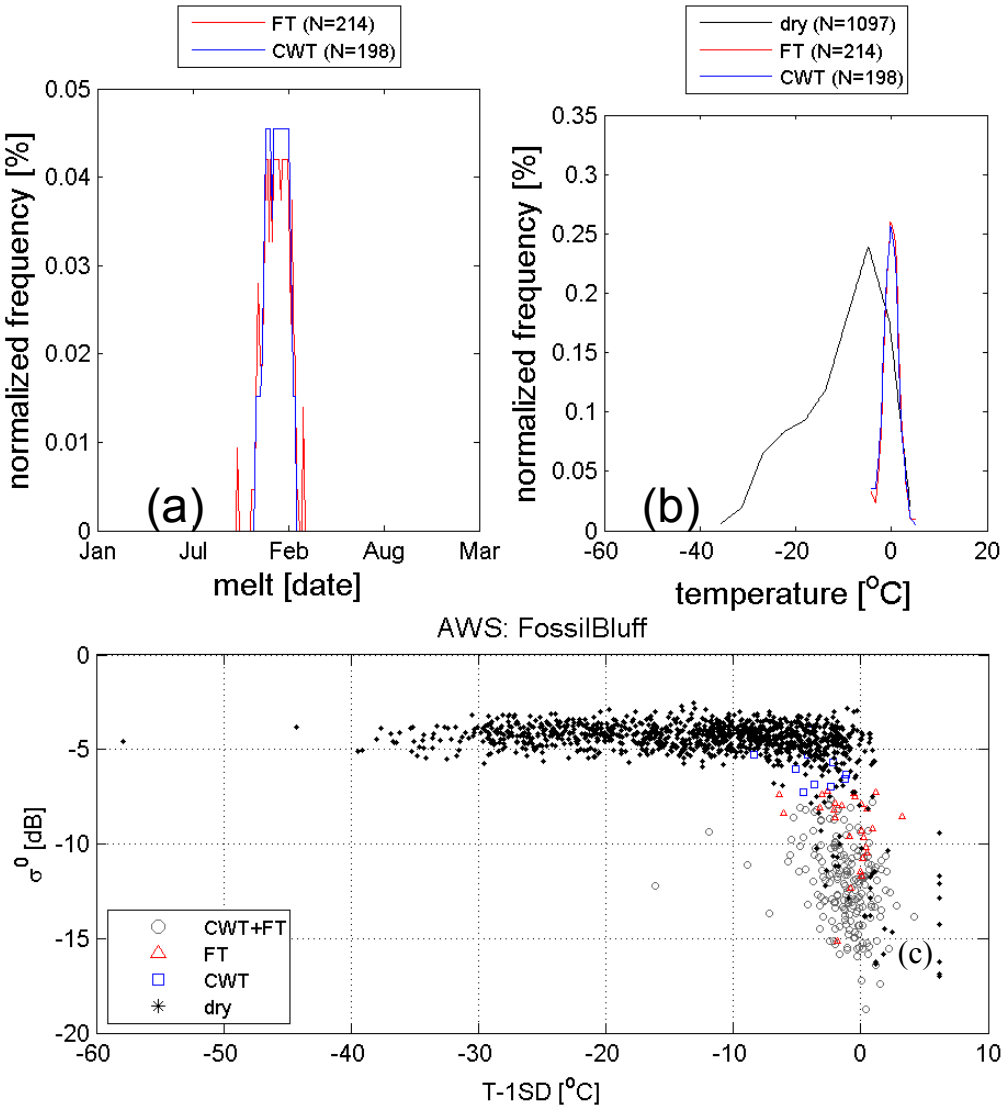

Figure A-8(a) The frequency of DOY that is detected as melted determined by the CWT and FT3 method. (b) Observed temperature at the time of melt detection from the CWT and FT3 method. (c) Observed temperature during QuikSCAT observation is colored based on the classification by the CWT and FT3 algorithm. This data is for the Fossil Bluff AWS from 2007-2009.

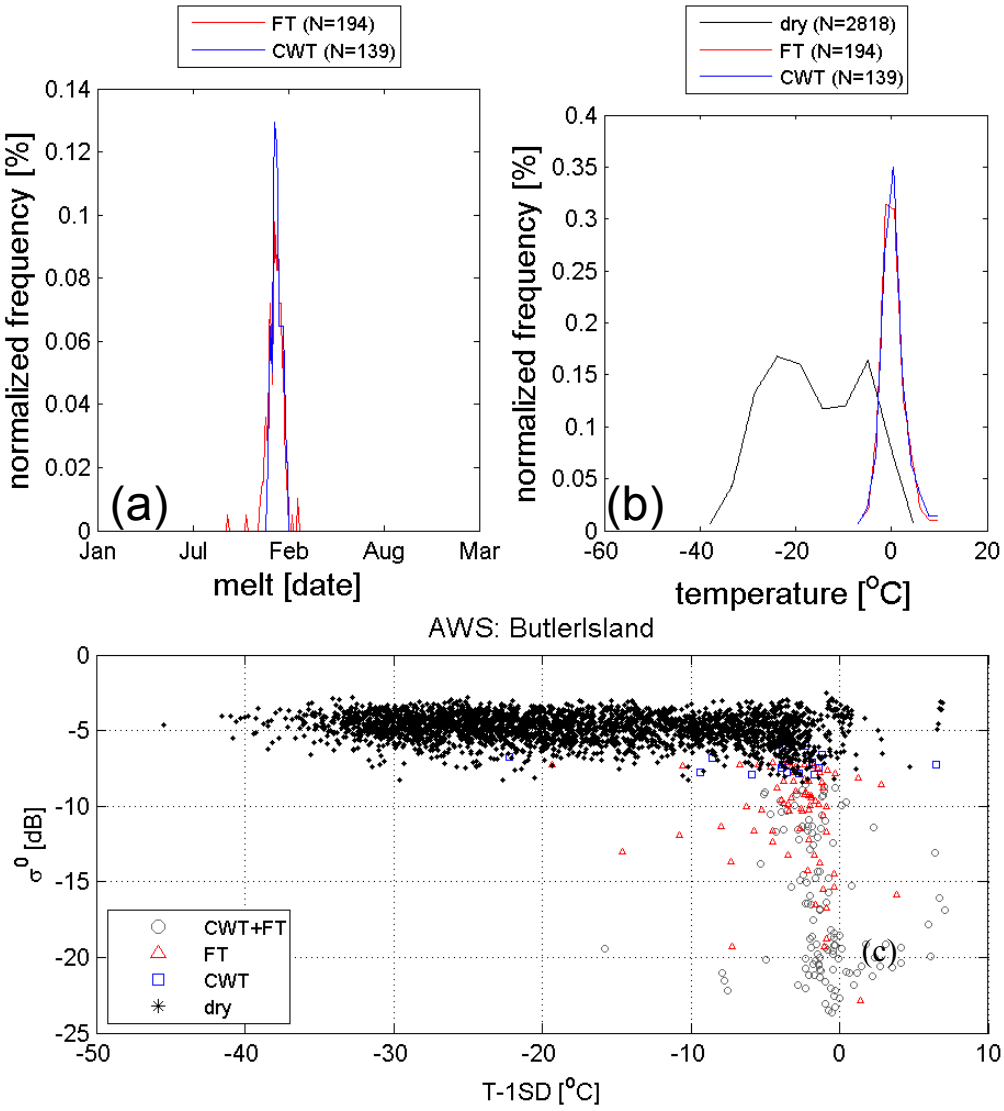

Figure A-9 (a) The frequency of DOY that is detected as melted determined by the CWT and FT3 method. (b) Observed temperature at the time of melt detection from the CWT and FT3 method. (c) Observed temperature during QuikSCAT observation is colored based on the classification by the CWT and FT3 algorithm. This data is for the Fossil Bluff AWS from 2007-2009.

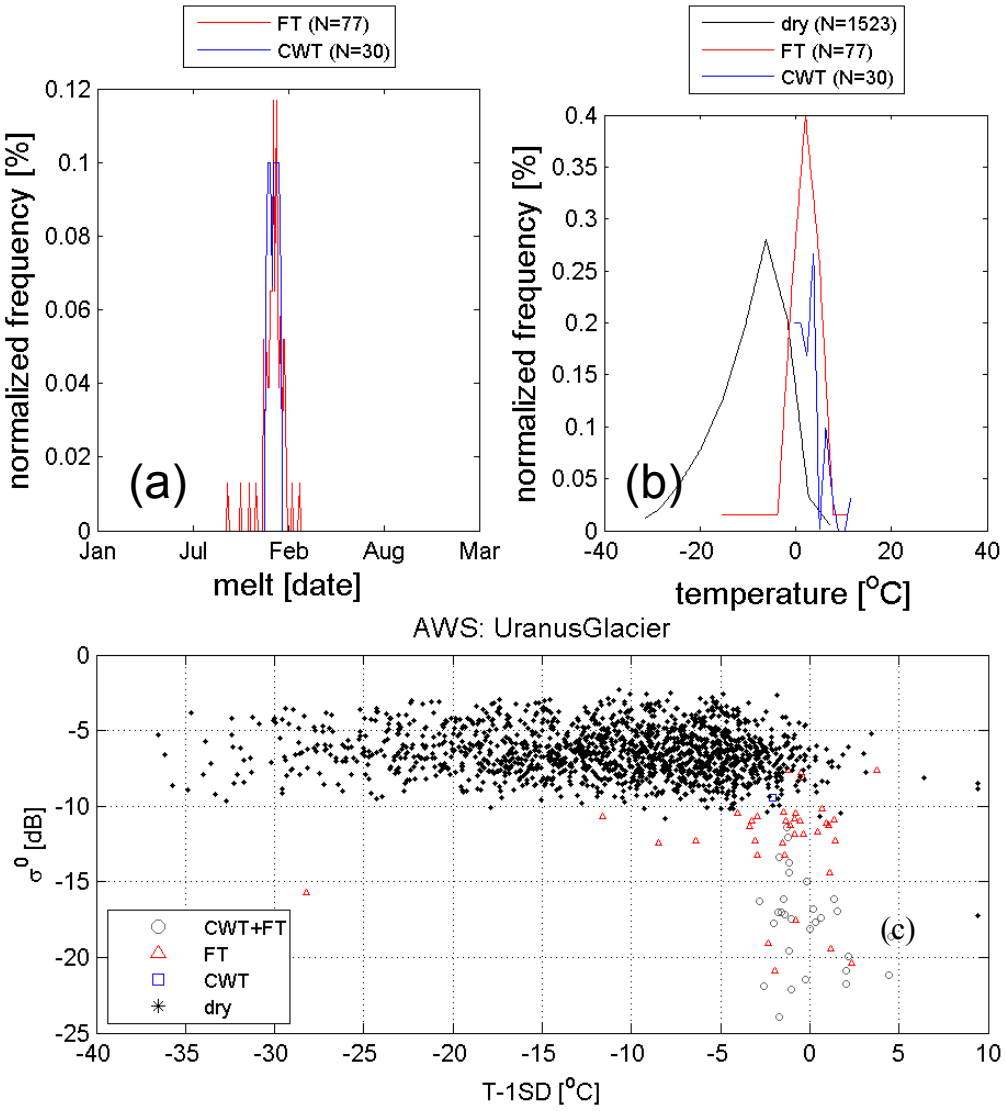

Figure A-10 (a) The frequency of DOY that is detected as melted determined by the CWT and FT3 method. (b) Observed temperature at the time of melt detection from the CWT and FT3 method. (c) Observed temperature during QuikSCAT observation is colored based on the classification by the CWT and FT3 algorithm. This data is for the Fossil Bluff AWS from 2000-2004.

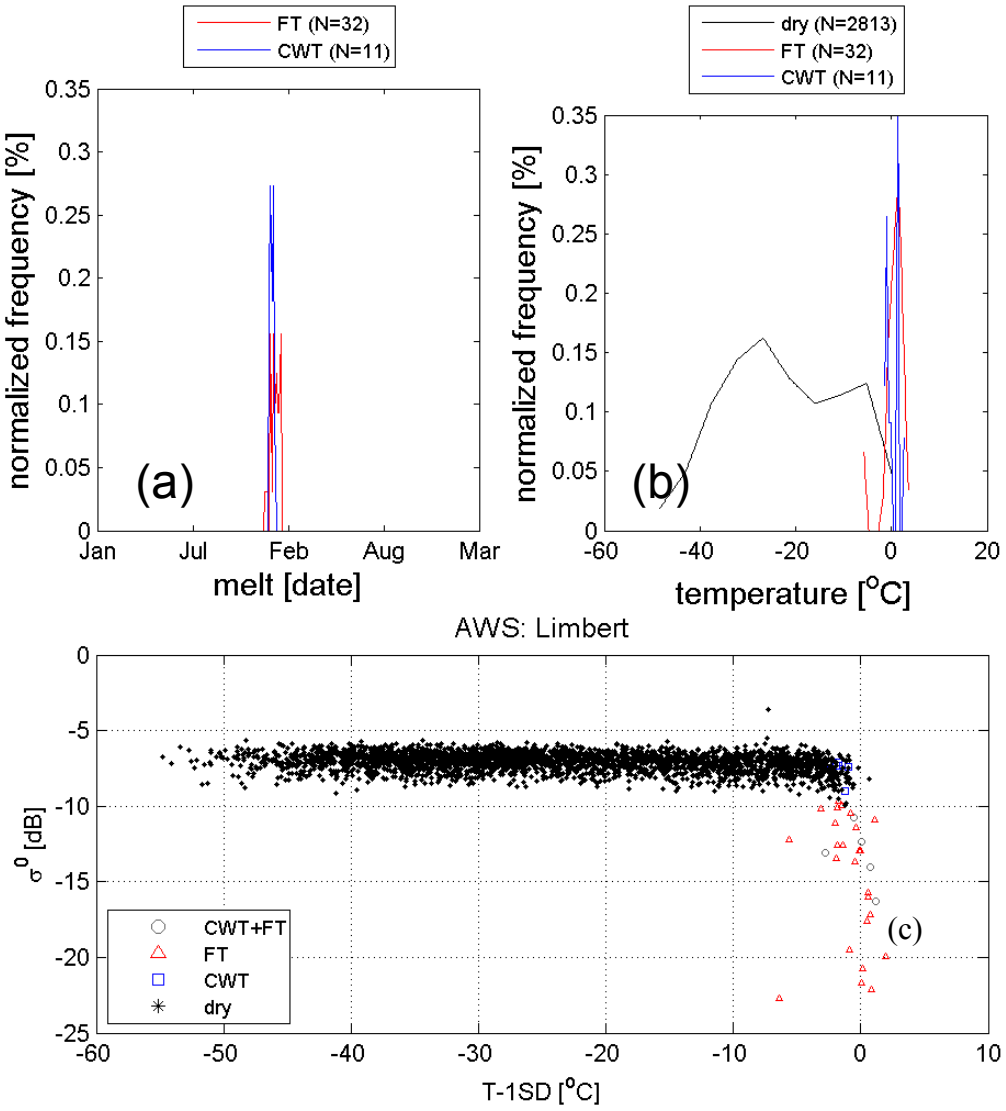

Figure A-11 (a) The frequency of DOY that is detected as melted determined by the CWT and FT3 method. (b) Observed temperature at the time of melt detection from the CWT and FT3 method. (c) Observed temperature during QuikSCAT observation is colored based on the classification by the CWT and FT3 algorithm. This data is for the Limbert AWS from 2005-2009.

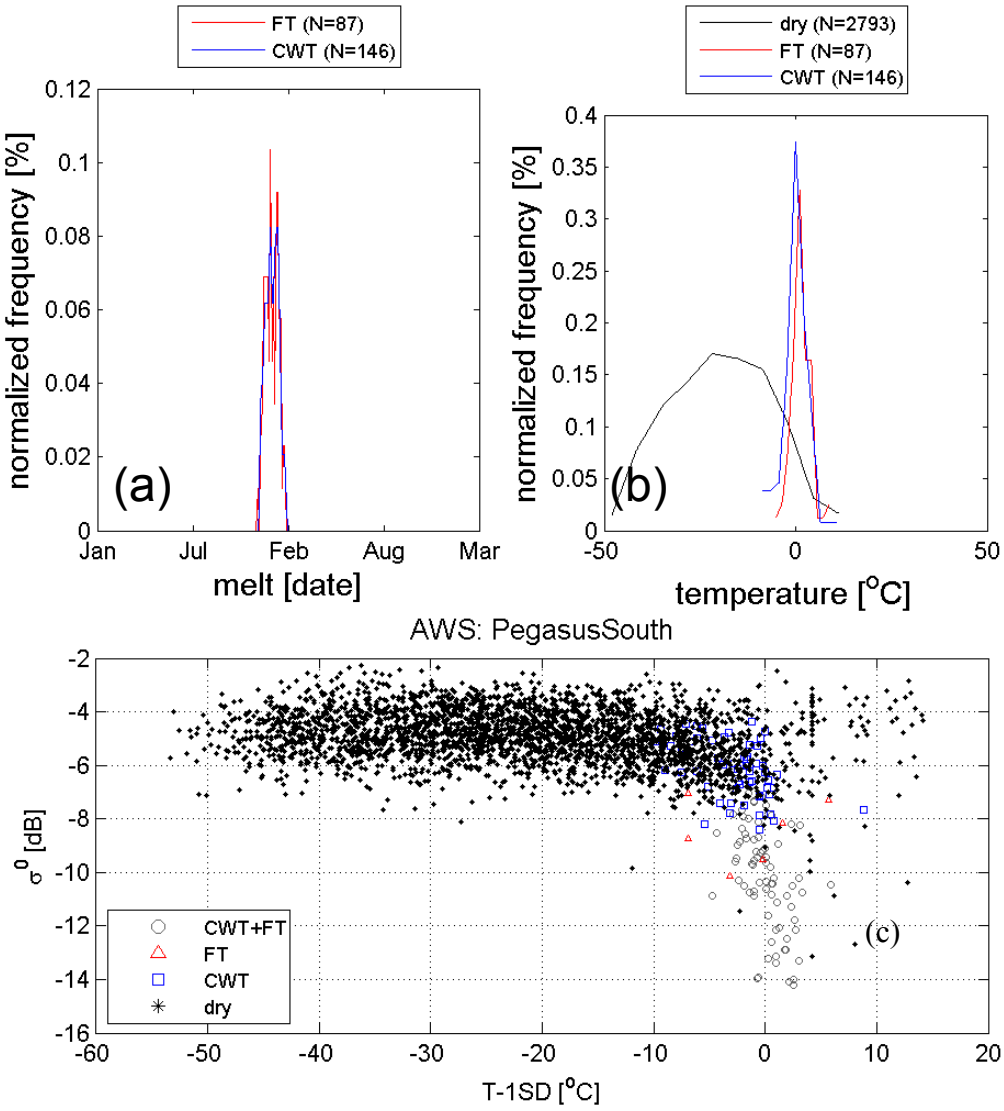

Figure A-12 (a) The frequency of DOY that is detected as melted determined by the CWT and FT3 method. (b) Observed temperature at the time of melt detection from the CWT and FT3 method. (c) Observed temperature during QuikSCAT observation is colored based on the classification by the CWT and FT3 algorithm. This data is for the Pegasus South AWS from 2000:2005.

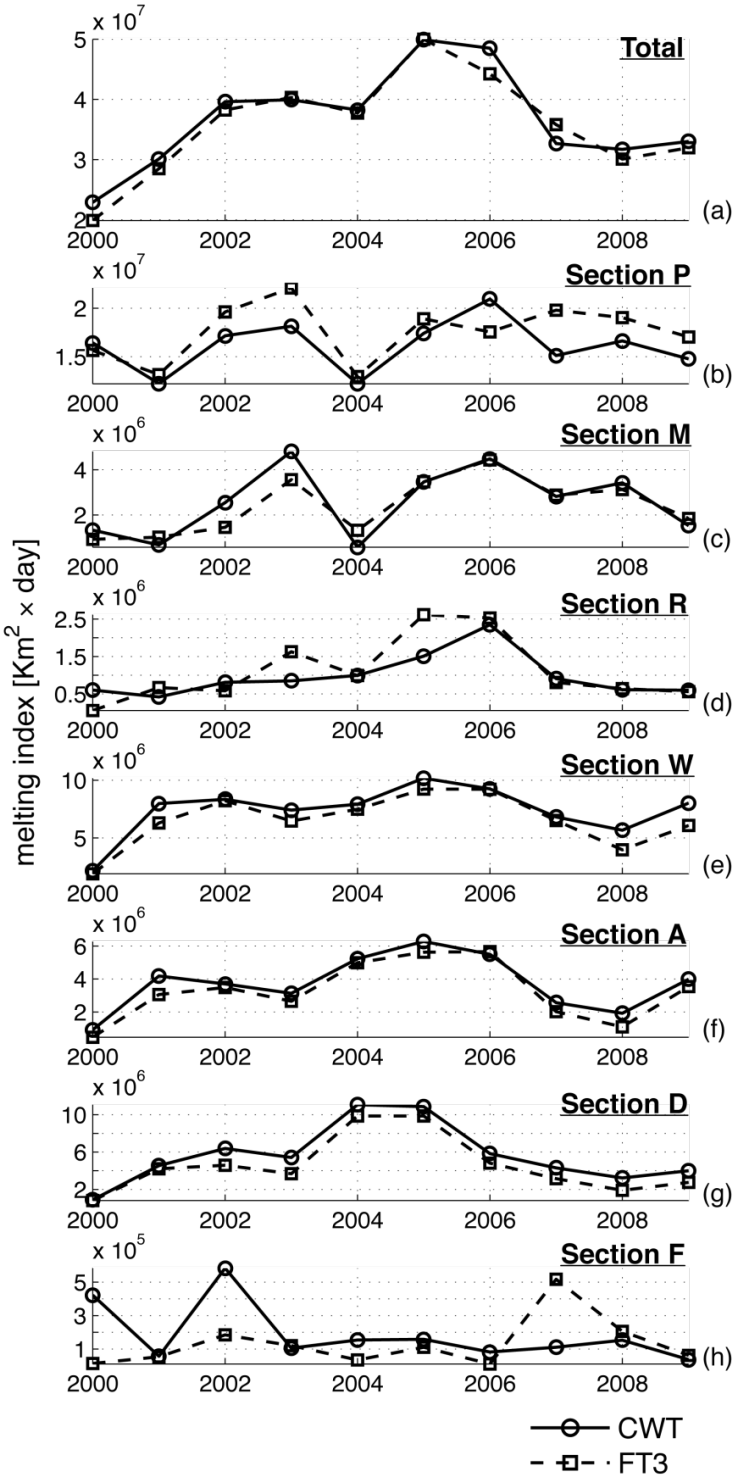

Figure A-13 Seasonal trends in melt index for regions defined in **Figure A-1**, for both the FT3 and CWT method.

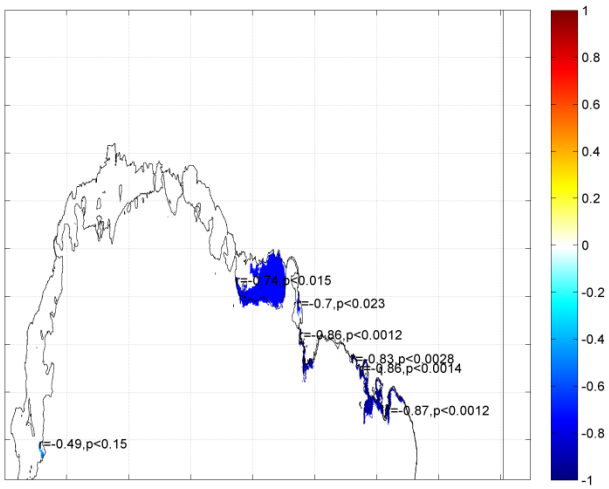

Figure A-14 Correlation between SAM (DecJanFeb) and regionally averaged MD for the CWT method over the Dronning Maude Land. Regression coefficients are labeled over areas of correlation

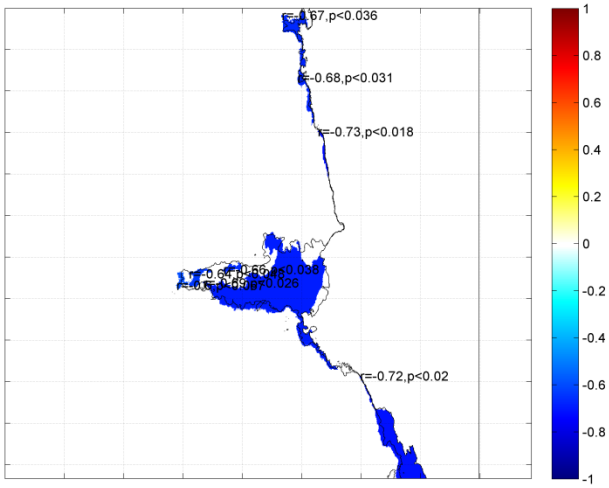

Figure A-15 Correlation between SAM (DecJanFeb) and regionally averaged MD for the CWT method for the Amery Ice Shelf. Regression coefficients are labeled over areas of correlation.

Table A-1 Melting duration (MD), melt index (MI), melt onset (MO), melt off (MF) Season duration for regions of Antarctica.

	MD [day]				MI [days-km^2]			
Section	FT3	CWT	diff	%diff	FT3	CWT	diff	%diff
Amery Ice Shelf (A)	23	34	-11	39%	2.60E+06	3.10E+06	-4.90E+05	17%
Antarctica (Ant)	27	41	-14	40%	2.80E+07	3.00E+07	-1.60E+06	5%
Dronning-Maude Land (D)	16	28	-12	53%	4.20E+06	5.30E+06	-1.10E+06	24%
Fimbul Ice Shelf (F)	5	41	-36	157%	1.20E+05	1.80E+05	-5.60E+04	38%
Marie Byrd Land (M)	13	38	-25	96%	1.90E+06	2.20E+06	-2.70E+05	13%
Antarctic Peninsula (P)	50	55	-4	8%	1.50E+07	1.40E+07	1.20E+06	8%
Ross Ice Shelf (R)	6	36	-30	142%	5.00E+05	4.50E+05	5.20E+04	11%
Wilkes Land (W)	23	37	-14	46%	3.80E+06	4.70E+06	-8.50E+05	20%

	MO [DOY*]						MF [DOY*]					
Section	FT3	CWT	diff	z-score	s_{FT3}	s_{CWT}	FT3	CWT	diff	z-score	s_{FT3}	s_{CWT}
Amery Ice Shelf (A)	357	349	7	0.7	12	9	385	384	1	0.08	14	17
Antarctica (Ant)	352	347	5	0.24	26	16	393	390	2	0.09	28	25
Dronning-Maude Land (D)	360	352	8	0.7	12	10	381	385	-3	-0.2	13	22
Fimbul Ice Shelf (F)	378	340	38	1.91	11	29	384	411	-27	-0.88	10	51
Marie Byrd Land (M)	358	348	10	0.34	30	27	389	400	-11	-0.28	36	39
Antarctic Peninsula (P)	336	342	-7	-0.31	28	15	411	398	14	0.55	28	22
Ross Ice Shelf (R)	371	340	30	1.53	16	23	382	387	-4	-0.17	17	32
Wilkes Land (W)	356	348	8	0.55	18	11	388	385	3	0.16	20	16

	Season** [day]				[MD/season]		
Section	FT3	CWT	diff	%diff	FT3	CWT	diff
Amery Ice Shelf (A)	28	34	-6	19%	80%	97%	20%
Antarctica (Ant)	41	43	-2	6%	67%	95%	34%
Dronning-Maude Land (D)	21	32	-11	42%	77%	86%	11%
Fimbul Ice Shelf (F)	6	71	-65	167%	77%	58%	29%
Marie Byrd Land (M)	31	51	-20	49%	43%	75%	54%
Antarctic Peninsula (P)	76	55	20	31%	66%	99%	39%
Ross Ice Shelf (R)	12	46	-35	119%	51%	77%	41%
Wilkes Land (W)	32	37	-5	14%	72%	99%	32%

* Here DOY refers to days after January, 1 for the first year in the melting season

** The melting season is defined as MF-MO

***Difference refers to FT3-CWT

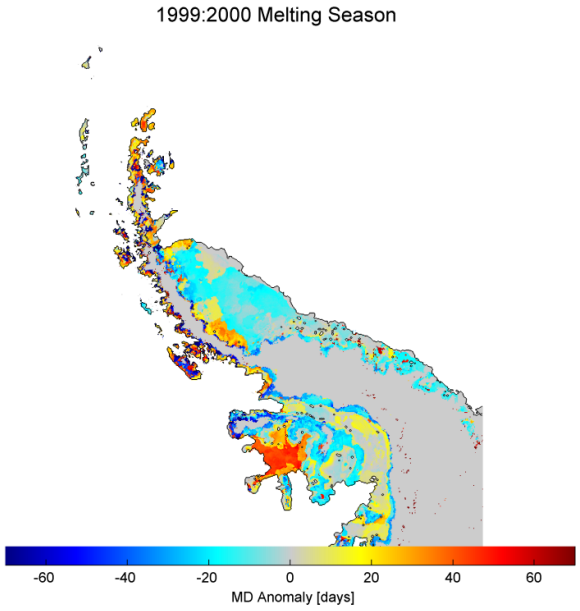

Figure A-16 QuikSCAT derived melting anomalies for the 1999-2000 season (from 1999 through 2009 mean) over the Antarctic Peninsula as determined by the CWT melt detection method

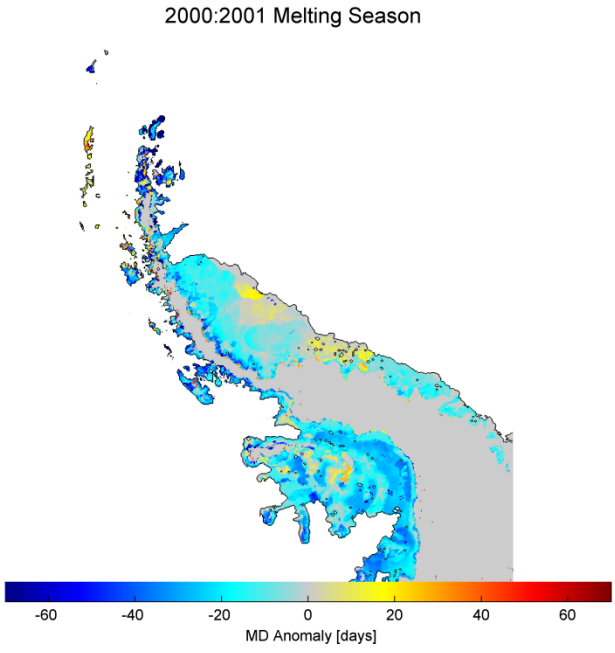

Figure A-17 Same as previous figure for the 2000-2001 melting season

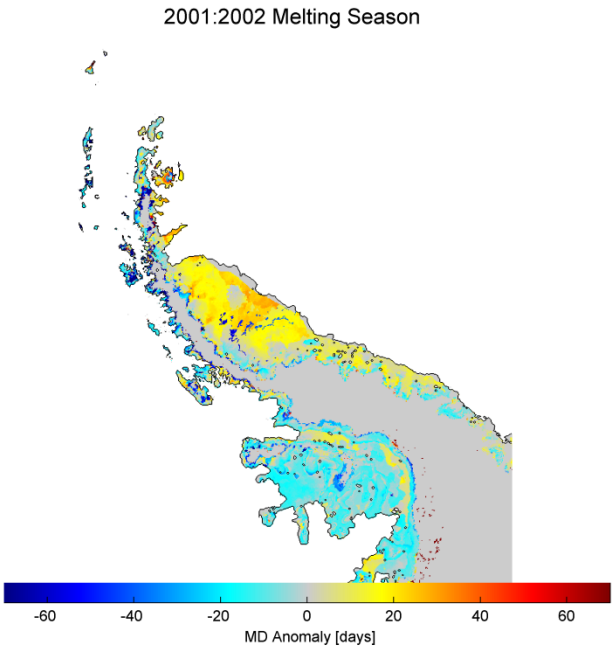

Figure A-18 Same as previous figure for the 2001-2002 melting season

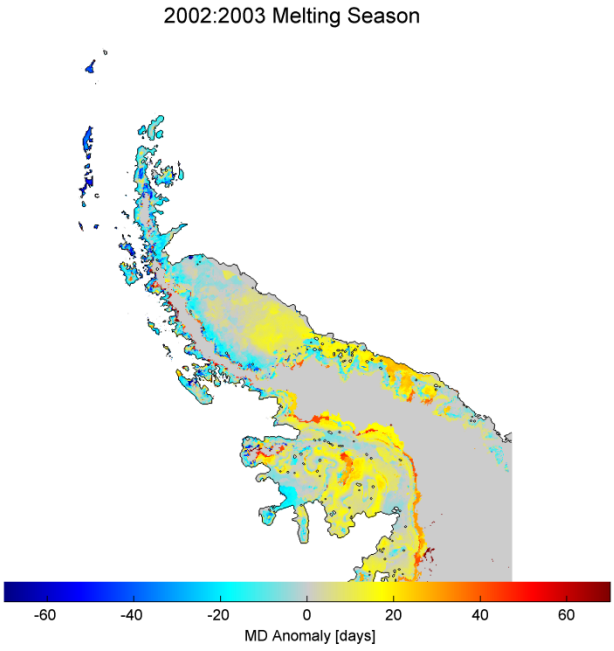

Figure A-19 Same as previous figure for the 2002-2003 melting season

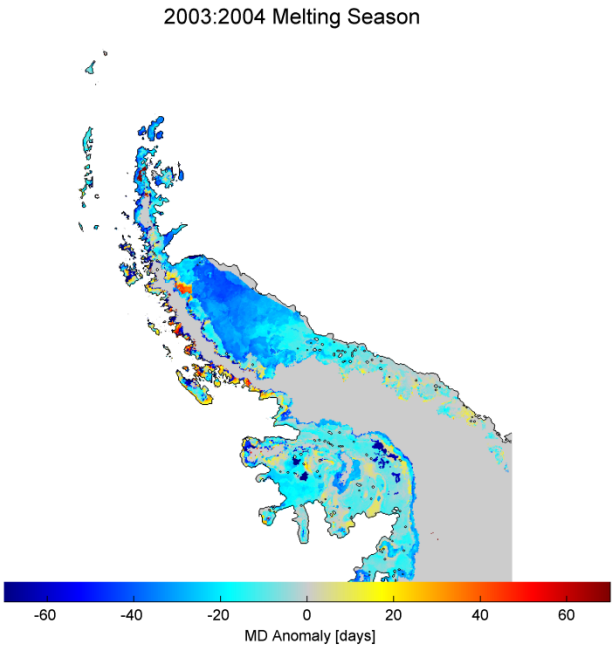

Figure A-20 Same as previous figure for the 2003-2004 melting season

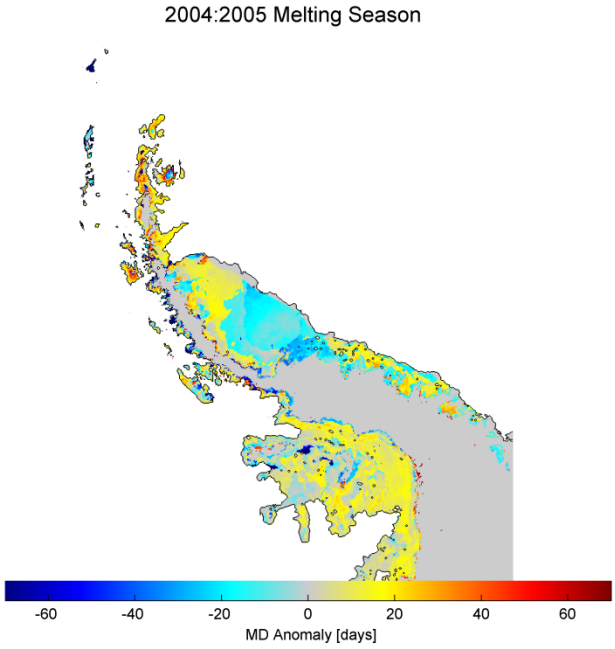

Figure A-21 Same as previous figure for the 2004-2005 melting season

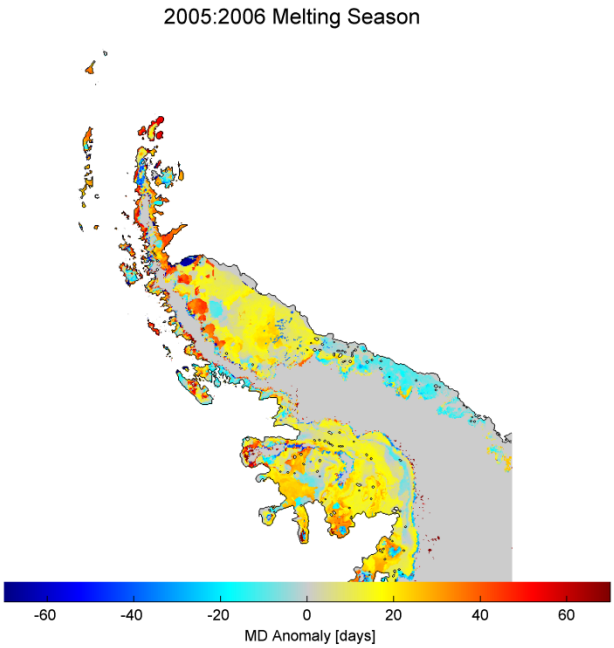

Figure A-22 Same as previous figure for the 2005-2006 melting season

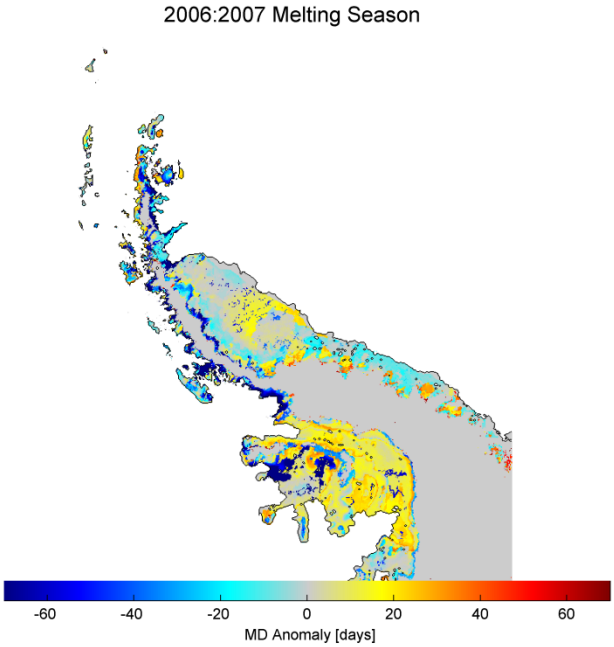

Figure A-23 Same as previous figure for the 2006-2007 melting season

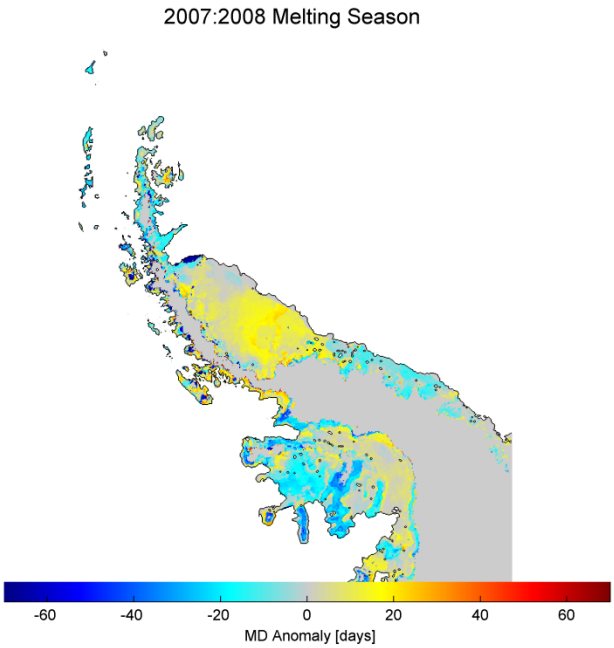

Figure A-24 Same as previous figure for the 2007-2008 melting season

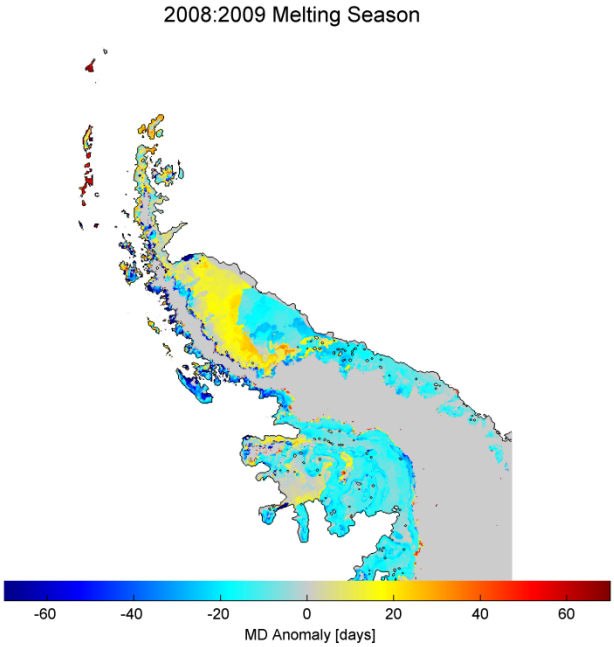

Figure A-25 Same as previous figure for the 2008-2009 melting season

Table A-2 Yearly and mean melt duration and melt index for the regions outlined in **Figure A-1**

		MD				MI			
year	section	FT3	CWT	diff	%diff	FT3	CWT	diff	%diff
1999	A	7	29	-23	-123.8%	1.95E+05	6.55E+05	-4.60E+05	-108.2%
2000	A	22	38	-16	-52.6%	2.29E+06	3.32E+06	-1.03E+06	-36.6%
2001	A	22	28	-7	-26.5%	2.72E+06	3.10E+06	-3.86E+05	-13.3%
2002	A	19	26	-7	-32.4%	2.05E+06	2.55E+06	-5.00E+05	-21.7%
2003	A	32	38	-6	-17.2%	4.32E+06	4.64E+06	-3.17E+05	-7.1%
2004	A	38	45	-7	-16.5%	4.89E+06	5.56E+06	-6.78E+05	-13.0%
2005	A	35	37	-2	-6.2%	4.91E+06	4.84E+06	7.01E+04	1.4%
2006	A	16	33	-18	-71.3%	1.41E+06	1.92E+06	-5.04E+05	-30.3%
2007	A	14	30	-16	-74.1%	6.33E+05	1.42E+06	-7.83E+05	-76.4%
2008	A	22	31	-8	-31.9%	2.78E+06	3.10E+06	-3.16E+05	-10.7%
mean	A	23	34	-11	-38.9%	2.62E+06	3.11E+06	-4.90E+05	-17.1%
1999	Ant	28	51	-23	-58.8%	1.56E+07	1.89E+07	-3.26E+06	-18.9%
2000	Ant	25	38	-13	-41.9%	2.21E+07	2.38E+07	-1.71E+06	-7.4%
2001	Ant	28	37	-9	-26.3%	2.96E+07	3.17E+07	-2.11E+06	-6.9%
2002	Ant	28	41	-13	-37.3%	3.17E+07	3.25E+07	-8.23E+05	-2.6%
2003	Ant	26	39	-12	-38.1%	3.02E+07	3.18E+07	-1.56E+06	-5.0%
2004	Ant	28	42	-14	-41.3%	4.05E+07	4.14E+07	-8.87E+05	-2.2%
2005	Ant	29	41	-12	-33.9%	3.56E+07	3.95E+07	-3.95E+06	-10.5%
2006	Ant	27	42	-15	-44.8%	2.79E+07	2.64E+07	1.58E+06	5.8%
2007	Ant	28	40	-12	-35.3%	2.37E+07	2.55E+07	-1.84E+06	-7.5%
2008	Ant	26	37	-12	-37.6%	2.44E+07	2.57E+07	-1.25E+06	-5.0%
mean	Ant	27	41	-14	-39.9%	2.81E+07	2.97E+07	-1.58E+06	-5.5%
1999	D	6	22	-16	-110.3%	6.46E+05	7.71E+05	-1.25E+05	-17.6%
2000	D	16	24	-8	-38.5%	3.78E+06	4.17E+06	-3.89E+05	-9.8%
2001	D	15	26	-11	-52.0%	4.18E+06	6.08E+06	-1.90E+06	-37.1%
2002	D	15	32	-16	-69.8%	3.29E+06	5.08E+06	-1.79E+06	-42.7%

2003	D	25	37	-12	-38.1%	9.41E+06	1.07E+07	-1.25E+06	-12.4%
2004	D	29	33	-4	-13.8%	9.37E+06	1.04E+07	-1.02E+06	-10.4%
2005	D	17	25	-7	-33.8%	4.33E+06	5.40E+06	-1.07E+06	-22.0%
2006	D	15	29	-14	-62.8%	2.84E+06	4.06E+06	-1.22E+06	-35.4%
2007	D	13	26	-14	-70.9%	1.67E+06	3.04E+06	-1.37E+06	-58.1%
2008	D	11	26	-15	-80.8%	2.35E+06	3.60E+06	-1.25E+06	-42.0%
mean	D	16	28	-12	-52.5%	4.19E+06	5.32E+06	-1.14E+06	-23.9%
1999	F	5	131	-126	-184.6%	3.23E+02	4.21E+05	-4.20E+05	-199.7%
2000	F	7	38	-32	-140.9%	2.76E+04	5.30E+04	-2.54E+04	-63.2%
2001	F	5	15	-11	-107.4%	1.63E+05	5.53E+05	-3.89E+05	-108.7%
2002	F	4	32	-29	-157.7%	9.82E+04	8.46E+04	1.36E+04	14.9%
2003	F	10	35	-26	-114.5%	3.16E+04	1.46E+05	-1.15E+05	-128.9%
2004	F	4	34	-30	-158.2%	1.06E+05	1.42E+05	-3.59E+04	-29.0%
2005	F	5	33	-28	-145.9%	9.94E+03	8.13E+04	-7.13E+04	-156.4%
2006	F	4	43	-40	-169.2%	5.05E+05	1.01E+05	4.05E+05	133.6%
2007	F	3	22	-19	-146.3%	1.99E+05	1.51E+05	4.74E+04	27.1%
2008	F	4	29	-25	-153.8%	5.90E+04	2.82E+04	3.08E+04	70.6%
mean	F	5	41	-36	-157.0%	1.20E+05	1.76E+05	-5.60E+04	-37.9%
1999	M	10	65	-55	-147.1%	7.18E+05	1.17E+06	-4.48E+05	-47.6%
2000	M	8	41	-33	-135.3%	7.73E+05	5.56E+05	2.18E+05	32.8%
2001	M	12	43	-31	-114.9%	1.00E+06	2.09E+06	-1.09E+06	-70.7%
2002	M	20	46	-27	-80.4%	2.85E+06	4.16E+06	-1.31E+06	-37.5%
2003	M	7	41	-34	-143.9%	9.56E+05	4.20E+05	5.37E+05	78.0%
2004	M	15	33	-18	-73.0%	2.83E+06	2.91E+06	-8.18E+04	-2.9%
2005	M	21	34	-13	-48.4%	3.73E+06	3.91E+06	-1.84E+05	-4.8%
2006	M	16	33	-17	-68.9%	2.27E+06	2.30E+06	-2.92E+04	-1.3%
2007	M	15	29	-14	-64.6%	2.58E+06	3.00E+06	-4.19E+05	-15.0%
2008	M	12	20	-8	-51.7%	1.29E+06	1.19E+06	9.66E+04	7.8%
mean	M	13	38	-25	-96.3%	1.90E+06	2.17E+06	-2.72E+05	-13.4%

1999	P	49	61	-12	-21.0%	1.33E+07	1.40E+07	-7.74E+05	-5.7%
2000	P	38	42	-4	-10.3%	1.14E+07	1.05E+07	8.91E+05	8.2%
2001	P	54	56	-1	-2.7%	1.63E+07	1.42E+07	2.18E+06	14.3%
2002	P	58	53	5	8.7%	1.89E+07	1.56E+07	3.24E+06	18.8%
2003	P	37	43	-6	-15.4%	1.06E+07	1.02E+07	3.74E+05	3.6%
2004	P	53	60	-8	-13.5%	1.58E+07	1.50E+07	8.65E+05	5.6%
2005	P	54	68	-13	-22.1%	1.54E+07	1.77E+07	-2.31E+06	-13.9%
2006	P	55	58	-3	-5.2%	1.70E+07	1.35E+07	3.47E+06	22.7%
2007	P	55	55	-1	-1.3%	1.63E+07	1.41E+07	2.14E+06	14.1%
2008	P	49	50	-1	-2.1%	1.43E+07	1.26E+07	1.76E+06	13.1%
mean	P	50	55	-4	-8.4%	1.49E+07	1.37E+07	1.18E+06	8.3%
1999	R	7	89	-82	-170.8%	1.19E+04	5.39E+05	-5.27E+05	-191.4%
2000	R	4	59	-56	-177.5%	4.00E+04	4.97E+04	-9.65E+03	-21.5%
2001	R	5	27	-22	-140.0%	6.94E+04	2.47E+05	-1.77E+05	-112.1%
2002	R	6	31	-25	-136.1%	8.21E+05	4.61E+05	3.59E+05	56.1%
2003	R	6	28	-21	-125.2%	3.12E+05	3.85E+05	-7.28E+04	-20.9%
2004	R	6	14	-8	-79.6%	1.92E+06	6.88E+05	1.23E+06	94.5%
2005	R	9	25	-16	-92.7%	1.41E+06	1.46E+06	-5.04E+04	-3.5%
2006	R	7	27	-20	-120.1%	1.88E+05	2.90E+05	-1.02E+05	-42.7%
2007	R	6	18	-12	-101.3%	1.66E+05	1.78E+05	-1.21E+04	-7.0%
2008	R	5	39	-35	-155.7%	9.66E+04	2.19E+05	-1.22E+05	-77.4%
mean	R	6	36	-30	-142.4%	5.04E+05	4.52E+05	5.20E+04	10.9%
1999	W	9	22	-14	-86.7%	7.58E+05	1.16E+06	-3.99E+05	-41.7%
2000	W	27	52	-25	-64.0%	3.78E+06	5.14E+06	-1.36E+06	-30.5%
2001	W	25	33	-9	-29.5%	5.07E+06	5.40E+06	-3.29E+05	-6.3%
2002	W	22	36	-13	-45.3%	3.71E+06	4.53E+06	-8.28E+05	-20.1%
2003	W	29	37	-8	-23.8%	4.54E+06	5.25E+06	-7.14E+05	-14.6%
2004	W	31	43	-13	-34.3%	5.50E+06	6.73E+06	-1.23E+06	-20.1%
2005	W	28	36	-8	-24.6%	5.79E+06	6.08E+06	-2.90E+05	-4.9%

2006	W	24	38	-14	-44.5%	3.70E+06	4.16E+06	-4.58E+05	-11.7%
2007	W	17	34	-16	-63.7%	2.10E+06	3.54E+06	-1.45E+06	-51.3%
2008	W	21	39	-18	-61.0%	3.46E+06	4.93E+06	-1.48E+06	-35.2%
mean	W	23	37	-14	-45.5%	3.84E+06	4.69E+06	-8.53E+05	-20.0%

Table A-3 Yearly and mean melt onset (MO) and melt off (MF) for Antarctica (Ant) and the regions outlined in **Figure A-1**.

		MO						MF						Season			
year	section	FT3	CWT	diff	z-score	s_FT3	s_CWT	FT3	CWT	diff	z-score	s_FT3	s_CWT	FT3	CWT	diff	%diff
1999	A	371	307	63	4.58	15	13	381	336	45	2.92	14.2	16.6	10	28	-19	-96.3%
2000	A	356	351	5	0.27	17	16	384	388	-4	-0.33	13.0	10.3	28	37	-8	-25.6%
2001	A	360	359	1	0.13	10	9	385	386	0	-0.09	6.5	4.6	25	27	-2	-6.6%
2002	A	362	364	-2	-0.21	8	7	389	389	-1	-0.04	13.2	10.5	26	25	1	4.3%
2003	A	350	351	-1	-0.13	8	8	386	389	-2	-0.20	13.0	10.4	36	37	-1	-3.5%
2004	A	347	347	0	0.07	8	7	388	390	-2	-0.23	12.5	8.2	41	44	-3	-6.9%
2005	A	344	346	-2	-0.34	7	7	382	383	0	-0.02	13.4	10.4	38	36	2	5.4%
2006	A	365	359	6	0.36	19	14	390	391	-1	-0.06	19.1	7.8	25	32	-7	-24.2%
2007	A	357	353	4	0.38	13	6	376	382	-6	-0.41	16.7	11.8	19	29	-10	-39.6%
2008	A	354	355	-1	-0.13	11	7	388	384	4	0.23	20.1	12.7	35	30	5	15.4%
mean	A	357	349	7	0.70	12	9	385	382	3	0.26	14.2	10.3	28	32	-4	-13.5%
1999	Ant	351	292	59	2.19	31	22	400	343	57	1.88	33.8	27.1	49	50	-2	-3.2%
2000	Ant	350	354	-3	-0.16	26	17	392	391	2	0.08	25.3	13.1	42	37	5	12.5%
2001	Ant	356	356	0	0.02	20	12	392	392	0	0.00	21.5	15.0	36	36	0	-0.6%
2002	Ant	355	353	2	0.12	23	14	396	393	2	0.11	28.3	15.2	41	40	0	0.6%
2003	Ant	352	354	-1	-0.09	20	13	389	391	-2	-0.08	31.4	16.7	37	37	0	-1.3%
2004	Ant	351	348	3	0.14	25	13	388	390	-2	-0.11	20.0	13.8	37	41	-4	-11.5%
2005	Ant	346	351	-6	-0.27	26	17	392	392	0	-0.01	29.8	20.5	46	41	5	12.5%
2006	Ant	351	355	-4	-0.15	38	20	395	396	-1	-0.10	19.2	9.7	44	41	3	7.0%
2007	Ant	355	352	3	0.17	27	10	393	391	2	0.08	38.1	18.7	38	39	-1	-2.0%
2008	Ant	351	354	-3	-0.14	21	16	389	390	-2	-0.08	28.9	15.7	38	37	1	2.7%
mean	Ant	352	347	5	0.24	26	16	393	387	6	0.26	27.6	16.6	41	40	1	1.7%
1999	D	373	312	61	3.84	13	19	381	333	48	3.75	11.0	14.5	8	21	-13	-87.8%
2000	D	362	362	1	0.04	11	12	381	384	-3	-0.37	9.6	9.0	19	23	-4	-19.1%
2001	D	361	359	2	0.30	9	7	382	384	-2	-0.26	8.2	4.6	21	25	-4	-17.9%
2002	D	359	356	2	0.24	11	9	381	387	-6	-0.39	15.5	12.8	23	31	-8	-30.2%
2003	D	355	352	3	0.45	7	6	384	388	-5	-0.44	11.9	8.9	28	36	-7	-23.3%
2004	D	354	354	0	0.02	8	6	386	386	1	0.07	10.2	8.3	32	32	0	1.4%
2005	D	357	356	0	0.04	13	11	378	379	-1	-0.10	13.4	9.0	22	23	-2	-7.1%
2006	D	367	364	3	0.28	14	11	387	392	-5	-0.41	14.4	7.5	20	28	-8	-32.9%
2007	D	355	352	4	0.24	18	12	375	379	-3	-0.23	20.0	8.3	20	27	-7	-29.2%
2008	D	358	358	0	0.02	13	9	376	382	-7	-0.44	17.4	13.0	18	25	-7	-31.9%
mean	D	360	352	8	0.70	12	10	381	379	2	0.15	13.2	9.6	21	27	-6	-24.6%
1999	F	492	242	249	6.37	34	44	505	373	132	3.33	33.7	45.8	14	131	-117	-161.9%
2000	F	366	351	15	0.48	20	40	378	382	-5	-0.20	19.0	28.2	12	31	-19	-89.1%
2001	F	370	363	7	0.78	4	14	374	377	-3	-0.54	5.1	7.2	4	14	-10	-114.8%
2002	F	363	369	-5	-0.25	3	38	367	384	-17	-1.28	4.4	22.6	3	16	-12	-127.3%
2003	F	360	344	16	1.07	5	25	373	379	-6	-0.47	6.4	18.9	13	35	-22	-92.9%
2004	F	374	345	29	1.40	5	37	378	384	-6	-0.59	2.5	18.9	4	39	-36	-164.8%
2005	F	356	340	15	0.90	5	29	363	375	-12	-1.18	1.2	19.7	7	35	-28	-134.7%
2006	F	379	339	40	2.11	4	34	382	382	-1	-0.08	4.1	13.9	3	43	-41	-177.0%
2007	F	362	351	12	1.10	8	13	365	373	-8	-0.75	7.6	12.5	3	22	-19	-158.3%
2008	F	356	351	5	0.27	17	19	359	376	-18	-0.74	17.2	30.7	3	25	-23	-160.5%

mean	F	378	340	38	1.91	11	29	384	379	6	0.35	10.1	21.8	6	39	-33	-143.4%
1999	M	355	278	78	2.42	35	29	395	342	53	1.21	48.4	39.1	40	64	-24	-47.2%
2000	M	364	345	19	0.53	34	37	386	391	-4	-0.14	32.4	27.3	23	46	-23	-66.9%
2001	M	371	355	16	0.76	20	22	394	398	-4	-0.16	31.0	23.9	23	43	-20	-61.8%
2002	M	356	352	4	0.15	24	23	392	398	-6	-0.23	28.7	20.9	36	45	-9	-22.8%
2003	M	345	362	-17	-0.37	32	61	367	380	-13	-0.31	48.2	37.0	22	18	4	20.1%
2004	M	359	355	4	0.24	22	16	386	388	-1	-0.08	24.3	7.8	27	33	-6	-19.4%
2005	M	355	359	-4	-0.13	39	25	403	396	7	0.25	35.2	21.4	48	37	11	26.2%
2006	M	357	365	-8	-0.35	24	25	394	398	-4	-0.29	18.7	8.2	37	32	5	13.1%
2007	M	358	354	4	0.14	46	9	385	383	2	0.07	52.0	13.4	27	29	-2	-6.4%
2008	M	360	359	1	0.03	24	21	389	382	7	0.28	38.1	14.2	29	23	7	25.4%
mean	M	358	348	10	0.34	30	27	389	385	4	0.13	35.7	21.3	31	37	-6	-17.1%
1999	P	333	287	45	2.20	27	15	414	348	67	2.30	29.6	28.1	81	60	21	29.9%
2000	P	335	353	-19	-0.87	28	15	405	394	11	0.49	31.7	14.2	71	41	30	54.2%
2001	P	343	351	-8	-0.39	26	14	411	406	5	0.23	23.0	15.7	67	55	12	20.2%
2002	P	340	347	-7	-0.46	19	11	417	400	17	0.76	31.5	14.4	77	52	24	37.4%
2003	P	354	357	-3	-0.13	28	10	414	399	15	0.55	32.8	22.4	60	42	18	34.7%
2004	P	322	336	-14	-0.64	33	11	403	396	8	0.33	26.7	19.5	81	59	22	30.9%
2005	P	326	348	-22	-0.82	31	22	420	415	5	0.21	31.6	17.9	94	67	27	33.2%
2006	P	315	344	-29	-0.84	48	21	406	402	4	0.35	14.9	7.7	90	57	33	44.4%
2007	P	347	348	-1	-0.10	20	9	417	403	14	0.50	34.5	21.0	70	54	15	24.8%
2008	P	341	351	-10	-0.46	23	20	406	400	6	0.31	23.3	16.1	65	49	16	28.1%
mean	P	336	342	-7	-0.31	28	15	411	396	15	0.66	28.0	17.7	76	54	22	33.7%
1999	R	417	238	179	4.03	49	40	463	326	137	3.11	50.3	37.8	46	89	-43	-63.1%
2000	R	377	316	60	2.66	5	40	379	373	6	0.38	5.2	25.9	3	57	-54	-182.7%
2001	R	366	356	10	1.02	4	17	371	382	-11	-1.79	4.2	8.4	4	26	-22	-145.9%
2002	R	376	356	20	0.64	35	28	390	388	2	0.15	22.5	7.4	14	32	-18	-77.4%
2003	R	339	334	5	0.34	12	17	350	361	-11	-0.68	16.8	15.9	11	27	-16	-85.9%
2004	R	371	367	4	0.55	2	12	376	380	-4	-0.85	3.2	6.0	5	13	-8	-86.7%
2005	R	355	352	2	0.46	3	7	368	376	-8	-0.97	9.7	7.0	13	24	-11	-57.4%
2006	R	378	369	10	0.55	12	24	387	391	-3	-0.27	15.1	10.2	9	22	-13	-85.4%
2007	R	377	367	10	0.71	5	24	383	384	-1	-0.13	9.6	7.8	6	17	-11	-101.9%
2008	R	349	347	2	0.06	34	25	356	381	-25	-0.89	36.3	18.8	8	34	-26	-127.3%
mean	R	371	340	30	1.53	16	23	382	374	8	0.51	17.3	14.5	12	34	-22	-97.1%
1999	W	370	309	61	3.39	21	15	385	331	54	2.79	26.2	12.7	15	21	-7	-35.8%
2000	W	351	345	7	0.41	20	13	393	396	-3	-0.31	11.6	8.7	41	51	-10	-21.4%
2001	W	357	356	1	0.09	14	9	387	389	-2	-0.19	15.0	7.5	29	32	-3	-10.0%
2002	W	356	354	2	0.12	19	12	390	388	2	0.10	22.3	11.5	34	35	0	-0.6%
2003	W	354	355	0	-0.03	14	11	391	391	0	0.03	16.9	12.4	37	36	1	2.1%
2004	W	350	349	1	0.12	11	8	387	391	-4	-0.21	21.0	14.6	37	42	-5	-12.2%
2005	W	347	348	-1	-0.09	12	9	380	383	-3	-0.26	13.8	9.0	33	35	-2	-6.2%
2006	W	358	356	2	0.11	24	15	398	392	6	0.30	26.2	11.0	40	37	4	9.4%
2007	W	360	355	5	0.40	19	8	386	388	-2	-0.14	19.1	8.5	25	33	-7	-24.8%
2008	W	354	352	2	0.09	22	12	385	390	-5	-0.27	28.7	8.2	31	38	-7	-19.1%
mean	W	356	348	8	0.55	18	11	388	384	4	0.28	20.1	10.4	32	36	-4	-10.6%

Bibliography

Addison, P. S. (2005). Wavelet transforms and the ECG: a review. *Physiological measurement*, 26, R155. pages R155-R189

Abdalati, W., & Steffen, K. (1997). Snowmelt on the Greenland ice sheet as derived from passive microwave satellite data. *Journal of Climate*, 10(2), 165-175.

Adler-Golden, S. M., M. W. Matthew, L. S. Bernstein, R. Y. Levine, A. Berk, S. C. Richtsmeier, P. K. Acharya, G. P. Anderson, G. Felde, J. Gardner, M. Hoke, L. S. Jeong, B. Pukall, A. Ratkowski, and H.-H Burke. (1999), Atmospheric Correction for Short-wave Spectral Imagery Based on MODTRAN4. *SPIE Proceedings on Imaging Spectrometry*, Vol. 3753, pp. 61-69

Alley, R. B., Clark, P. U., Huybrechts, P., & Joughin, I. (2005). Ice-sheet and sea-level changes. *Science*, 310(5747), 456-460. doi: 10.1126/science.1114613

Alexiades, V., and A.D. Solomon (1993), *Mathematical modeling of melting and freezing processes.* Washington DC, Hemisphere Publishing Corp.

Anisimov, O. A., Vaughan, T. V., Callaghan, C., Furgal, H., Marchant, T. D., Prowse, H., . . . Walsh, J. E. (2007). Polar regions (Arctic and Antarctic). Climate Change 2007: Impacts, Adaptation and Vulnerability. Contribution of Working Group II to the Fourth Assessment Report of the Intergovernmental Panel on Climate Change. In M. L. Parry, O. F. Canziani, J. P. Palutikof, P. J. van der Linden & C. E. Hanson (Eds.), (pp. 653-685). Cambridge, UK: Cambridge University Press.

Ashcraft, I. S., & Long, D. G. (2003). The spatial response function of SeaWinds backscatter measurements, *Proceedings SPIE The International Society for Optical Engineering* , ISSU 5151, pages 609-618

Ashcraft, I. S., & Long, D. G. (2006). Comparison of methods for melt detection over Greenland using active and passive microwave measurements. *International Journal of Remote Sensing*, 27(12), 2469-2488.

Bell, R. E. (2008). The role of subglacial water in ice-sheet mass balance. *Nature Geoscience*, 1(5), 297-304. doi: 10.1038/ngeo186

Box, J., Fettweis, X., Stroeve, J., Tedesco, M., Hall, D., & Steffen, K. (2012). Greenland ice sheet albedo feedback: thermodynamics and atmospheric drivers. *The Cryosphere Discuss*, 6, 593-634.

Box, J. E. and K. Ski (2007), Remote sounding of Greenland supra-glacial melt lakes (), implications to sub-glacial hydraulics, *J. Glaciol.,* 181, 257 – 265*,* 2007.

Bromwich, D. H., & Nicolas, J. P. (2010). Sea-level rise: Ice-sheet uncertainty. *Nature Geoscience*, 3(9), 596-597.

Chander, G., B. L. Markham and D. L. Helder (2009), Summary of current radiometric calibration coefficients for Landsat MSS, TM, ETM+, and EO-1 ALI sensors, *Remote Sensing of Environment* 113, 893–903.

Chen, J., Wilson, C., Blankenship, D., & Tapley, B. (2009). Accelerated Antarctic ice loss from satellite gravity measurements. *Nature Geoscience*, 2(12), 859-862.

Comiso, J. C. (2010). Polar oceans from space. New York: Springer.

Das, S. B., I. Joughin, M.D. Behn, I.M. Howat, M.A. King, D. Lizarralde and M.P. Bhatia (2008), Fracture propagation to the base of the Greenland ice sheet during supraglacial lake drainage, *Science*, 320, 778-781,.

Domack, E., Duran, D., Leventer, A., Ishman, S., Doane, S., McCallum, S., . . . Prentice, M. (2005). Stability of the Larsen B ice shelf on the Antarctic Peninsula during the Holocene epoch. Nature, 436(7051), 681-685.

Dowdeswell, J. A. (2006). The Greenland ice sheet and global sea-level rise. *Science*, 311(5763), 963.

Dupont, T. K., & Alley, R. B. (2006). Role of small ice shelves in sea-level rise. Geophysical Research Letters, 33(9). doi: L09503 10.1029/2005gl025665

Early, D. S., & Long, D. G. (2001). Image reconstruction and enhanced resolution imaging from irregular samples. *Ieee Transactions on Geoscience and Remote Sensing*, 39(2), 291-302. doi: 10.1109/36.905237

Fettweis, X. (2007), Reconstruction of the 1979-2006 Greenland ice sheet surface mass balance using the regional climate model MAR, *The Cryosphere, 1, 21-40*

Fettweis, X., Tedesco, M., van den Broeke, M., & Ettema, J. (2010). Melting trends over the Greenland ice sheet (1958–2009) from spaceborne microwave data and regional climate models. Cryosphere Discuss, 4, 2433-2473.

Fettweis, X., Tedesco, M., van den Broeke, M., & Ettema, J. (2011). Melting trends over the Greenland ice sheet (1958–2009) from spaceborne microwave data and regional climate models. The Cryosphere [= TC], 5.

Georgiu, S., A. Shepherd, M. McMillan and P. Nienow(2009) Seasonal evolution of supraglacial lake volume from ASTER imagery, *Annals of Glaciology,* 50(52), 95 – 100.

Grenfell, T. C., and D. K. Perovich (2004), Seasonal and spatial evolution of albedo in a snow-ice-land-ocean environment, *J. Geophys. Res.*, *109*, C01001, doi:10.1029/2003JC001866.

Hanna, E., Huybrechts, P., Janssens, I., Cappelen, J., Steffen, K., & Stephens, A. (2005). Runoff and mass balance of the Greenland ice sheet: 1958-2003. Journal of Geophysical Research, 110, D13108.

Hansen, J., Ruedy, R., Sato, M., & Lo, K. (2010a). GLOBAL SURFACE TEMPERATURE CHANGE. [Review]. Reviews of Geophysics, 48, 29. doi: Rg4004 10.1029/2010rg000345

Hansen, J., Ruedy, R., Sato, M., & Lo, K. (2010b). GLOBAL SURFACE TEMPERATURE CHANGE. Reviews of Geophysics, 48. doi: Rg4004 10.1029/2010rg000345

Herrmann, F. J. (2001). Singularity characterization by monoscale analysis: Application to seismic imaging. Applied and Computational Harmonic Analysis, 11(1), 64-88.

Hughes, T. J. (1981). THE WEAK UNDERBELLY OF THE WEST ANTARCTIC ICE-SHEET. Journal of Glaciology, 27(97), 518-525.

Jevrejeva, S., Moore, J. C., & Grinsted, A. (2010). How will sea level respond to changes in natural and anthropogenic forcings by 2100? Geophysical Research Letters, 37. doi: L07703 10.1029/2010gl042947

Joshi, M., Merry, C. J., Jezek, K. C., & Bolzan, J. F. (2001). An edge detection technique to estimate melt duration, season and melt extent on the Greenland ice sheet using passive microwave data. Geophysical Research Letters, 28(18), 3497-3500.

Joughin, I., & Alley, R. B. (2011). Stability of the West Antarctic ice sheet in a warming world. *Nature Geoscience*, 4(8), 506-513. doi: 10.1038/ngeo1194

Joughin, I., Das, S. B., King, M. A., Smith, B. E., Howat, I. M., & Moon, T. (2008). Seasonal speedup along the western flank of the Greenland Ice Sheet. *Science*, 320(5877), 781-783. doi: 10.1126/science.1153288

Joughin, I., S. Tulaczyk, M. Fahnestock and R. Kwok (1996), A mini-surge on the Ryder Glacier, Greenland, observed by satellite radar interferometry, *Science*, 274, 228–230

Kaufmann, Y. J., A. E. Wald, L. A. Remer, B.-C. Gao, R.-R. Li, and L. Flynn (1997), The MODIS 2.1-mm Channel-Correlation with Visible Reflectance for Use in Remote Sensing of Aerosol. *IEEE Transactions on Geoscience and Remote Sensing*. Vol. 35, pp. 1286-1298.

Kunz, L. B., D. G. Long (2006), Melt detection in Antarctic ice shelves using scatterometers and microwave radiometers, *Geoscience and Remote Sensing, IEEE Transactions on, 44*(9), 2461-2469.

Le Gonidec, Y., Conil, F., & Gibert, D. (2003). The wavelet response as a multiscale NDT method. *Ultrasonics*, 41(6), 487-497.

Lee, Z., et al. (1999), Hyperspectral remote sensing for shallow waters. 2. Deriving bottom depths and water properties by optimization, *Applied Optics*, *38*(18), 3831-3843.

Lemke, P., Ren, J., Alley, R. B., Allison, I., Carrasco, J., Flato, G., . . . Thomas, R. H. (2007). Observations: Changes in snow, ice and frozen ground. Titel: Climate change 2007: the physical science basis; summary for policymakers, technical summary and frequently asked questions. Part of the W*orking Group I contribution to the Fourth Assessment*

Report of the Intergovernmental Panel on Climate Change, 337-383.

Li, C., Zheng, C., & Tai, C. (1995). Detection of ECG characteristic points using wavelet transforms. *Biomedical Engineering, IEEE Transactions* on, 42(1), 21-28.

Liu, H., Wang, L., & Jezek, K. C. (2005). Wavelet-transform based edge detection approach to derivation of snowmelt onset, end and duration from satellite passive microwave measurements. *International Journal of Remote Sensing*, 26(21), 4639-4660.

Linden, P.F (2000), *Convection in the environment*. In Bachelor, G.K., H.K. Moffatt and M.G. Worster, eds. *Perspectives in fliud mechanics*, Cambridge, Cambridge University Press, 287–343

Long, D. G., & Hicks, B. R. (2000). Standard BYU QuikScat/SeaWinds land/ice image products. Brigham Young Univ., Provo, UT, *QuikScat Image Product documentation*

Lüthje, M., L.T. Pedersen, N. Reeh, and W. Greuell (2006), Modelling the evolution of supra-glacial lakes on the West Greenland ice-sheet margin, *Journal of Glaciology*, 52, 608-618.

Luthcke, S. B., Zwally, H., Abdalati, W., Rowlands, D., Ray, R., Nerem, R., . . . Chinn, D. (2006). Recent Greenland ice mass loss by drainage system from satellite gravity observations. *Science*, 314(5803), 1286.

MacAyeal, D. R., Scambos, T. A., Hulbe, C. L., & Fahnestock, M. A. (2003). Catastrophic ice-shelf break-up by an ice-shelf-fragment-capsize mechanism. *Journal of Glaciology*, 49(164), 22-36. doi: 10.3189/172756503781830863

Mallat, S., & Zhong, S. (1992). Characterization of signals from multiscale edges. IEEE *Transactions on pattern analysis and machine intelligence*, 14(7), 710-732.

Mallat, S. G. (1999). *A Wavelet Tour of Signal Processing:* Academic Press

Maritorena, S., A. Morel, and B. Gentili (1994), Diffuse reflectance of oceanic shallow waters:,\ Influence of water depth and bottom albedo, *Limnol. Oceanogr*., 39(7), 1689– 1703

Marshall, G. J. (2003). Trends in the Southern Annular Mode from observations and reanalyses. *Journal of climate*, 16(24), 4134-4143.

Marshall, G. J., Di Battista, S., Naik, S. S., & Thamban, M. (2011). Analysis of a regional change in the sign of the SAM–temperature relationship in Antarctica. *Climate Dynamics*, 36(1), 277-287.

McMillan, M., P. Nienow, A. Shepherd, T. Benham, and A. Sole (2007), Seasonal evolution of supra-glacial lakes on the Greenland ice sheet. *Earth and Planetary Science Letters*, 262, 484-492.

Meehl, G. A., Covey, C., Delworth, T., Latif, M., McAvaney, B., Mitchell, J. F. B., . . . Taylor, K. E. (2007). The WCRP CMIP3 multimodel dataset. *Bull. Am. Meteorol. Soc*, 88, 1383-1394.

Meier, M. F., Dyurgerov, M. B., Rick, U. K., O'Neel, S., Pfeffer, W. T., Anderson, R. S., . . . Glazovsky, A. F. (2007). Glaciers dominate Eustatic sea-level rise in the 21st century. *Science*, 317(5841), 1064-1067. doi: 10.1126/science.1143906

Mernild, S. H., Mote, T. L., & Liston, G. E. (2011). Greenland ice sheet surface melt extent and trends: 1960-2010. *Journal of Glaciology*, 57(204), 621-628.

Mobley, C.D. (1997), Estimation of the remote-sensing reflectance from above-surface measurements, *Appl. Optics,* 38(36), 7442-7455.

Mote, T. L., Anderson, M. R., Kuivinen, K. C., & Rowe, C. M. (1993). Passive microwave-derived spatial and temporal variations of summer melt on the Greenland ice sheet. *Annals of Glaciology*, 17, 233-233.

Mueller, J. (2003), In-Water Radiometric Profile Measurements and Data Analysis Protocols, *NASA/TM-2003-21621/Rev-Vol III, 7*.

Mueller, J., G. McClain, R. Bidigare, C. Trees, W. Balch, J. Dore, D. Drapeau, D. Karl, and L. Van (2003), Ocean optics protocols for satellite ocean color sensor validation, revision 5, volume V: Biogeochemical and bio-optical measurements and data analysis protocols, *NASA Tech. Memo*. 2003-211621, Rev, 5.

Munneke, P. K., Picard, G., van den Broeke, M. R., Lenaerts, J. T. M., & van Meijgaard, E. (2012). Insignificant change in Antarctic snowmelt volume since 1979. *Geophysical Research Letters*, 39. doi: L01501 10.1029/2011gl050207

Nghiem, S., Steffen, K., Neumann, G., & Huff, R. (2007). Snow accumulation and snowmelt monitoring in Greenland and Antarctica. *Dynamic Planet*, Springer, pages 31-38.

Nghiem, S. V., Steffen, K., Kwok, R., & Tsai, W. (2001). Detection of snowmelt regions on the Greenland ice sheet using diurnal backscatter change. *Journal of Glaciology*, 47(159), 539-547.

Nicholls, R. J. (2004). Coastal flooding and wetland loss in the 21st century: changes under the SRES climate and socio-economic scenarios. *Global Environmental Change-Human and Policy Dimensions*, 14(1), 69-86. doi: 10.1016/j.gloenvcha.2003.10.007

Nicholls, R. J., & Cazenave, A. (2010). Sea-level rise and its impact on coastal zones. *Science*, 329(5992), 628-628.

Ohmura, A. (2001). Physical basis for the temperature-based melt-index method. *Journal of Applied Meteorology*, 40(4), 753-761.

Overpeck, J. T., Otto-Bliesner, B. L., Miller, G. H., Muhs, D. R., Alley, R. B., & Kiehl, J. T. (2006). Paleoclimatic evidence for future ice-sheet instability and rapid sea-level rise. *Science*, 311(5768), 1747-1750. doi: 10.1126/science.1115159

Philpot, W. D. (1989), Bathymetric mapping with passive multispectral imagery, *Appl. Optics*, 28(8), 1569– 1578.

Picard, G., Fily, M., & Gallee, H. (2007). Surface melting derived from microwave radiometers: a climatic indicator in Antarctica. *Annals of Glaciology*, 46(1), 29-34.

Pimentel, S. and G. E. Flowers (2010), A numerical study of hydrologically driven glacier dynamics and subglacial flooding, *Proc. R. Soc. A* doi: 10.1098/rspa.2010.0211.

Pimentel, S., G.E. Flowers, and C.G. Schoof (2010), A hydrologically coupled higher-order flow-band model of ice dynamics with a Coulomb friction sliding law, *J. Geophys. Res.* 115, F04023, doi:10.1029/2009JF001621

Pope, R.M.and E. S. Fry (1997), Absorption spectrum (380–700 nm) of pure water. II. Integrating cavity measurements, *Appl. Opt.*, 36, 8710-8723.

Rahmstorf, S. (2007). A semi-empirical approach to projecting future sea-level rise. *Science*, 315(5810), 368-370. doi: 10.1126/science.1135456

Rahmstorf, S. (2010). A new view on sea level rise. *Nature Reports Climate Change*, 44-45.

Rignot, E., Casassa, G., Gogineni, P., Krabill, W., Rivera, A., & Thomas, R. (2004). Accelerated ice discharge from the Antarctic Peninsula following the collapse of Larsen B ice shelf. *Geophysical Research Letters*, 31(18). doi: L1840110.1029/2004gl020697

Rignot, E., & Thomas, R. H. (2002). Mass balance of polar ice sheets. *Science*, 297(5586), 1502.

Rignot, E., Velicogna, I., van den Broeke, M. R., Monaghan, A., & Lenaerts, J. (2011). Acceleration of the contribution of the Greenland and Antarctic ice sheets to sea level rise. *Geophysical Research Letters*, 38. doi: L05503 10.1029/2011gl046583

Rohling, E. J., Grant, K., Bolshaw, M., Roberts, A. P., Siddall, M., Hemleben, C., & Kucera, M. (2009). Antarctic temperature and global sea level closely coupled over the past five glacial cycles. *Nature Geoscience*, 2(7), 500-504. doi: 10.1038/ngeo557

Scambos, T., Hulbe, C., & Fahnestock, M. (2003). Climate-induced ice shelf disintegration in the Antarctic Peninsula. *Antarctic Research Series*, 79, 79-92.

Schoof, C. (2010). Ice-sheet acceleration driven by melt supply variability. *Nature*, 468(7325), 803-806. doi: 10.1038/nature09618

Selmes, N., T. Murray, and T. D. James (2011), Fast draining lakes on the Greenland Ice Sheet, *Geophysical Research Letters.*, *38*, L15501, doi:10.1029/2011GL047872.

Shepherd, A., & Wingham, D. (2007). Recent sea-level contributions of the Antarctic and Greenland ice sheets. *Science*, 315(5818), 1529.

Smith, R. C. and K. S. Baker (1981), Optical properties of the clearest natural waters (200-800 nm), *Appl. Optics*, Vol. 20, No. 2.

Sneed, W. A., and G. S. Hamilton (2007), Evolution of melt pond volume on the surface of the Greenland Ice Sheet, *Geophys. Res. Lett.*, *34*, L03501, doi:10.1029/2006GL028697.

Sneed, W. A., and G. S. Hamilton (2011), Validation of a method for determining the depth of glacial melt ponds using satellite imagery, *Annals of Glaciology 52(59)*, 15 – 22

Solomon, S., D., Qin, M., Manning, Z., Chen, M., Marquis, K. B., Averyt, M., & Miller, H. L. (2007). *Contribution of Working Group I to the Fourth Assessment Report of the Intergovernmental Panel on Climate Change*. Cambridge, United Kingdom and New York, NY, USA: Cambridge University Press.

Spencer, M. W., Tsai, W. Y., & Long, D. G. (2003). High-resolution measurements with a spaceborne pencil-beam scatterometer using combined range/doppler discrimination techniques. *Ieee Transactions on Geoscience and Remote Sensing*, 41(3), 567-581. doi: 10.1109/tgrs.2003.809938

Steffen, K., J. E. Box, and W. Abdalati (1996), Greenland Climate Network: GC-Net, in Colbeck, S. C. Ed. CRREL 96-27 *Special Report on Glaciers, Ice Sheets and Volcanoes, tribute to M. Meier*, 98-10

Steffen, K., Nghiem, S., Huff, R., & Neumann, G. (2004). The melt anomaly of 2002 on the Greenland Ice Sheet from active and passive microwave satellite observations. *Geophysical Research Letters*, 31(20), L20402.

Steig, E. J., Schneider, D. P., Rutherford, S. D., Mann, M. E., Comiso, J. C., & Shindell, D. T. (2009). Warming of the Antarctic ice-sheet surface since the 1957 International Geophysical Year. *Nature*, 457(7228), 459-462.

Stiles, W. H., & Ulaby, F. T. (1980). The active and passive microwave response to snow parameters 1. Wetness. *Journal of Geophysical Research*, 85(C2), 1037-1044.

Sundal, A.V., A. Shepherd , P. Nienow , E. Hanna, S. Palmer , P. Huybrechts (2009), Evolution of supra-glacial lakes across the Greenland Ice Sheet, *Remote Sensing of Environment* 113, 2164–2171.

Sundal, A. V., Shepherd, A., Nienow, P., Hanna, E., Palmer, S., & Huybrechts, P. (2011). Melt-induced speed-up of Greenland ice sheet offset by efficient subglacial drainage. *Nature*, 469(7331), 521-524.

Taubman, D. S., Marcellin, M. W., & Rabbani, M. (2002). JPEG2000: Image compression fundamentals, standards and practice. Journal of Electronic Imaging, 11, 286.

Tedesco, M. (2007). Snowmelt detection over the Greenland ice sheet from SSM/I brightness temperature daily variations. *Geophysical Research Letters*, 34(2). doi: L02504 10.1029/2006gl028466

Tedesco, M. (2009). Assessment and development of snowmelt retrieval algorithms over Antarctica from K-band spaceborne brightness temperature (1979-2008). *Remote Sensing of Environment*, 113(5), 979-997.

Tedesco, M., Abdalati, W., & Zwally, H. J. (2007). Persistent surface snowmelt over Antarctica (1987-2006) from 19.35 GHz brightness temperatures. *Geophysical Research Letters*, 34(18). doi: L1850410.1029/2007gl031199

Tedesco, M., Fettweis, X., Van den Broeke, M., Van de Wal, R., Smeets, C., van de Berg, W. J., . . . Box, J. (2011). The role of albedo and accumulation in the 2010 melting record in

Greenland. *Environmental Research Letters*, 6, 014005.

Tedesco, M., Kim, E. J., England, A. W., De Roo, R. D., & Hardy, J. P. (2006). Brightness temperatures of snow melting/refreezing cycles: Observations and modeling using a multilayer dense medium theory-based model. *Geoscience and Remote Sensing, IEEE Transactions* on, 44(12), 3563-3573.

Tedesco, M., Luthje, M., Steffen, K., Steiner, N., Fettweis, X., Willis, I., Banwell, A. (2012). Measurement and modeling of ablation of the bottom of supraglacial lakes in western Greenland. *Geophysical Research Letters,* 39. doi: L02502 10.1029/2011gl049882

Tedesco, M., & Monaghan, A. J. (2009). An updated Antarctic melt record through 2009 and its linkages to high-latitude and tropical climate variability. *Geophysical Research Letters*, 36, L18502.10.1029/2009gl039186

Tedesco M., and N. Steiner (2011), In-situ multispectral and bathymetric measurements over a supraglacial lake in western Greenland using a remotely controlled watercraft *The Cryosphere*, 5, 445-452

Thompson, D. W. J., & Wallace, J. M. (2000). Annular Modes in the Extratropical Circulation. Part I: Month-to-Month Variability*. *Journal of climate*, 13(5), 1000-1016.

Torinesi, O., Fily, M., & Genthon, C. (2003). Variability and trends of the summer melt period of Antarctic ice margins since 1980 from microwave sensors. *Journal of climate*, 16(7), 1047-1060.

Tsang, L., Kong, J. A., & Shin, R. T. (1985). *Theory of microwave remote sensing*. Wiley Interscience, 214-235.

Turner, J., Colwell, S. R., Marshall, G. J., Lachlan-Cope, T. A., Carleton, A. M., Jones, P. D., . . . Iagovkina, S. (2005). Antarctic climate change during the last 50 years. *International Journal of Climatology*, 25(3), 279-294.

Ulaby, F. T., R. K. Moore, and A. K. Fung (1981), *Microwave remote sensing: Active and passive. Volume 1-Microwave remote sensing fundamentals and radiometry*, Addison-Wesley,

Ulaby, F. T., & Stiles, W. H. (1980). The Active and Passive Microwave Response to Snow Parameters .2. Water Equivalent of Dry Snow. *Journal of Geophysical Research-Oceans and Atmospheres*, 85(NC2), 1045-1049. doi: 10.1029/JC085iC02p01045

van den Broeke, M. (2005). Strong surface melting preceded collapse of Antarctic Peninsula ice shelf. *Geophysical Research Letters*, 32(12). doi: L12815 10.1029/2005gl023247

van den Broeke, M., Bamber, J., Ettema, J., Rignot, E., Schrama, E., Van de Berg, W. J., . . . Wouters, B. (2009). Partitioning recent Greenland mass loss. *Science*, 326(5955), 984-986.

van den Broeke, M., Bus, C., Ettema, J., & Smeets, C. (2010). Temperature thresholds for degree-day modelling of Greenland ice sheet melt rates. *Geophysical Research Letters*,

37(18), L18501/18501-L18501/18505.

van den Broeke, M. R., Smeets, C. J. P. P., & van de Wal, R. S. W. (2011). The seasonal cycle and interannual variability of surface energy balance and melt in the ablation zone of the west Greenland ice sheet. *Cryosphere*, 5(2), 377-390. doi: 10.5194/tc-5-377-2011

van der Veen, C., Plummer, J., & Stearns, L. (2011). Controls on the recent speed-up of Jakobshavn Isbrae, West Greenland. *Journal of Glaciology*, 57(204), 770-782.

van Lipzig, N. P. M., Marshall, G. J., Orr, A., & King, J. C. (2008). The relationship between the Southern Hemisphere Annular Mode and Antarctic Peninsula summer temperatures: Analysis of a high-resolution model climatology. *Journal of Climate*, 21(8), 1649-1668.

Vaughan, D. G. (2006). Recent trends in melting conditions on the Antarctic Peninsula and their implications for ice-sheet mass balance and sea level. *Arctic Antarctic and Alpine Research*, 38(1), 147-152. doi: 10.1657/1523-0430(2006)038[0147:rtimco]2.0.co;2

Wang, L., & Yu, J. (2011). Spatiotemporal Segmentation of Spaceborne Passive Microwave Data for Change Detection. *Geoscience and Remote Sensing Letters*, IEEE(99), 909-913.

Wang, L. B., Derksen, C., & Brown, R. (2008). Detection of pan-Arctic terrestrial snowmelt from QuikSCAT, 2000-2005. *Remote Sensing of Environment*, 112(10), 3794-3805. doi: 10.1016/j.rse.2008.05.017

Zwally, H. J., Abdalati, W., Herring, T., Larson, K., Saba, J., & Steffen, K. (2002). Surface melt-induced acceleration of Greenland ice-sheet flow. *Science*, 297(5579), 218-222. doi: 10.1126/science.1072708

Zwally, H. J., & Fiegles, S. (1994). Extent and Duration of Antarctic Surface Melting. *Journal of Glaciology*, 40(136), 463-476.